

QUANTIFYING THE EVOLUTION OF CRYSTAL  
STRESSES DURING MONOTONIC AND CYCLIC  
LOADING USING FINITE ELEMENT  
SIMULATIONS

A Dissertation

Presented to the Faculty of the Graduate School  
of Cornell University

in Partial Fulfillment of the Requirements for the Degree of  
Doctor of Philosophy

by

Su Leen Wong

May 2011

© 2011 Su Leen Wong  
ALL RIGHTS RESERVED

QUANTIFYING THE EVOLUTION OF CRYSTAL STRESSES DURING  
MONOTONIC AND CYCLIC LOADING USING FINITE ELEMENT  
SIMULATIONS

Su Leen Wong, Ph.D.

Cornell University 2011

The focus of the current work is on investigating the orientation dependent micromechanical response of face-centered cubic (fcc) polycrystals using crystal-based elastoplastic finite element simulations. This dissertation contains three related studies examining the evolution of the lattice strains and the crystal stresses in fcc polycrystalline aggregates subjected to monotonic and cyclic loading. These three studies, which can be read independently, are presented in Chapters 1, 2 and 3.

Chapter 1 contains an investigation into the evolution of the orientation dependent lattice strain response in fcc polycrystals under monotonic tensile loading, particularly in the elastic-plastic transition regime leading up to fully-developed plasticity. The lattice strains, when plotted as a function of the macroscopic stress, begin to deviate from linear behavior in the elastic-plastic transition regime when certain sets of crystals begin yielding before others. It is demonstrated that the progression of yielding in different sets of crystals is influenced by a combination of the single crystal elastic and plastic anisotropies, which can be quantified by the directional strength-to-stiffness ratio [1].

Chapter 2 examines the evolution of the lattice strains and the crystal scale stress distributions in fcc polycrystals under fully-reversed, strain-controlled cyclic loading with respect to the concepts of the directional strength-to-stiffness

ratio [1] and the vertices of the single crystal yield surface [2], which have previously only been applied to monotonic tensile loading. These two concepts are derived from the single crystal elastic and plastic anisotropic properties and are used to explain observed behaviors in the lattice strain response such as the size and shape of the lattice strain hysteresis loops.

Chapter 3 presents a coordinated approach to quantifying the evolution of lattice strains in an AA7075-T6 aluminum alloy under *in situ* zero-tension cyclic loading using high-energy synchrotron x-ray diffraction experiments and crystal-based finite element simulations. This dissertation involves only the computational aspect of this coordinated approach. Lattice Strain Pole Figures (SPFs) are constructed from both measured and computed lattice strains and comparisons are made at the same macroscopic stress on several cycles in the loading history. Trends in the evolution of crystal quantities such as the crystal stresses, slip system activity and the slip system strengths, which are available from the simulation data, are examined and explained in a consistent manner with respect to the single crystal yield surface topology.

The final chapter, Chapter 4, is a brief summary of the preceding chapters highlighting the main contributions of this dissertation.

## **BIOGRAPHICAL SKETCH**

Su Leen Wong was born in 1984 in Kuala Lumpur, Malaysia. She came to Ithaca, New York in August 2003 to major in Mechanical Engineering at Cornell University and graduated with a Bachelor of Science degree in January 2006. Not long after graduating, she began her pursuit of a Ph.D. under the guidance of Professor Paul Dawson.

*Dedicated to my parents.*

## ACKNOWLEDGEMENTS

First and foremost, I would like to thank my special committee chairman, Professor Paul Dawson for his unending support, guidance and patience over the past five years.

Thank you to Professor Matthew Miller for being like a second advisor to me and for all his comments on the papers I wrote, they were greatly appreciated. Thank you to Professor Alan Zehnder for serving on my special committee.

I would like to thank my colleague and collaborator, Jay Schuren, who has been through this with me from the beginning. Thank you to Donald Boyce for all his help over the years and his infinite patience with all my questions. Thank you to all past and present DPLab colleagues, in particular Tito Marin, Hadas Ritz and Jun-Sang Park, for sharing their wealth of knowledge and experience when I first arrived at DPLab.

I am extremely grateful for the love and support from friends and family, near and far, over the years. I would not be where I am today without them.

Support for this work has been provided by the Air Force Office of Scientific Research (AFOSR) under grant number FA9550-06-1-0168.

## TABLE OF CONTENTS

Biographical Sketch . . . . .	iii
Dedication . . . . .	iv
Acknowledgements . . . . .	v
Table of Contents . . . . .	vi
List of Tables . . . . .	viii
List of Figures . . . . .	ix
<b>1 Influence of directional strength-to-stiffness on the elastic-plastic transition of fcc polycrystals under uniaxial tensile loading</b>	<b>1</b>
1.1 Abstract . . . . .	1
1.2 Introduction . . . . .	1
1.3 Background . . . . .	4
1.4 Methodology . . . . .	8
1.4.1 Crystal orientations . . . . .	9
1.4.2 Crystallographic fibers . . . . .	10
1.4.3 Single crystal elastic anisotropy . . . . .	11
1.4.4 Elastic and plastic behavior of crystals . . . . .	14
1.4.5 Virtual polycrystals and simulation of uniaxial tensile tests	17
1.5 Results . . . . .	20
1.5.1 Macroscopic stress-strain curve . . . . .	20
1.5.2 Evolution of the lattice strains . . . . .	21
1.5.3 Evolution of the stress distribution . . . . .	28
1.6 Role of strength-to-stiffness . . . . .	31
1.6.1 Structural analog . . . . .	32
1.6.2 Directional strength-to-stiffness ratio for a single crystal .	35
1.6.3 Directional strength-to-stiffness ratio for a crystallographic fiber of the polycrystal . . . . .	41
1.6.4 Average stress of a crystallographic fiber . . . . .	46
1.7 Conclusion . . . . .	49
<b>2 Evolution of the crystal stress distributions in face-centered cubic polycrystals subjected to cyclic loading</b>	<b>50</b>
2.1 Abstract . . . . .	50
2.2 Introduction . . . . .	51
2.3 Experimental observations . . . . .	54
2.4 Methodology . . . . .	57
2.5 Simulation results . . . . .	61
2.5.1 Macroscopic stress-strain response . . . . .	63
2.5.2 Lattice strain response . . . . .	64
2.5.3 Slip system activity . . . . .	68
2.6 Influences of directional strength-to-stiffness and SCYS topology on the cyclic response . . . . .	72

2.6.1	Directional strength-to-stiffness . . . . .	72
2.6.2	Vertices of the single crystal yield surface . . . . .	75
2.7	Conclusions . . . . .	84
<b>3</b>	<b>Quantifying the evolution of crystal stresses during cyclic loading using finite element simulations and high-energy x-ray diffraction</b>	<b>87</b>
3.1	Abstract . . . . .	87
3.2	Introduction . . . . .	88
3.3	Background . . . . .	90
3.3.1	Crystal orientations and crystallographic fibers . . . . .	92
3.4	Experiments . . . . .	93
3.4.1	Diffraction and lattice strains . . . . .	93
3.4.2	Material and mechanical testing method . . . . .	95
3.4.3	Lattice Strain Pole Figures (SPFs) . . . . .	97
3.4.4	Determination of lattice strain uncertainty . . . . .	98
3.5	Simulations . . . . .	99
3.5.1	Numerical formulation . . . . .	99
3.5.2	Virtual specimen and simulation of cyclic loading tests . . . . .	102
3.5.3	Determination of model constants . . . . .	103
3.5.4	Generation of SPFs from simulated data . . . . .	107
3.6	Results . . . . .	108
3.6.1	Residual lattice strain distribution . . . . .	108
3.6.2	Comparison between measured and simulated SPFs . . . . .	109
3.6.3	Evolution of SPFs with cycles . . . . .	112
3.6.4	Evolution of the computed crystal stresses with cycles . . . . .	115
3.7	Discussion . . . . .	125
3.8	Conclusions . . . . .	127
<b>4</b>	<b>Summary and findings</b>	<b>130</b>
<b>A</b>	<b>Approach for varying single crystal elastic moduli</b>	<b>132</b>
<b>B</b>	<b>Derivation of single crystal directional stiffness</b>	<b>135</b>

## LIST OF TABLES

1.1	Single crystal elastic moduli corresponding to different levels of single crystal elastic anisotropy, $r_E$ , for constant $E_{avg}$ and $\nu_{avg}$ . . .	14
1.2	Slip system hardening model parameters used in all the simulations. . . . .	18
2.1	Slip system and cyclic hardening model parameters for SS304L stainless steel [52]. . . . .	60
2.2	The different combinations of hardening and initial ODF for each set of simulations . . . . .	62
2.3	Single crystal elastic moduli corresponding to $r_E = 1.0$ and $r_E = 3.2$ . Representative values of the single crystal elastic moduli for stainless steel ( $r_E = 3.2$ ) were obtained from Ref. [55]. . . . .	63
2.4	Directional strength-to-stiffness values for selected single crystal directions and averages over crystallographic fibers. . . . .	74
2.5	Relative magnitude of the deviatoric vertex stress, $\sigma'_{v,i}$ , for the five vertex families associated with the fcc SCYS [2]. . . . .	76
3.1	Slip system and hardening model parameters determined for AA7075-T6 in the first suite of simulations. . . . .	104
3.2	Single crystal elastic moduli corresponding to $r_E = 1.3$ determined for AA7075-T6. . . . .	106
3.3	Magnitude of the deviatoric form of the vertex stress, $\sigma'_{v,i}$ , for each vertex stress family [2]. . . . .	119

## LIST OF FIGURES

1.1	Applied stress versus elastic lattice strains for crystals with $\{hkl\}$ plane normals parallel to the tensile axis from Clausen et. al. [14]. Symbols are measured lattice strains and lines are computed lattice strains. . . . .	7
1.2	Computed lattice strains for crystals with $\{hkl\}$ plane normals parallel to the tensile axis from Clausen, Lorentzen and Leffers [29]. . . . .	8
1.3	Several prominent crystallographic fibers in the cubic fundamental region of Rodrigues space. The [001] direction is the specimen loading direction. . . . .	12
1.4	Interior of the virtual polycrystal showing the complete rhombic dodecahedra crystals. The XYZ coordinate system is the specimen coordinate system. . . . .	18
1.5	Nominal and true macroscopic stress-strain curves for $r_E = 1.0$ and $r_E = 3.0$ . . . . .	21
1.6	Lattice strain, $\varepsilon_{\{hkl\}}$ , and plastic deformation rate magnitude, $D_{\{hkl\}}^p$ as a function of the macroscopic true stress for $r_E = 1.0$ . LD is the loading direction which is also the [001] specimen direction. . . . .	23
1.7	Lattice strain, $\varepsilon_{\{hkl\}}$ , and plastic deformation rate magnitude, $D_{\{hkl\}}^p$ as a function of the macroscopic true stress for $r_E = 1.4$ . LD is the loading direction which is also the [001] specimen direction. . . . .	24
1.8	Lattice strain, $\varepsilon_{\{hkl\}}$ , and plastic deformation rate magnitude, $D_{\{hkl\}}^p$ as a function of the macroscopic true stress for $r_E = 2.0$ . LD is the loading direction which is also the [001] specimen direction. . . . .	24
1.9	Lattice strain, $\varepsilon_{\{hkl\}}$ , and plastic deformation rate magnitude, $D_{\{hkl\}}^p$ as a function of the macroscopic true stress for $r_E = 3.0$ . LD is the loading direction which is also the [001] specimen direction. . . . .	25
1.10	Macroscopic true stress-strain curves for $r_E = 1.0$ and $r_E = 3.0$ . The points on the curve are at 300 MPa, 500 MPa and 640 MPa which correspond to the linear elastic regime, the elastic-plastic transition regime and the fully-developed plasticity regime respectively. . . . .	29
1.11	Axial stress distribution, $\sigma_{zz}$ , over the fundamental region. The stress distributions correspond to the macroscopic axial stress levels shown in Figure 1.10. . . . .	31

1.12	(a) Two blocks of identical dimensions but of different materials are loaded in compression between rigid plates which result in an isostrain condition for the two materials; (b) Individual stress-strain response of each material. Material 2 achieves its yield strength before Material 1 under the same strain even though Material 2 has the higher yield strength; (c) Combined load-displacement response of the whole system; (d) Elastic strain for each material as a function of the total stress of the whole system. Initially before either material yields, they both have the same elastic strain. . . . .	33
1.13	Cubic crystal lattice with the uniaxial stress component in the $\mathbf{d}$ direction, $\tau_d$ . The 123 coordinate system is aligned with the edges of the crystal lattice, while the stress tensor with the uniaxial stress component in the $\mathbf{d}$ direction is defined in the $\mathbf{d}\hat{2}\hat{3}$ coordinate system. . . . .	36
1.14	(a) Schmid factor, $m_d$ , for fcc crystals plotted on the fundamental orientation triangle. (b) Directional elastic stiffness, $E_d^{\text{crys}}$ , for pure aluminum ( $r_E = 1.2$ ) plotted on the fundamental orientation triangle. (c) Directional strength-to-stiffness ratio, $r_{s,d}^{\text{crys}}$ , for $r_E = 1.0$ . (d) Directional strength-to-stiffness ratio, $r_{s,d}^{\text{crys}}$ , for $r_E = 3.0$ .	38
1.15	Directional strength-to-stiffness ratio, $r_{S,\{hkl\}}^{\text{crys}}$ , computed for a single crystal under uniaxial tension. . . . .	39
1.16	The Taylor factor, $M_{\{hkl\}}^{\text{fiber}}$ , for different crystallographic fibers at two levels of the single crystal elastic anisotropy, $r_E$ . The abscissa corresponds to the macroscopic true strain. In fully-developed plasticity, the Taylor factors approach a steady-state value and are independent of the single crystal elastic anisotropy. . . . .	43
1.17	$(\tau_{zz}/\epsilon_{zz})_{\{hkl\}}$ for different crystallographic fibers at two levels of the single crystal elastic anisotropy, $r_E$ . The abscissa corresponds to the macroscopic true stress. . . . .	44
1.18	Directional strength-to-stiffness ratio, $r_{S,\{hkl\}}^{\text{fiber}}$ , computed for several crystallographic fibers. . . . .	45
1.19	Non-axial components of the average Kirchhoff stress tensor for a crystallographic fiber, normalized by the axial stress component, $\tau_{zz}^{\text{fiber}}$ , in the elastic regime. . . . .	47
1.20	Non-axial components of the average Kirchhoff stress tensor for a crystallographic fiber, normalized by the axial stress component, $\tau_{zz}^{\text{fiber}}$ , in the fully-developed plasticity regime. . . . .	48
2.1	Lattice strains of crystals with the $\{111\}$ and $\{200\}$ lattice plane normals aligned with the axial loading direction for stainless steel specimens under fully reversed cyclic loading between fixed strain limits. . . . .	56

2.2	Macroscopic true stress-strain curves for 20 complete cycles for simulation Sets 1 and 3. . . . .	65
2.3	Lattice strain, $\varepsilon_{\{hkl\}}$ , versus macroscopic true stress for the simulations of Set 1. The lattice strains are averaged among crystals belonging to the $\{100\} \parallel \text{LD}$ and $\{111\} \parallel \text{LD}$ crystallographic fibers, where LD corresponds to the $[001]$ specimen loading direction. . . . .	66
2.4	Lattice strain, $\varepsilon_{\{hkl\}}$ , versus macroscopic true stress for the simulations of Set 3. The lattice strains are averaged among crystals belonging to the $\{100\} \parallel \text{LD}$ and $\{111\} \parallel \text{LD}$ crystallographic fibers, where LD corresponds to the $[001]$ specimen loading direction. . . . .	67
2.5	The solid black lines on the stress-strain curve correspond to the portions of the stress-strain curve where $D_{\{hkl\}}^p$ is plotted on Cycles 0, 1 and 20 for Set 1. . . . .	69
2.6	Plastic deformation rate magnitude, $D_{\{hkl\}}^p$ , versus macroscopic true stress for crystals belonging to the $\{100\} \parallel \text{LD}$ and $\{111\} \parallel \text{LD}$ crystallographic fibers for the simulations of Set 1. The LD direction corresponds to the $[001]$ specimen loading direction. The plastic deformation rate magnitude, $D_{\{hkl\}}^p$ , is plotted starting at a macroscopic stress of -100 MPa until a macroscopic strain of 1% is achieved, which is shown for Cycles 0, 1 and 20 in Figure 2.5. . . . .	70
2.7	Plastic deformation rate magnitude, $D_{\{hkl\}}^p$ , versus macroscopic true stress for crystals belonging to the $\{100\} \parallel \text{LD}$ and $\{111\} \parallel \text{LD}$ crystallographic fibers for the simulations of Set 3. The LD direction corresponds to the $[001]$ specimen loading direction. . . . .	70
2.8	Single crystal directional strength-to-stiffness ratio shown within the basic orientation triangle for $r_E = 1.0$ and $r_E = 3.2$ . The figures have the same grayscale bar for comparison purposes. . . . .	73
2.9	Lattice strain, $\varepsilon_{\{hkl\}}$ , versus macroscopic true strain associated with the the $\{100\} \parallel \text{LD}$ and $\{111\} \parallel \text{LD}$ fibers for the simulations of Set 1, where LD is the specimen loading direction. . . . .	77
2.10	Coaxiality angle, $\phi_c^v$ , between the crystal stress and the nearest vertex stress for several crystallographic fibers at 1% macroscopic strain on Cycle 1. V1-V5 correspond to the five unique vertex families. . . . .	78
2.11	Points along the macroscopic stress-strain curve on Cycles 0, 1 and 20 for which the distributions of the normalized deviatoric stress magnitudes are plotted in Figures 2.12–2.14. . . . .	80
2.12	Normalized deviatoric stress magnitudes for $r_E = 1.0$ and $r_E = 3.2$ on Cycle 0 at 0.065%, 0.4% and 1% macroscopic strain. . . . .	81
2.13	Normalized deviatoric stress magnitudes for $r_E = 1.0$ and $r_E = 3.2$ on Cycle 1 at -0.8%, -0.3% and 1% macroscopic strain. . . . .	82
2.14	Normalized deviatoric stress magnitudes for $r_E = 1.0$ and $r_E = 3.2$ on Cycle 20 at -0.8%, -0.3% and 1% macroscopic strain. . . . .	83

2.15	Slip system strength distribution by crystallographic fiber at 1% macroscopic strain for $r_E = 1.0$ and $r_E = 3.2$ . . . . .	84
3.1	Schematic of a lattice Strain Pole Figure (SPF) experiment conducted in transmission. Here $D$ and $\rho$ are the sample to detector distance and the radial distance on the detector, respectively. . .	94
3.2	EBSD maps for the rolling and transverse planes of the AA7075-T6 aluminum alloy sheet. . . . .	95
3.3	The ODF determined from the experiments, plotted over the cubic fundamental region of Rodrigues orientation space. The ODF is represented in terms of Multiples of Uniform Distribution (MUD). . . . .	96
3.4	Relationship between a point on a pole figure and a crystallographic fiber in Rodrigues space . . . . .	98
3.5	Macroscopic stress-strain curves from the experiments and simulations on Cycle 0. Points are indicated on the macroscopic stress-strain curve where diffraction measurements were conducted. Strain Pole Figure (SPF) comparisons were made between the experiments and simulations at the macroscopic stress levels corresponding to these points. . . . .	104
3.6	Macroscopic stress-strain curves from the experiments and simulations for cyclic loading. . . . .	107
3.7	Measured residual SPFs at a macroscopic stress of 0 MPa, prior to loading. Note that the colorbar scale is not symmetric. . . . .	109
3.8	Experiment, simulation and difference SPFs for three different $\{hkl\}$ s at 515 MPa on Cycle 0. Note that the colorbar scale for Figure 3.8(c) is different. . . . .	110
3.9	Experiment, simulation and difference SPFs for three different $\{hkl\}$ s at 515 MPa on Cycle 100. Note that the colorbar scale for Figure 3.9(c) is different. . . . .	111
3.10	Difference SPFs between Cycle 1 and Cycle 0 at 515 MPa for the experiments and simulations, where the Cycle 0 SPF is subtracted from the Cycle 1 SPF. Note that the colorbar scales for the two figures are different. . . . .	113
3.11	Difference SPFs between Cycle 10 and Cycle 0 at 515 MPa for the experiments and simulations, where the Cycle 0 SPF is subtracted from the Cycle 10 SPF. . . . .	114
3.12	Difference SPFs between Cycle 100 and Cycle 0 at 515 MPa for the experiments and simulations, where the Cycle 0 SPF is subtracted from the Cycle 100 SPF. . . . .	115
3.13	Magnitudes of the crystals stress vectors computed from the simulations and plotted on pole figures. Note that the colorbar scale for Figure 3.13(c) is different. . . . .	117

3.14	Net slip system shearing rate, $\dot{\gamma}$ , plotted over a pole figure for Cycles 0 and 100. Note that the colorbar scales are different. . . .	121
3.15	Slip system strength computed from the simulations. Note that the scale for Figure 3.15(c) is different. . . . .	122
3.16	Angle between macroscopic stress and crystal stress computed from the simulations. Note that the scale for Figure 3.16(c) is different. . . . .	124

## CHAPTER 1

# INFLUENCE OF DIRECTIONAL STRENGTH-TO-STIFFNESS ON THE ELASTIC-PLASTIC TRANSITION OF FCC POLYCRYSTALS UNDER UNIAXIAL TENSILE LOADING

### 1.1 Abstract

Crystal-based finite element simulations have been conducted on virtual face-centered cubic (fcc) polycrystals under uniaxial tensile loading to study the influence of single crystal elastic anisotropy on the elastic-plastic transition behavior exhibited by the lattice strains. The lattice strain response is examined for different sets of crystals corresponding to different crystallographic fibers. The lattice strain response observed in the elastic-plastic transition is related to crystals associated with different crystallographic fibers yielding on average at different levels of the macroscopic stress. The lattice strain behavior is determined by a combination of the elastic and plastic anisotropies of the single crystals, which is quantified using the directional strength-to-stiffness ratio. The directional strength-to-stiffness ratio for a single crystal and a crystallographic fiber are introduced and they are used to explain the deviation of the lattice strains from linear behavior in the elastic-plastic transition leading up to fully-developed plasticity.

### 1.2 Introduction

Most engineering alloys are polycrystalline, composed of large numbers of individual crystals with different lattice orientations with respect to some reference coordinate frame. Single crystals exhibit anisotropy due to the orientation

dependence of the elastic stiffness and plastic strength of these crystals. The elastic stiffness depends on the single crystal elastic anisotropy while the plastic strength depends on the slip system geometry of the crystal structure. The orientation of a crystal with respect to the macroscopic loading causes some crystals to appear stiffer than others and some crystals to be more favorably oriented to yield than others. This leads to variations in the stress distribution at the crystal level, even for a simple macroscopic loading condition such as uniaxial tension. Such variations are important, as the more highly stressed crystals within a polycrystal can serve, for example, as initiation sites for performance-limiting defects.

The mechanical response of a crystal within a polycrystalline aggregate is dependent on its single crystal properties, its lattice orientation, and the orientations of neighboring crystals. The influence of elastic anisotropy on the response of individual crystals within a polycrystal, however, is masked by the interactions of large numbers of randomly oriented crystals. A polycrystal may exhibit a nearly isotropic elastic response on the macroscopic scale regardless of the level of the single crystal elastic anisotropy if the crystals have uniformly distributed lattice orientations. Although the macroscopic elastic responses of polycrystals with uniformly distributed lattice orientations are the same with high or low single crystal elastic anisotropy, the micromechanical responses are quite different. It is important to note that the degree of single crystal elastic anisotropy can vary within a single alloy system, such as with the addition of increasing amounts of an alloying element (aluminum with high percentage of magnesium vs. pure aluminum), and not just between completely different materials (copper vs. aluminum). Accurate determination of single crystal properties is important in developing a quantitative understanding of the mi-

mechanical behavior of polycrystalline aggregates.

In the current work, the effect of varying the single crystal elastic anisotropy is examined for face-centered cubic (fcc) polycrystals under uniaxial tensile loading through the elastic-plastic transition into fully-developed plasticity. The level of single crystal elastic anisotropy is varied while holding the macroscopic elastic response (average Young's modulus and Poisson's ratio) and the plasticity parameters constant. The responses to varying the single crystal elastic anisotropy are determined using crystal-based finite element simulations of virtual fcc polycrystals where individual crystals within the polycrystal consist of multiple finite elements. The method of varying the single crystal elastic moduli in the current work is similar to the approach used in Ref. [3], where the single crystal elastic moduli of an AA-5182 aluminum alloy were varied systematically to improve the match between the computed lattice strains and the lattice strains measured using neutron diffraction. For a polycrystal under uniaxial tensile loading, we demonstrate that the level of single crystal elastic anisotropy influences the evolution of the orientation dependent lattice strains, beginning with the elastic-plastic transition and proceeding until fully-developed plasticity is achieved. We examine lattice strains in sets of crystals that share a common orientation of designated crystallographic planes (indicated by their Miller indices,  $\{hkl\}$ ), similar to measurements made in neutron diffraction experiments. Further, from the simulation results, we also show that different sets of crystals corresponding to different  $\{hkl\}$  lattice planes begin yielding, on average, at different levels of the macroscopic stress. We demonstrate that the yielding behavior of crystals corresponding to different  $\{hkl\}$ s is influenced by the combined elastic and plastic anisotropies of the crystals, which is quantified using the directional strength-to-stiffness ratio.

This chapter is organized as follows. In Section 1.3, we review previous experimental and computational efforts to quantify the evolution of the lattice strains through the elastic-plastic transition. Section 1.4 describes the analytical tools required to conduct the single crystal elastic parametric study, the methodology for constructing virtual polycrystals, and the methodology for conducting numerical simulations on the virtual polycrystals. Section 1.5 shows the results of the single crystal elastic anisotropy parametric study. In Section 1.6 the definition of the directional strength-to-stiffness ratio is introduced and its role in determining the evolution of the lattice strains is examined.

### 1.3 Background

Diffraction methods enable the interrogation of subsets of crystals within a polycrystal and lead to the ability to quantify stresses at the crystal level. X-ray and neutron diffraction have been used to measure residual stresses in polycrystalline metals [4, 5]. Diffraction techniques have also been used to measure lattice strains in specimens under *in situ* loading [6–8]. In a diffraction experiment, a shift in a diffraction peak under load corresponds to a lattice strain measurement of a subset of crystals within the polycrystal with a particular  $\{hkl\}$  crystallographic plane normal aligned with a particular specimen direction. Combining the lattice strain data from a broad suite of  $\{hkl\}$  reflections gives sufficient information to determine the lattice strain tensor as a function of lattice orientation [9, 10]. Often only a few  $\{hkl\}$  reflections are examined, and while these are insufficient to reconstruct the full, orientation dependent strain tensor, the data nevertheless are useful in understanding the behaviors at the crystal scale.

To motivate the numerical study presented in the current work, we focus on

studies that report diffraction measurements of the evolution of lattice strains under *in situ* loading, particularly through the elastic-plastic transition regime. Numerous researchers have measured lattice strains under *in situ* loading using neutron diffraction for fcc [11–18], bcc [19–22] and hcp [23–28] polycrystalline metals. These neutron diffraction measurements have typically been limited to a few  $\{hkl\}$  lattice planes parallel and perpendicular to the specimen loading direction. The neutron diffraction measurements were used to validate various polycrystal deformation models such as the Taylor [11–13], self-consistent [14–21, 23–29] and finite element models [21, 22].

The polycrystalline metals tested in the studies referenced above have consistently shown that the lattice strains deviate from linear behavior in the elastic-plastic transition through fully-developed plasticity. The deviations of the lattice strains from linear behavior arise due to load redistribution between different crystals of different orientations when some crystals begin to yield. Even under a macroscopic uniaxial stress state, different crystal  $\{hkl\}$  families yield at different levels of the macroscopic stress and the crystals which continue to deform elastically carry an increased proportion of the applied load. The lattice strains that arise due to incompatibilities in deformation between crystals in the elastic-plastic transition are typically referred to as intergranular strains.

The polycrystalline fcc metals previously studied [11–18] span a wide range in the single crystal elastic anisotropy as well as exhibit different lattice strain responses in the elastic-plastic transition. The suite of simulations conducted by Clausen, Lorentzen and Leffers [29] showed that aluminum, copper and stainless steel exhibited different lattice strain responses for different  $\{hkl\}$ s under uniaxial tensile loading. The load redistribution between the crystals in the elastic-plastic transition was attributed generally to a combination of the elas-

tic and plastic behavior of the material. Oliver, Daymond and Withers [21] have also compared the residual elastic strains of low carbon (LC) steel with the residual strains of a bcc polycrystal with the same plastic properties as the LC steel but with isotropic elastic properties. They found that in the absence of elastic anisotropy, the lattice strains exhibit different behaviors once yielding begins which led them to conclude that both the elastic and plastic properties influence the development of intergranular strains in a polycrystal. Although the materials previously studied have different levels of single crystal elastic anisotropy, a systematic study has not been conducted to quantify the effect of the combination of elastic and plastic properties on the orientation dependent lattice strains in the elastic-plastic transition regime.

Our current work is discussed, in particular, in the context of two publications by Clausen and various collaborators [14, 29]. Clausen et. al. [14] have measured and simulated the evolution of the lattice strains during uniaxial tensile loading of stainless steel and the relevant results are shown in Figure 1.1. The single crystal elastic moduli of stainless steel result in a relatively high single crystal elastic anisotropy value of  $r_E = 3.20$ , where  $r_E$  is the ratio of the elastic stiffness in the  $\langle 111 \rangle$  crystal direction to the elastic stiffness in the  $\langle 100 \rangle$  crystal direction. Figure 1.1 shows that the  $\{200\}$  crystals deviate significantly from linear behavior in the elastic-plastic transition and exhibit larger elastic strains relative to the crystals associated with other  $\{hkl\}$ s.

Clausen et al. [29] conducted a suite of simulations to model the lattice strains of aluminum, copper and austenitic stainless steel under uniaxial tensile loading using an elastic-plastic self-consistent model. The single crystal elastic anisotropy for aluminum, copper and stainless steel are  $r_E = 1.18$ ,  $r_E = 2.87$  and  $r_E = 3.20$  respectively. Aluminum has low single crystal elastic anisotropy while

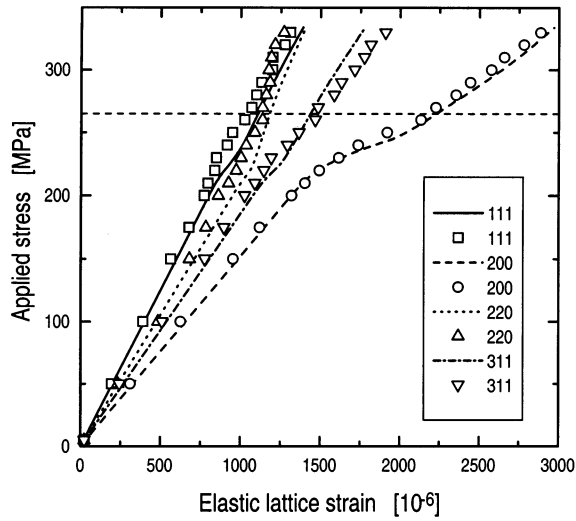


Figure 1.1: Applied stress versus elastic lattice strains for crystals with  $\{hkl\}$  plane normals parallel to the tensile axis from Clausen et al. [14]. Symbols are measured lattice strains and lines are computed lattice strains.

copper and stainless steel have relatively high single crystal elastic anisotropy. The lattice strains as a function of the applied stress for the three materials are shown in Figure 1.2. It is observed that for aluminum, which has much lower elastic anisotropy than either copper or stainless steel, the lattice strains in the elastic-plastic transition show different relative behaviors in comparison to the lattice strains in copper and stainless steel. Specifically, the  $\{111\}$  crystals in aluminum exhibit larger lattice strains in the elastic-plastic transition through fully-developed plasticity in comparison to the lattice strains associated with other  $\{hkl\}$ s. In contrast, for copper and stainless steel, the  $\{200\}$  crystals exhibit larger lattice strains relative to the other  $\{hkl\}$ s. The copper and stainless steel lattice strains in the elastic-plastic transition behave similarly, with the  $\{200\}$  crystals exhibiting the greatest elastic strains. The  $\{311\}$  crystals in copper and stainless steel maintain a response that is close to linear while the other  $\{hkl\}$ s (except the  $\{200\}$  crystals) exhibit a compressive shift relative to their linear elastic response.

These results indicate that the single crystal elastic anisotropy has a strong effect on the evolution of the lattice strains through the elastic-plastic transition.

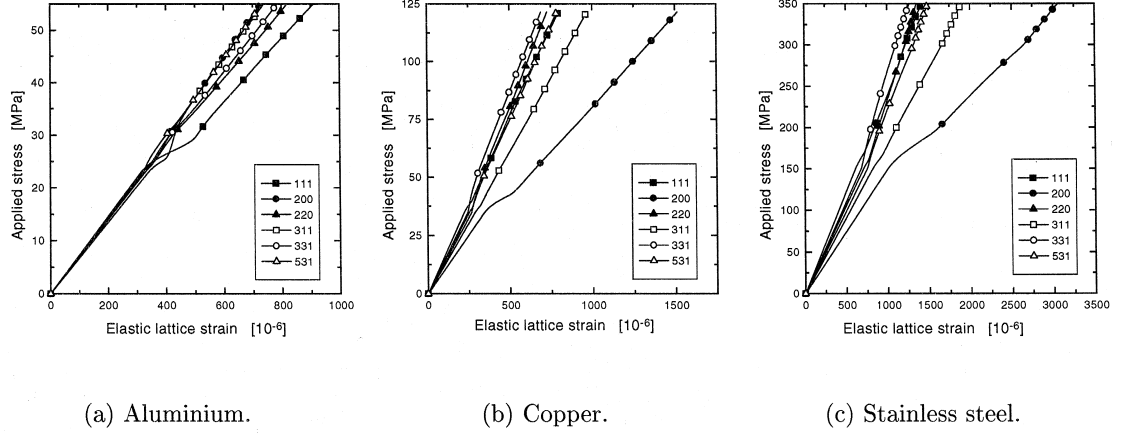


Figure 1.2: Computed lattice strains for crystals with  $\{hkl\}$  plane normals parallel to the tensile axis from Clausen, Lorentzen and Leffers [29].

Based on the results shown in Figures 1.1 and 1.2, the contribution of this paper is to quantify the combined role of the single crystal elastic anisotropy and plastic anisotropy, using the directional strength-to-stiffness ratio. We demonstrate that the directional strength-to-stiffness ratio of the crystals can be used to explain the behavior of the orientation dependent lattice strains in the elastic-plastic transition.

## 1.4 Methodology

In this section we describe the methodology used to numerically simulate the response of a polycrystal to obtain lattice strain data similar to measured lattice strain data from diffraction experiments. Section 1.4.1 describes the metric that is used to specify the crystal orientations within a polycrystalline aggregate. To

compare our simulation results to published results, we need to determine the subsets of crystals within the virtual polycrystal that satisfy a particular diffraction condition. Section 1.4.2 describes the relation used to identify particular subsets of crystals of the virtual polycrystal. Section 1.4.3 describes the method of varying the level of single crystal elastic anisotropy while keeping the average macroscopic elastic response constant. A brief outline of the elastic and plastic constitutive relations of single crystals is presented in Section 1.4.4. The description of the construction of the virtual polycrystal, the boundary conditions, and the method of post-processing the simulation data are presented in Section 1.4.5.

### 1.4.1 Crystal orientations

The description of a crystal orientation within a polycrystalline aggregate is important because of the orientation dependence of the elastic and plastic response of a single crystal. Two Cartesian coordinate systems are used to specify the orientation of a crystal: the crystal coordinate system defined by the orthonormal basis vectors,  $\mathbf{e}_i^c$ , and the specimen coordinate system defined by the orthonormal basis vectors,  $\mathbf{e}_i^s$ . For a crystal structure with orthogonal symmetry, the crystal basis vectors,  $\mathbf{e}_i^c$ , are typically aligned with the three orthogonal directions of the crystal unit cell. The specimen basis vectors,  $\mathbf{e}_i^s$ , are typically aligned with the normals of three perpendicular surfaces of the polycrystalline specimen. The orientation of a crystal within an aggregate is defined as the rotation needed to align the crystal coordinate frame with the reference or specimen coordinate frame.

Specifically, a rotation or orientation matrix,  $\mathbf{R}$ , transforms a vector in the

crystal coordinate system,  $\mathbf{v}^c$ , to a vector in the sample coordinate system,  $\mathbf{v}^s$ :

$$\mathbf{R}\mathbf{v}^c = \mathbf{v}^s \quad (1.1)$$

The rotation matrix can also be described in terms of a rotation axis,  $\mathbf{n}$ , and the angle of rotation,  $\phi$ , about the axis using Rodrigues parameterization of orientations [30]:

$$\mathbf{r} = \mathbf{n} \tan \frac{\phi}{2} \quad (1.2)$$

The Rodrigues vector,  $\mathbf{r}$ , is related to the rotation matrix through [31, 32]:

$$\mathbf{R} = \frac{1}{1 + \mathbf{r} \cdot \mathbf{r}} ((1 - \mathbf{r} \cdot \mathbf{r})\mathbf{I} + 2(\mathbf{r} \otimes \mathbf{r} + \mathbf{I} \times \mathbf{r})) \quad (1.3)$$

A point in Rodrigues space corresponds to the angle-axis combination that describes the orientation of the crystal with respect to the specimen coordinate system. The Rodrigues parameterization of orientations is advantageous because the Rodrigues parameter space can be reduced using crystal symmetries to a fundamental region bounded by planes. The fundamental region for crystals which possess cubic symmetry has the shape of a truncated cube as shown in Figure 1.3. In this chapter, quantities that depend on orientation will be plotted over the fundamental region.

## 1.4.2 Crystallographic fibers

A crystallographic fiber, represented as  $\mathbf{c} \parallel \mathbf{s}$ , connects all orientations that align a particular crystal axis,  $\mathbf{c}$ , with a particular specimen direction,  $\mathbf{s}$ :

$$\mathbf{R}\mathbf{c} = \pm \mathbf{s} \quad (1.4)$$

The equation for a crystallographic fiber in Rodrigues space for a fixed specimen frame is represented as [32]:

$$\tilde{\mathbf{r}} = \frac{1}{1 + \mathbf{c} \cdot \mathbf{s}} \left( \mathbf{c} \times \mathbf{s} + (\mathbf{c} + \mathbf{s}) \tan \frac{\phi_c}{2} \right) \quad (1.5)$$

where  $\phi_c$  is an arbitrary rotation about the crystal axis,  $c$ .

All orientations belonging to a crystallographic fiber differ only by a rotation about a common axis. The Rodrigues method of representing orientations is particularly attractive because crystallographic fibers appear as straight lines in Rodrigues space. Crystallographic fibers provide a basis for comparison between simulations and diffraction measurements on polycrystals because a particular crystallographic fiber associates directly with a particular Bragg diffraction condition. Diffraction experiments measure the normal component of the lattice strain of all crystals with the  $\{hkl\}$  plane normal aligned with a particular scattering vector (specimen direction). In the simulations, the normal component of the lattice strain is averaged among all crystals with their  $\{hkl\}$  plane normal, given by a crystal direction,  $c$ , aligned with a particular specimen direction,  $s$ .

Several prominent crystallographic fibers considered in the analysis are shown in Figure 1.3, with  $s = [001]$ . The specimen  $[001]$  direction is of particular interest because it is the loading direction in the simulations. Since only the specimen loading direction is considered in this analysis, the  $\{hkl\} \parallel [001]$  fiber will also be referred to as the  $\{hkl\}$  fiber. The  $\{hkl\}$  fiber is the collection of all crystals where the  $\{hkl\}$  plane normal of the crystal is aligned with the specimen  $[001]$  direction. The  $\{hkl\}$  plane normal is also denoted as the  $\langle hkl \rangle$  direction.

### 1.4.3 Single crystal elastic anisotropy

We are interested in the influence of the level of single crystal elastic anisotropy on the evolution of the lattice strains as the deformation proceeds under uniaxial tension. A definition for the single crystal elastic anisotropy and the method of systematically varying the single crystal elastic moduli are briefly described in

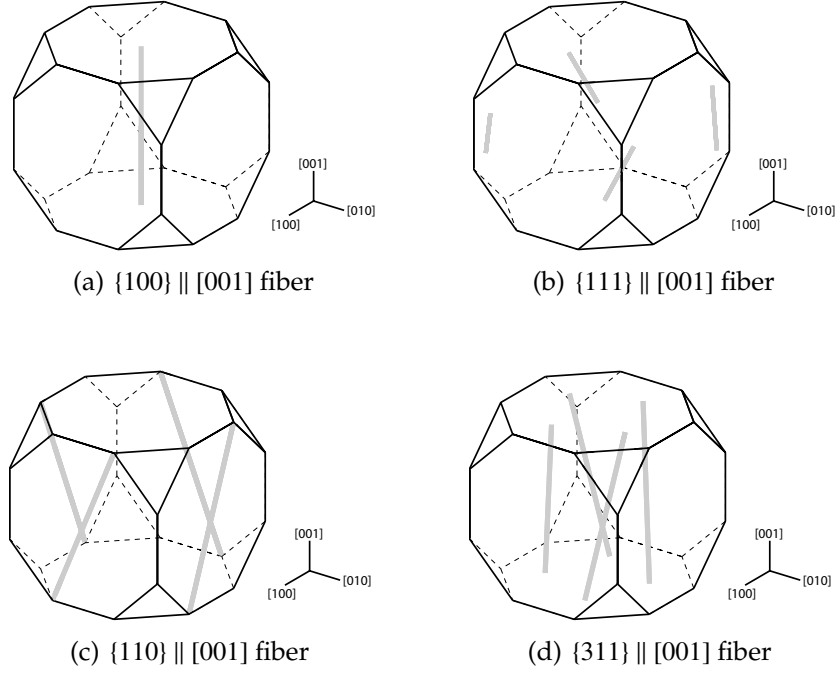


Figure 1.3: Several prominent crystallographic fibers in the cubic fundamental region of Rodrigues space. The [001] direction is the specimen loading direction.

this section.

The Kirchhoff stress tensor of a crystal,  $\tau$ , is related to the elastic strain tensor,  $\epsilon$ , by a fourth-order elastic stiffness tensor,  $\mathbb{C}$ , which is defined in the crystal coordinate system:

$$\tau = \mathbb{C} : \epsilon \quad (1.6)$$

The Kirchhoff stress,  $\tau$ , is related to the Cauchy stress,  $\sigma$ , by  $\tau = \det(\mathbf{I} + \epsilon)$ . Using the Voigt matrix notation, the Kirchhoff stress tensor,  $\tau$ , and the elastic strain tensor,  $\epsilon$ , in Equation (1.6) can be expressed as  $6 \times 1$  vectors as shown in Equation (1.7). The elastic stiffness tensor,  $\mathbb{C}$ , for cubic crystals can also be reduced to

a 6×6 matrix with three independent elastic constants,  $C_{11}$ ,  $C_{12}$  and  $C_{44}$  [33]:

$$\begin{pmatrix} \tau_{11} \\ \tau_{22} \\ \tau_{33} \\ \tau_{23} \\ \tau_{13} \\ \tau_{12} \end{pmatrix} = \begin{bmatrix} C_{11} & C_{12} & C_{12} & 0 & 0 & 0 \\ C_{12} & C_{11} & C_{12} & 0 & 0 & 0 \\ C_{12} & C_{12} & C_{11} & 0 & 0 & 0 \\ 0 & 0 & 0 & C_{44} & 0 & 0 \\ 0 & 0 & 0 & 0 & C_{44} & 0 \\ 0 & 0 & 0 & 0 & 0 & C_{44} \end{bmatrix} \begin{pmatrix} \epsilon_{11} \\ \epsilon_{22} \\ \epsilon_{33} \\ \epsilon_{23} \\ \epsilon_{13} \\ \epsilon_{12} \end{pmatrix} \quad (1.7)$$

Elastic anisotropy in a single crystal is the dependence of the elastic response on the orientation of the stress with respect to the crystallographic axes of the crystal lattice. The level of elastic anisotropy of a single crystal with cubic symmetry is quantified by the ratio of the Young's modulus in the  $\langle 111 \rangle$  direction to the Young's modulus in the  $\langle 100 \rangle$  direction, defined as the elastic anisotropy ratio,  $r_E$ :

$$r_E = \frac{E_{\langle 111 \rangle}}{E_{\langle 100 \rangle}} \quad (1.8)$$

In cubic crystals, the  $\langle 111 \rangle$  direction is typically the stiffest direction and the  $\langle 100 \rangle$  direction is the most compliant direction.

For cubic crystals, three independent elastic constants are required to determine the anisotropic single crystal elastic response. In this study, we are interested in the crystal level response when the elastic anisotropy ratio,  $r_E$ , is varied, while keeping the average macroscopic elastic response of the aggregate constant. We use the method of varying  $r_E$  described by Dawson et. al. [3] by constructing two average parameters, an average Young's modulus,  $E_{\text{avg}}$ , and an average Poisson's ratio,  $\nu_{\text{avg}}$ , for a polycrystalline aggregate with a uniform orientation distribution. Therefore in our approach to varying  $r_E$ , we chose the three independent parameters:  $r_E$ ,  $E_{\text{avg}}$  and  $\nu_{\text{avg}}$ . Using a simple relationship between the anisotropic single crystal moduli and the average properties, we vary

$r_E$	$C_{11}$ (GPa)	$C_{12}$ (GPa)	$C_{44}$ (GPa)
1.0	110.700	59.200	51.500
1.2	107.300	60.900	56.600
1.4	104.356	62.372	61.015
1.5	103.099	63.000	62.901
1.6	101.944	63.578	64.634
2.0	98.141	65.479	70.338
2.5	94.691	67.204	75.513
3.0	92.166	68.467	79.301

Table 1.1: Single crystal elastic moduli corresponding to different levels of single crystal elastic anisotropy,  $r_E$ , for constant  $E_{\text{avg}}$  and  $\nu_{\text{avg}}$ .

$r_E$  while keeping  $E_{\text{avg}}$  and  $\nu_{\text{avg}}$  constant. Additional details of the approach for varying the single crystal elastic moduli can also be found in appendix A.

Starting from the single crystal elastic moduli of pure aluminum reported by Hosford [34], where  $C_{11} = 107.3$  GPa,  $C_{12} = 60.9$  GPa and  $C_{44} = 56.6$  GPa, we compute  $r_E = 1.20$ ,  $E_{\text{avg}} = 69.45$  GPa and  $\nu_{\text{avg}} = 0.35$ . By keeping the values of  $E_{\text{avg}}$  and  $\nu_{\text{avg}}$  fixed and specifying a new value for  $r_E$ , we can solve the system of equations corresponding to Equations (A.6)–(A.8) in appendix A for the new values of  $C_{11}$ ,  $C_{12}$  and  $C_{44}$ .

A range of  $r_E$ s were chosen to represent single crystal elastic behavior ranging from isotropic ( $r_E = 1.0$ ) to highly anisotropic ( $r_E = 3.0$ ) behavior. Table 1.1 shows the single crystal elastic moduli generated from different values of  $r_E$  for constant  $E_{\text{avg}}$  and  $\nu_{\text{avg}}$ .

#### 1.4.4 Elastic and plastic behavior of crystals

The numerical formulation used in the simulations involves an elastoplastic constitutive model which determines the behavior of a single crystal, implemented within a finite element formulation which determines the behavior

of an aggregate of crystals. The single crystal constitutive model is based on anisotropic elasticity coupled with plastic deformation by crystallographic slip on a restricted number of slip systems. The equations of the single crystal constitutive model are then implemented within a finite element framework based on the weak form of the equilibrium equations. A complete description of the constitutive model and the finite element implementation can be found in Refs. [35–37].

We consider crystallographic slip through the crystal lattice to be the dominant mode of plastic deformation. The crystal lattice also undergoes rotations and elastic stretching. The crystal kinematics are represented by a multiplicative decomposition of the deformation gradient tensor,  $\mathbf{F}$  [35]:

$$\mathbf{F} = \mathbf{V}^* \mathbf{R}^* \mathbf{F}^P \quad (1.9)$$

where  $\mathbf{F}^P$  is the purely plastic part of  $\mathbf{F}$ ,  $\mathbf{R}^*$  is the lattice rotation and  $\mathbf{V}^*$  is the elastic stretch. Equation (1.9) defines a reference configuration,  $\mathcal{B}_0$ , and the current configuration,  $\mathcal{B}$ , as well as two intermediate configurations,  $\bar{\mathcal{B}}$  and  $\hat{\mathcal{B}}$ . A schematic illustrating these configurations can be found in Ref. [35].

In metals and metallic alloys, the elastic strains are typically many orders in magnitude smaller than the plastic strains in fully-developed plasticity (macroscopic strains exceeding 2%). By using the small strain assumption, the elastic stretch tensor,  $\mathbf{V}^*$ , is related to the infinitesimal strain tensor,  $\boldsymbol{\epsilon}$ :

$$\mathbf{V}^* = \mathbf{I} + \boldsymbol{\epsilon} \quad (1.10)$$

where  $\mathbf{I}$  is the identity tensor.

The crystal constitutive equations are expressed in the  $\hat{\mathcal{B}}$  configuration, defined by  $\hat{\mathbf{F}}^P = \mathbf{R}^* \mathbf{F}^P$ , which is achieved by elastically unloading without rotation from the current configuration,  $\mathcal{B}$ . The constitutive relations for the elastic and

plastic response of a crystal can be written separately. The elastic response is a linear relation between the the Kirchhoff stress,  $\boldsymbol{\tau}$ , and the elastic strain,  $\boldsymbol{\epsilon}$ , as shown in Equation (1.6).

The plastic velocity gradient,  $\hat{\mathbf{L}}^p$ , can be decomposed into its symmetric and skew-symmetric parts:

$$\hat{\mathbf{L}}^p = \dot{\hat{\mathbf{F}}}^p \hat{\mathbf{F}}^{p-1} = \hat{\mathbf{D}}^p + \hat{\mathbf{W}}^p \quad (1.11)$$

Plastic deformation occurs by crystallographic slip on a restricted number of slip systems. For each slip system  $\alpha$ , a slip direction,  $\hat{\mathbf{s}}^\alpha$ , and a slip plane normal,  $\hat{\mathbf{m}}^\alpha$ , are defined in the  $\hat{\mathcal{B}}$  configuration. Introducing the contributions of each  $\alpha$ -slip system in Equation (1.11), the viscoplastic flow rule for crystallographic slip is expressed as:

$$\hat{\mathbf{D}}^p = \sum_{\alpha} \dot{\gamma}^{\alpha} \hat{\mathbf{P}}^{\alpha} \quad \text{and} \quad \hat{\mathbf{W}}^p = \dot{\mathbf{R}}^* \mathbf{R}^{*T} + \sum_{\alpha} \dot{\gamma}^{\alpha} \hat{\mathbf{Q}}^{\alpha} \quad (1.12)$$

where  $\hat{\mathbf{P}}^{\alpha} = \text{sym}(\hat{\mathbf{s}}^{\alpha} \otimes \hat{\mathbf{m}}^{\alpha})$ ,  $\hat{\mathbf{Q}}^{\alpha} = \text{skw}(\hat{\mathbf{s}}^{\alpha} \otimes \hat{\mathbf{m}}^{\alpha})$  and  $\dot{\gamma}^{\alpha}$  is the plastic shearing rate of the  $\alpha$ -slip system. The plastic shearing rate on the  $\alpha$ -slip system,  $\dot{\gamma}^{\alpha}$ , is related to the crystal stress through a power law form:

$$\dot{\gamma}^{\alpha} = \dot{\gamma}_0^{\alpha} \left( \frac{|\tau^{\alpha}|}{g^{\alpha}} \right)^{\frac{1}{m}} \text{sgn}(\tau^{\alpha}) \quad (1.13)$$

where  $g^{\alpha}$  is the slip system strength,  $\dot{\gamma}_0^{\alpha}$  is a reference shear rate and  $m$  is the rate sensitivity of slip. The resolved shear stress,  $\tau^{\alpha}$ , is the projection of the deviatoric part of the Kirchhoff stress,  $\boldsymbol{\tau}'$ , on the  $\alpha$ -slip system:

$$\tau^{\alpha} = \boldsymbol{\tau}' : \hat{\mathbf{P}}^{\alpha} \quad (1.14)$$

## 1.4.5 Virtual polycrystals and simulation of uniaxial tensile tests

A virtual polycrystal in the shape of a cube is instantiated with 2916 rhombic dodecahedra crystals. The complete rhombic dodecahedra crystals in the interior of the virtual polycrystal are shown in Figure 1.4 but there are additional partial crystals that make up the surfaces of the cube which are not shown. The virtual polycrystal is made up of a total of 192000 finite elements. A rhombic dodecahedra crystal has 12 faces and consists of 48 10-node tetrahedra finite elements which are assigned the same initial lattice orientation. The initial orientations of all the crystals are randomly assigned from a uniform orientation distribution function (ODF). The orientations of the finite elements that constitute a crystal are allowed to evolve independently as the deformation proceeds. The crystals have the fcc crystal structure which deform by crystallographic slip on  $\{111\}$  slip planes in  $\langle 110 \rangle$  slip directions. This finite element mesh is used in all the simulations in this study. Uniaxial tension loading boundary conditions are applied to the finite element mesh. A constant axial velocity is applied on the top Z surface of the mesh, while the bottom Z surface is constrained in the Z-direction. The two positive X and Y surfaces of the mesh are traction-free, while the X=0 and Y=0 surfaces have a symmetry boundary condition imposed.

The suite of simulations conducted involves varying the single crystal elastic anisotropy,  $r_E$ , while keeping all other input parameters fixed. The initial slip system strength of all the crystals are assigned the same value, while the slip hardening parameters are kept constant and  $r_E$  is varied. The different levels of  $r_E$  examined in this suite of simulations are shown in Table 1.1 and the slip system hardening model parameters used are shown in Table 1.2. The vir-

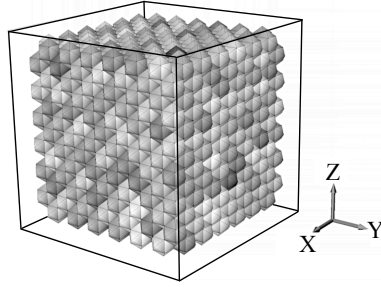


Figure 1.4: Interior of the virtual polycrystal showing the complete rhombic dodecahedra crystals. The XYZ coordinate system is the specimen coordinate system.

tual polycrystal is loaded monotonically until the macroscopic nominal stress reaches 580 MPa. The macroscopic nominal stress of 580 MPa corresponds to approximately a macroscopic true stress of 640 MPa.

$h_0$ (MPa)	$g_0$ (MPa)	$g_{s0}$ (MPa)	$m$	$m'$	$\dot{\gamma}_0$ ( $s^{-1}$ )	$\dot{\gamma}_{s0}$ ( $s^{-1}$ )
200	235	350	0.02	0.0	1.0	$5 \times 10^{10}$

Table 1.2: Slip system hardening model parameters used in all the simulations.

The parametric study has also been conducted on a smaller finite element mesh with 1098 complete dodecahedra crystals and 81000 finite elements. The results for the smaller virtual polycrystal mesh are consistent with the results corresponding to the larger mesh. This indicates that the number of crystals in both meshes are sufficient to obtain statistically relevant information. In addition, simulations were conducted without slip system strengthening and reorientation of the crystals. The simulation results without slip system strengthening and reorientation are consistent with the simulation results with slip system strengthening and reorientation up to the end of the elastic-plastic transition regime.

The first step in post-processing the simulation data is to determine the ele-

ments in the finite element mesh with orientations which correspond to one of the four crystallographic fibers shown in Figure 1.3. There are 24 symmetry operations for the cubic crystal type,  $\mathbf{R}_{\text{sym}}$ , and when applied to the crystal plane normal  $\{hkl\} = \mathbf{c}$ , result in crystal directions that are indistinguishable from the original crystal direction:

$$\mathbf{c}_{\text{sym}} = \mathbf{R}_{\text{sym}}\mathbf{c} \quad (1.15)$$

The angle between the crystal directions,  $\mathbf{c}_{\text{sym}}$ , and the specimen loading direction,  $\mathbf{s}$ , is computed as:

$$\theta = \cos^{-1}(\mathbf{c}_{\text{sym}} \cdot \mathbf{s}) \quad (1.16)$$

The minimum value of  $\theta$  for all  $\mathbf{c}_{\text{sym}}$ ,  $\theta_c$ , is taken to be the misorientation angle between the crystal  $\{hkl\}$  plane normal and the specimen direction  $\mathbf{s}$ . To determine whether a crystal belongs to a crystallographic fiber, the angle  $\theta_c$  associated with a crystal must be less than a critical angle,  $\theta_{\text{crit}}$ :

$$\theta_c < \theta_{\text{crit}} \quad (1.17)$$

The angle  $\theta_{\text{crit}}$  must be large enough to encompass a statistically significant number of crystals contributing to each crystallographic fiber, but small enough to exclude crystals that do not satisfy the diffraction condition. Values for  $\theta_{\text{crit}}$  of  $2^\circ$ ,  $3^\circ$  and  $5^\circ$  were used to determine whether a crystal belongs to a particular crystallographic fiber. The results presented in Section 1.5 correspond to  $\theta_{\text{crit}} = 3^\circ$  for the finite element mesh with 2916 crystals and 192000 elements.

The results corresponding to the three different values of  $\theta_{\text{crit}}$  show similar trends, although the results corresponding to  $\theta_{\text{crit}} = 2^\circ$  show some discontinuities in the evolution of certain crystal quantities which are averaged along a crystallographic fiber. The discontinuities indicate that there may be insuffi-

cient crystals contributing to a crystallographic fiber to provide statistically significant information comparable to diffraction measurements on polycrystals.

## 1.5 Results

Simulations have been conducted on the virtual polycrystal under uniaxial tensile loading for different levels of the single crystal elastic anisotropy,  $r_E$ , reported in Table 1.1. The initial slip system strengths and the slip hardening parameters have the same values across all simulations. The goal of this suite of simulations is not to attempt to compare the lattice strain simulation results with experimental measurements for different materials, but to use the suite of simulations to examine solely the influence of single crystal elastic anisotropy on the evolution of the lattice strains.

Section 1.5.1 shows the nominal and true macroscopic stress-strain curves for two values of  $r_E$ :  $r_E = 1.0$ , which corresponds to elastically isotropic single crystals, and  $r_E = 3.0$ , which corresponds to highly elastically anisotropic single crystals. The evolution of the lattice strains and the plastic deformation rate magnitudes for crystals belonging to different crystallographic fibers are presented in Section 1.5.2. The stress distributions of the polycrystal over Rodrigues space at various stages of the deformation are discussed in Section 1.5.3.

### 1.5.1 Macroscopic stress-strain curve

The nominal and true macroscopic stress-strain curves are shown in Figure 1.5 for two values of  $r_E$ :  $r_E = 1.0$  and  $r_E = 3.0$ . The single crystal elastic anisotropy,  $r_E$ , is varied such that the macroscopic Young's modulus (slope of the elas-

tic portion of the macroscopic stress-strain curve) is constant for all values of  $r_E$  under consideration. As seen in Figure 1.5,  $r_E$  influences the macroscopic stress-strain behavior, particularly in the elastic-plastic transition regime. In fully-developed plasticity (macroscopic strains exceeding 2%), the macroscopic strains are slightly larger for lower values of  $r_E$  at the same macroscopic stress.

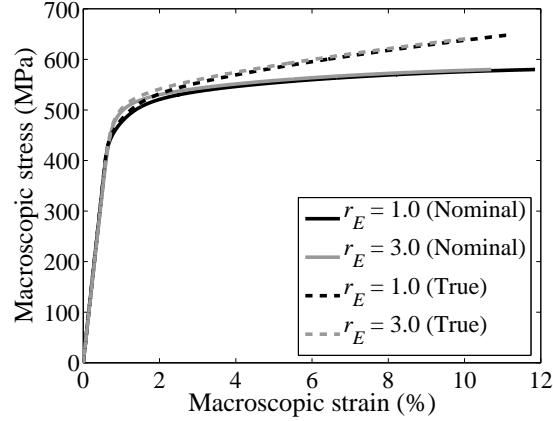


Figure 1.5: Nominal and true macroscopic stress-strain curves for  $r_E = 1.0$  and  $r_E = 3.0$ .

## 1.5.2 Evolution of the lattice strains

The lattice strain,  $\varepsilon_{\{hkl\}}$ , and the plastic deformation rate magnitude,  $D_{\{hkl\}}^P$ , are presented for the  $\{hkl\} \parallel [001]$  crystallographic fibers shown in Figure 1.3. The lattice strain,  $\varepsilon_{\{hkl\}}$ , is the normal component of the elastic strain tensor parallel to the specimen loading direction  $[001]$ . The subscript  $\{hkl\}$  denotes that the quantity is averaged among all crystals belonging to the  $\{hkl\} \parallel [001]$  crystallographic fiber. As the  $[001]$  specimen direction is the only specimen direction considered in the analysis, the notations  $\{hkl\} \parallel [001]$  and  $\{hkl\}$  are used interchangeably. The plastic deformation rate,  $\hat{\mathbf{D}}^P$ , is a second-order tensor which is computed using Equation (1.12). Since plastic flow in the material an isochoric process,  $\hat{\mathbf{D}}^P$  can

be expressed as a deviatoric 5-vector,  $\hat{\mathbf{D}}^P$ . For notational simplicity, the plastic deformation rate magnitude will be denoted as  $D^P = \|\hat{\mathbf{D}}^P\|$ .

The lattice strains,  $\varepsilon_{\{hkl\}}$ , and the plastic deformation rate magnitude,  $D_{\{hkl\}}^P$ , are plotted as a function of the macroscopic true stress for increasing levels of the single crystal elastic anisotropy,  $r_E$ , in Figures 1.6–1.9. A rapid increase in  $D_{\{hkl\}}^P$  indicates that on average, the crystals belonging to the  $\{hkl\} \parallel [001]$  crystallographic fiber have yielded and plastic flow has commenced among these crystals. Although simulations were conducted for all the different values of  $r_E$  specified in Table 1.1, only results for select cases of  $r_E$  are shown in this section.

The results presented here correspond to a value of  $\theta_{\text{crit}} = 3^\circ$ . The evolution of the plastic deformation rate magnitude exhibits some discontinuities when  $\theta_{\text{crit}} = 2^\circ$ , although the macroscopic stress at which crystals associated with a crystallographic fiber begin to yield on average is not affected within the range of  $\theta_{\text{crit}}$  values examined. The peak value of the plastic deformation rate magnitude is also influenced slightly by the value of  $\theta_{\text{crit}}$ , but the macroscopic stress at which a rapid increase in the plastic deformation rate magnitude occurs is not affected by the value of  $\theta_{\text{crit}}$  within the range of values examined.

### Elastic response

The lattice strains in the elastic regime are first considered for the results shown in Figures 1.6–1.9. The lattice strains for the case where the crystals are elastically isotropic ( $r_E = 1.0$ ) are shown in Figure 1.6(a). The lattice strains for all  $\{hkl\}$ s have the same magnitude in the elastic regime when  $r_E = 1.0$ , which is expected for an elastically isotropic material.

As the value of  $r_E$  is increased above  $r_E = 1.0$ , the spread increases between the lattice strains for different  $\{hkl\}$ s in the elastic regime, as evident in Fig-

ures 1.6(a), 1.7(a), 1.8(a) and 1.9(a). The relative magnitudes of the lattice strains in the elastic regime follow the same order as the relative magnitudes of the directional elastic stiffness of a single crystal. The computation of the directional elastic stiffness is described in more detail in Section 1.6.2. The  $\langle 111 \rangle$  crystal direction is the stiffest direction and the  $\langle 100 \rangle$  crystal direction is the most compliant direction, which is reflected in the relative magnitudes of the  $\{111\}$  and  $\{100\}$  lattice strains.

The plastic deformation rate magnitudes in the elastic regime are zero for all the  $\{hkl\}$ s because no plastic flow occurs in the elastic regime (by definition). However, a rapid increase in the plastic deformation rate magnitude occurs at different levels of the macroscopic stress for crystals belonging to different  $\{hkl\}$  fibers, which indicates that the crystals belonging to different  $\{hkl\}$  fibers yield on average at different levels of the macroscopic stress.

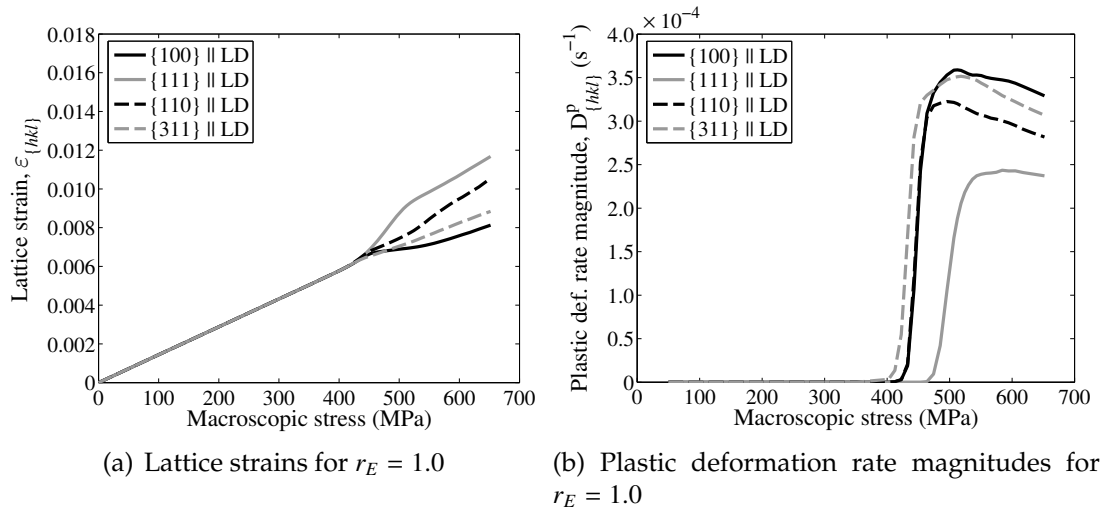


Figure 1.6: Lattice strain,  $\varepsilon_{\{hkl\}}$ , and plastic deformation rate magnitude,  $D_{\{hkl\}}^P$ , as a function of the macroscopic true stress for  $r_E = 1.0$ . LD is the loading direction which is also the  $[001]$  specimen direction.

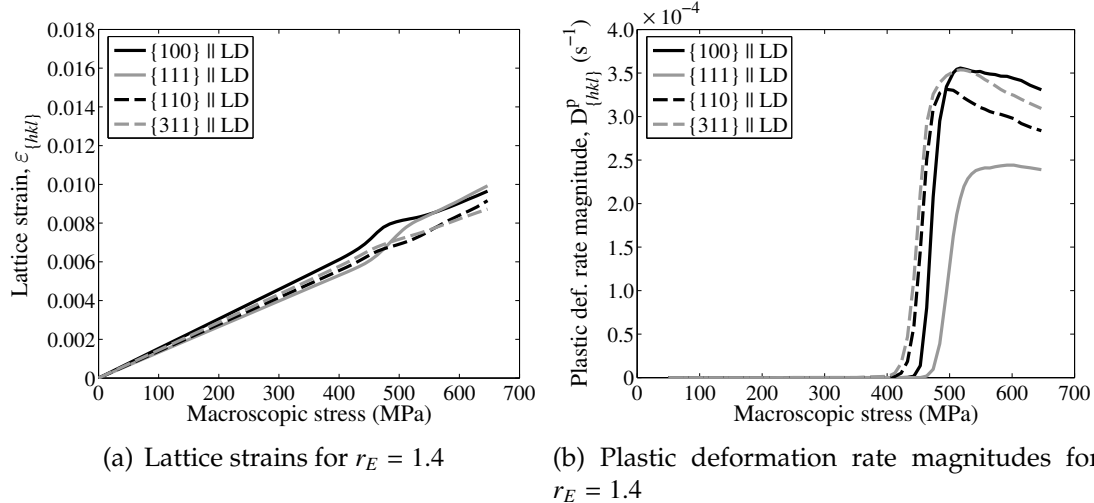


Figure 1.7: Lattice strain,  $\varepsilon_{\{hkl\}}$ , and plastic deformation rate magnitude,  $D_{\{hkl\}}^P$ , as a function of the macroscopic true stress for  $r_E = 1.4$ . LD is the loading direction which is also the [001] specimen direction.

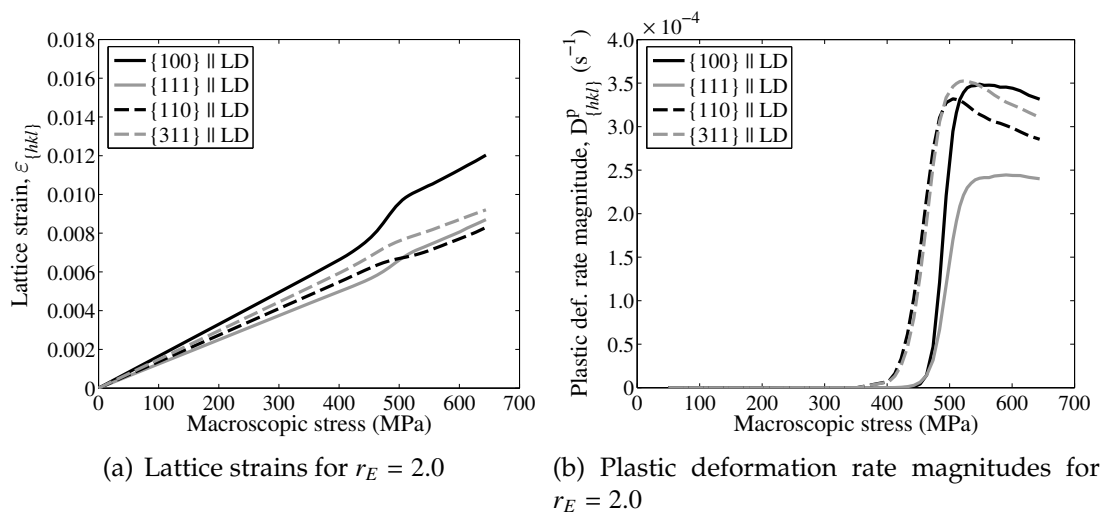


Figure 1.8: Lattice strain,  $\varepsilon_{\{hkl\}}$ , and plastic deformation rate magnitude,  $D_{\{hkl\}}^P$ , as a function of the macroscopic true stress for  $r_E = 2.0$ . LD is the loading direction which is also the [001] specimen direction.

### Elastic-plastic transition

For  $r_E = 1.0$ , the lattice strains for all  $\{hkl\}$ s have the same magnitude in the elastic regime but once yielding begins and plastic deformation occurs, the lattice

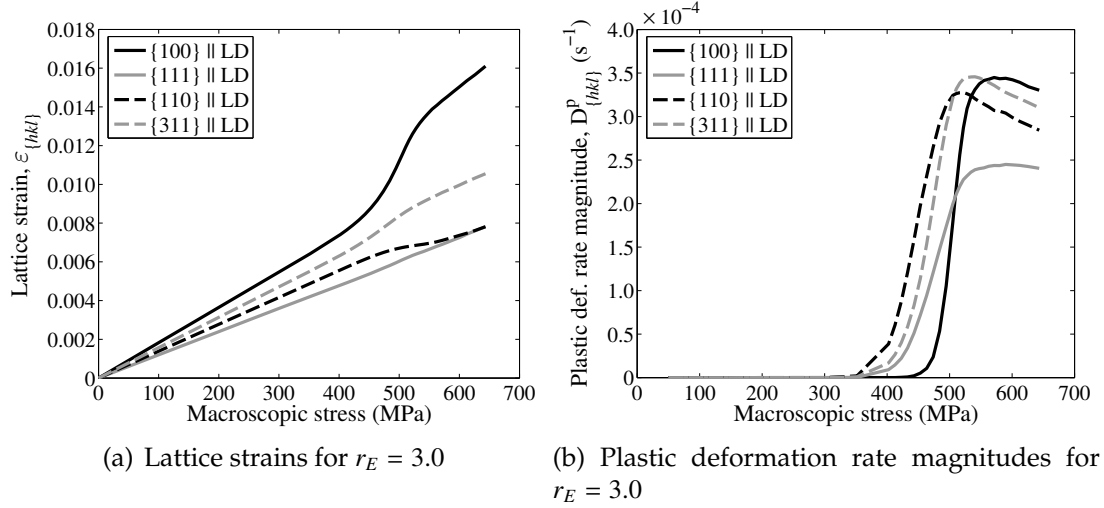


Figure 1.9: Lattice strain,  $\varepsilon_{\{hkl\}}$ , and plastic deformation rate magnitude,  $D_{\{hkl\}}^P$ , as a function of the macroscopic true stress for  $r_E = 3.0$ . LD is the loading direction which is also the [001] specimen direction.

strains for different  $\{hkl\}$ s begin diverging in the elastic-plastic transition regime (Figure 1.6(a)). The separation between lattice strains continues into the fully-developed plasticity regime. The fully-developed plastic regime is the stage of the deformation where the crystals have activated sufficient slip systems such that the plastic part of the deformation rate,  $\mathbf{D}^P$ , is equal to the total deformation rate,  $\mathbf{D}$ , ( $\mathbf{D}^P = \mathbf{D}$ ). Although the crystals are elastically isotropic for  $r_E = 1.0$ , Figure 1.6(b) demonstrates that there is also plastic or yield strength anisotropy because on average, crystals belonging to different crystallographic fibers yield at different levels of the macroscopic stress. The  $\{111\}$  lattice strains rise above the other  $\{hkl\}$  lattice strains in the plastic regime and this is accompanied by crystals belonging to the  $\{111\}$  fiber yielding on average at a relatively higher macroscopic stress compared to crystals belonging to other fibers (Figure 1.6(b)). The crystals belonging to other fibers yield at approximately the same macroscopic stress level and yielding is accompanied by a downward inflection of the lattice strains in the elastic-plastic transition regime, as apparent in Figure 1.6(a).

The lattice strains and plastic deformation rate magnitudes for  $r_E = 1.4, 2.0$  and  $3.0$  are shown in Figures 1.7–1.9. As the value of  $r_E$  is increased above  $r_E = 1.0$ , the lattice strains are influenced by a combination of the elastic and plastic anisotropies which results in different behaviors in the elastic-plastic transition regime. Examining first the lattice strains for  $r_E = 1.4$  (Figure 1.7(a)), the  $\{110\}$  and  $\{311\}$  lattice strains exhibit a downward inflection in the elastic-plastic transition regime which is accompanied by crystals belonging to the  $\{110\}$  and  $\{311\}$  fibers yielding on average at a lower macroscopic stress (Figure 1.7(b)). The crystals belonging to the  $\{100\}$  fiber yield on average at a higher macroscopic stress than the crystals belonging to either the  $\{110\}$  or  $\{311\}$  fibers. Initially the  $\{100\}$  lattice strains exhibit an upward inflection in the elastic-plastic transition when the  $\{110\}$  and  $\{311\}$  lattice strains exhibit a downward inflection. However, when the crystals belonging to the  $\{100\}$  fiber yield, the  $\{100\}$  lattice strains exhibit a downward inflection. The crystals belonging to the  $\{111\}$  fiber for  $r_E = 1.4$  yield on average at the highest macroscopic stress and therefore only the  $\{111\}$  lattice strains exhibit an upward inflection in the elastic-plastic transition regime.

A qualitative difference in the relative behaviors of the crystals of the  $\{100\}$  fiber and the crystals of the  $\{111\}$  fiber occurs at  $r_E = 2.0$  (Figure 1.8). At this value of  $r_E$ , the crystals belonging to the  $\{100\}$  and  $\{111\}$  fibers yield on average at approximately the same macroscopic stress and the  $\{100\}$  and  $\{111\}$  lattice strains both exhibit an upward inflection in the elastic-plastic transition regime (Figure 1.8(a)). Below  $r_E = 2.0$ , crystals of the  $\{100\}$  fiber on average will yield before those of the  $\{111\}$  fiber; above  $r_E = 2.0$ , the opposite is true. The crystals of the  $\{110\}$  and  $\{311\}$  fibers yield on average at a relatively lower macroscopic stress and the  $\{110\}$  lattice strains experience a downward inflec-

tion in the elastic-plastic transition regime, but the downward inflection is less obvious for the  $\{311\}$  lattice strains. In general, the  $\{311\}$  lattice strains are approximately linear with increasing macroscopic stress even after yielding for the range of  $r_E$  of  $r_E = 1.0$  to  $r_E = 3.0$  possibly due to the high multiplicity of the  $\{311\}$  crystal plane normal.

For  $r_E = 3.0$ , the  $\{100\}$  lattice strains rise significantly above the lattice strains exhibited by the other  $\{hkl\}$ s in the elastic-plastic transition leading up to fully-developed plasticity (Figure 1.9(a)). This is also accompanied by the crystals belonging to the  $\{100\}$  fiber yielding on average at the highest macroscopic stress compared to crystals belonging to other fibers. The crystals belonging to the  $\{110\}$  fiber yield on average at the lowest macroscopic stress compared to crystals belonging to other fibers. Yielding of the crystals belonging to the  $\{110\}$  fiber is accompanied by a downward inflection of the  $\{110\}$  lattice strains in the elastic-plastic transition. The  $\{111\}$  and  $\{311\}$  lattice strains exhibit an approximately linear response with increasing macroscopic stress even after yielding.

The upward inflection of the  $\{100\}$  lattice strains is enhanced as  $r_E$  is increased and this phenomenon is accompanied by an increase in the macroscopic stress at which the crystals belonging to the  $\{100\}$  fiber begin to yield on average (Figures 1.6(b), 1.7(b), 1.8(b) and 1.9(b)). Conversely, the downward inflection in the  $\{111\}$  lattice strains is suppressed as  $r_E$  is increased and it is accompanied by the decrease in the macroscopic stress at which crystals belonging to the  $\{111\}$  fiber begin to yield on average.

### **Fully-developed plasticity**

For  $r_E = 1.0$ , it is observed that  $\{111\}$  lattice strains rise above the other  $\{hkl\}$  lattice strains while the  $\{100\}$  lattice strains have the smallest magnitude com-

pared to lattice strains exhibited by the other  $\{hkl\}$ s in the elastic-plastic transition through fully-developed plasticity (Figure 1.6(a)). In general, as  $r_E$  increases, the magnitude of the  $\{111\}$  lattice strains in the fully-developed plasticity regime decreases while the magnitude of the  $\{100\}$  lattice strains increases in the fully-developed plasticity regime. For  $r_E = 1.0$ , the  $\{111\}$  lattice strains are above the lattice strains of the other  $\{hkl\}$ s in the plastic regime whereas for  $r_E = 3.0$ , the  $\{100\}$  lattice strains are above the lattice strains of the other  $\{hkl\}$ s. For a given fiber, the plastic deformation rate magnitude at the maximum level of the macroscopic stress in fully-developed plasticity appears to be independent of  $r_E$ , as seen in Figures 1.6(b), 1.7(b), 1.8(b) and 1.9(b).

In Section 1.6, we demonstrate how the combination of the elastic and plastic properties, which is quantified by the directional strength-to-stiffness ratio, can be used to explain the lattice strain behavior and the average macroscopic stress at which crystals belonging to a crystallographic fiber begins to yield.

### 1.5.3 Evolution of the stress distribution

It is known that in the limit of fully-developed plasticity, the crystal stress tensors of the polycrystal under uniaxial tensile loading rotate towards the vertices of the single crystal yield surface [2, 38]. The single crystal yield surface is the yield condition expressed in stress space [39]. A facet of the yield surface is the yield condition for a single slip system, while a vertex is the intersection of at least five slip systems. Face-centered cubic crystals typically have 6–8 slip systems intersecting at a vertex. The crystal stress state moves toward a vertex of the yield surface because the yield surface vertices can accommodate an arbitrary strain state due to the activation of multiple slip systems at a vertex.

While differences in the single crystal elastic anisotropy leads to differences

in the crystal stress distribution of a polycrystal in the elastic regime, the stress distribution in fully-developed plasticity is not influenced by the single crystal elastic anisotropy. In the limit of fully-developed plasticity, the crystal stresses are highly dependent on the orientation of the crystals because the crystal orientations determine the preferred vertex stresses of the crystals [2].

The stress distribution is examined at three stages of the deformation under uniaxial tension: the elastic regime, the elastic-plastic transition, and fully-developed plasticity regime. The three stages of the deformation are shown as points on the macroscopic true stress-strain curve in Figure 1.10. Although macroscopic stress-strain responses for  $r_E = 1.0$  and  $r_E = 3.0$  are similar, the macroscopic strain that is achieved at the target macroscopic stress of 640 MPa is slightly smaller for  $r_E = 3.0$ .

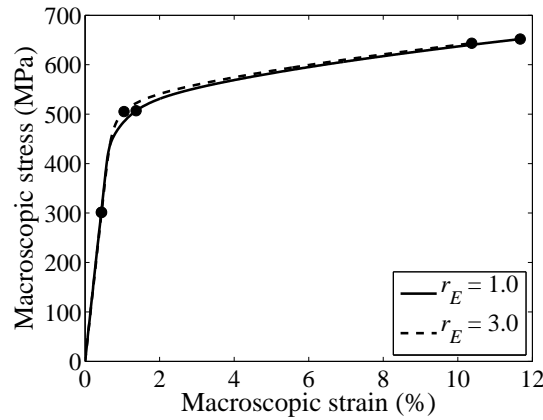


Figure 1.10: Macroscopic true stress-strain curves for  $r_E = 1.0$  and  $r_E = 3.0$ . The points on the curve are at 300 MPa, 500 MPa and 640 MPa which correspond to the linear elastic regime, the elastic-plastic transition regime and the fully-developed plasticity regime respectively.

The axial component of the Cauchy stress,  $\sigma_{zz}$ , in the specimen coordinate frame is plotted as a function of the Rodrigues vector,  $\mathbf{r}$ , over the fundamental region of Rodrigues space in Figure 1.11. The  $\sigma_{zz}(\mathbf{r})$  stress distribution for two

different values of  $r_E$  are shown at the different stages of the deformation, which are denoted in Figure 1.10. The distributions of the other components of the stress tensor have been examined and found to have similar trends as the  $\sigma_{zz}(\mathbf{r})$  stress distributions at the different stages of the deformation.

The axial stress distribution in the elastic regime reflects the difference in  $r_E$ , as seen for  $r_E = 1.0$  in Figure 1.11(a) and  $r_E = 3.0$  in Figure 1.11(b) at 300 MPa. For  $r_E = 1.0$ , the crystals are elastically isotropic and therefore all crystal orientations have the same stress in the elastic regime. For  $r_E = 3.0$ , the  $\langle 100 \rangle$  crystal direction is the most compliant and the  $\langle 111 \rangle$  crystal direction is the stiffest crystal direction. The location of the  $\{100\}$  and  $\{111\}$  crystallographic fibers are shown in Figure 1.3 and the  $\{100\}$  fiber has relatively low axial stress while the  $\{111\}$  fiber has relatively high axial stress. The variability in the stress along a fiber is due to the effect of neighboring crystals.

As the crystals begin yielding in the elastic-plastic transition regime and load redistribution occurs between the crystals, anisotropy in the stress distribution for  $r_E = 1.0$  at 500 MPa appears but there are still differences between the stress distributions for  $r_E = 1.0$  and  $r_E = 3.0$  at this stage of the deformation as shown in Figures 1.11(c) and 1.11(d). The stress distributions in fully-developed plasticity are shown in Figures 1.11(e) and 1.11(f). The stress distributions are very similar for these two values of  $r_E$  because the stress distributions are determined by the vertex stresses of the single crystal yield surface. Crystals belonging to certain crystallographic fibers have preferred families of vertex stresses [2].

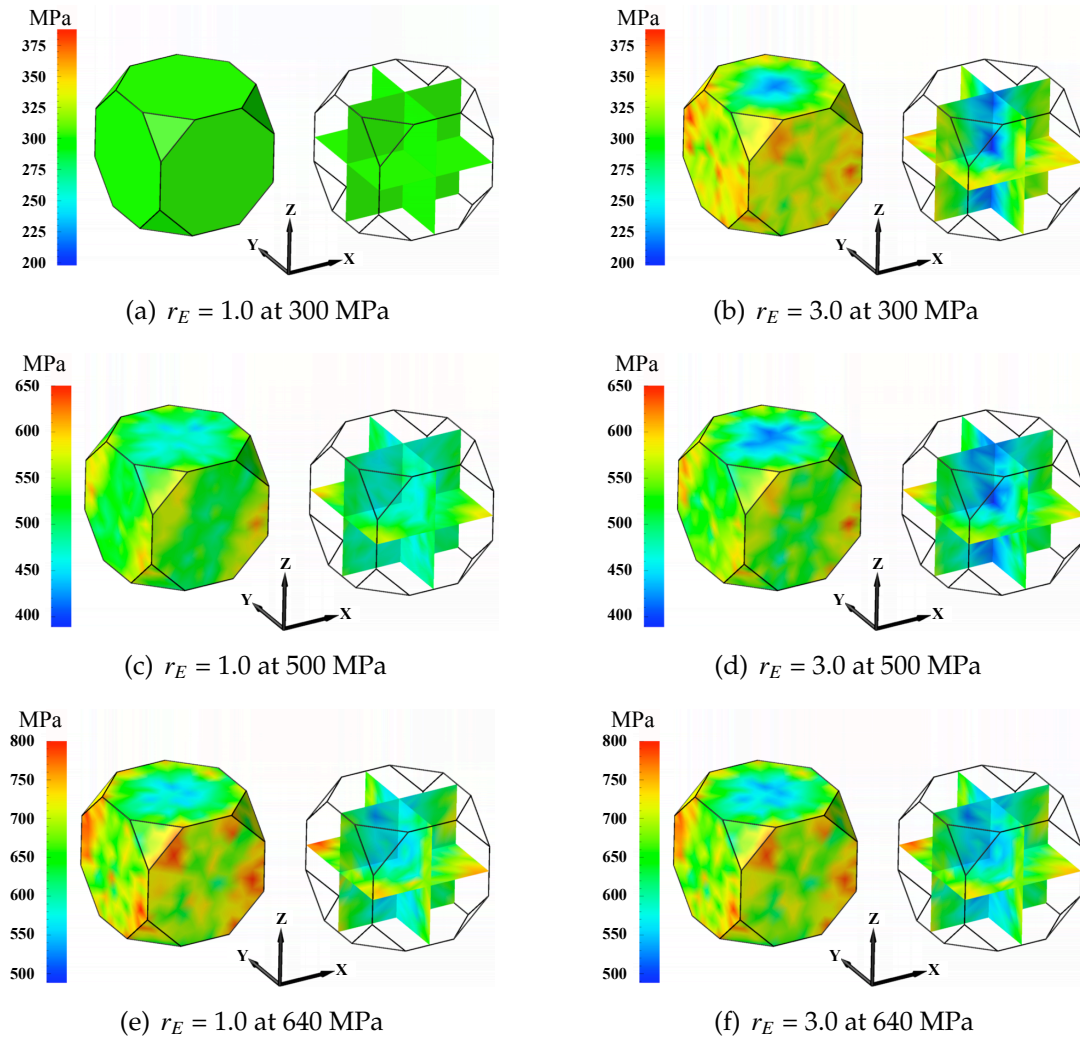


Figure 1.11: Axial stress distribution,  $\sigma_{zz}$ , over the fundamental region. The stress distributions correspond to the macroscopic axial stress levels shown in Figure 1.10.

## 1.6 Role of strength-to-stiffness

In this section, we demonstrate the role of the strength-to-stiffness ratio in determining the evolution of the orientation-dependent lattice strains through the elastic-plastic transition regime and the macroscopic stress level at which yielding begins on average for the crystals belonging to a particular crystallographic fiber.

The hypothesis is that the average directional strength-to-stiffness ratio of the crystals associated with a crystallographic fiber is a good indicator of the relative order of yielding: crystals associated with a crystallographic fiber with higher average strength-to-stiffness should yield at a higher macroscopic stress and conversely, crystals associated with a crystallographic fiber with lower strength-to-stiffness should yield at a lower macroscopic stress.

In Section 1.6.1, a simple structural analog is first introduced to demonstrate the concept of the strength-to-stiffness ratio for two materials with different elastic and plastic properties. This structural analog can be used to show that load accommodation occurs between materials or crystals with different strength-to-stiffness ratios. The directional strength-to-stiffness ratio,  $r_s$ , for a single crystal and a crystallographic fiber, are introduced in Section 1.6.2 and Section 1.6.3, respectively. The directional strength-to-stiffness ratio is used to explain the lattice strains and yield behavior of crystals associated with different crystallographic fibers under uniaxial tensile loading. The average stress tensor of the crystals belonging to a crystallographic fiber is also examined in Section 1.6.4.

### **1.6.1 Structural analog**

An isostrain structural analog is used to illustrate the concept of the strength-to-stiffness ratio. Consider two blocks with identical dimensions but with different Young's modulus ( $E_1$  and  $E_2$ ) and different yield strengths ( $Y_1$  and  $Y_2$ ) loaded in compression between two rigid plates, as shown in Figure 1.12(a). The two materials are assumed to have elastic-perfectly plastic behavior. The blocks experience identical displacement, and therefore identical strains as well.

Because Material 1 has a lower yield strength, we might expect it to yield

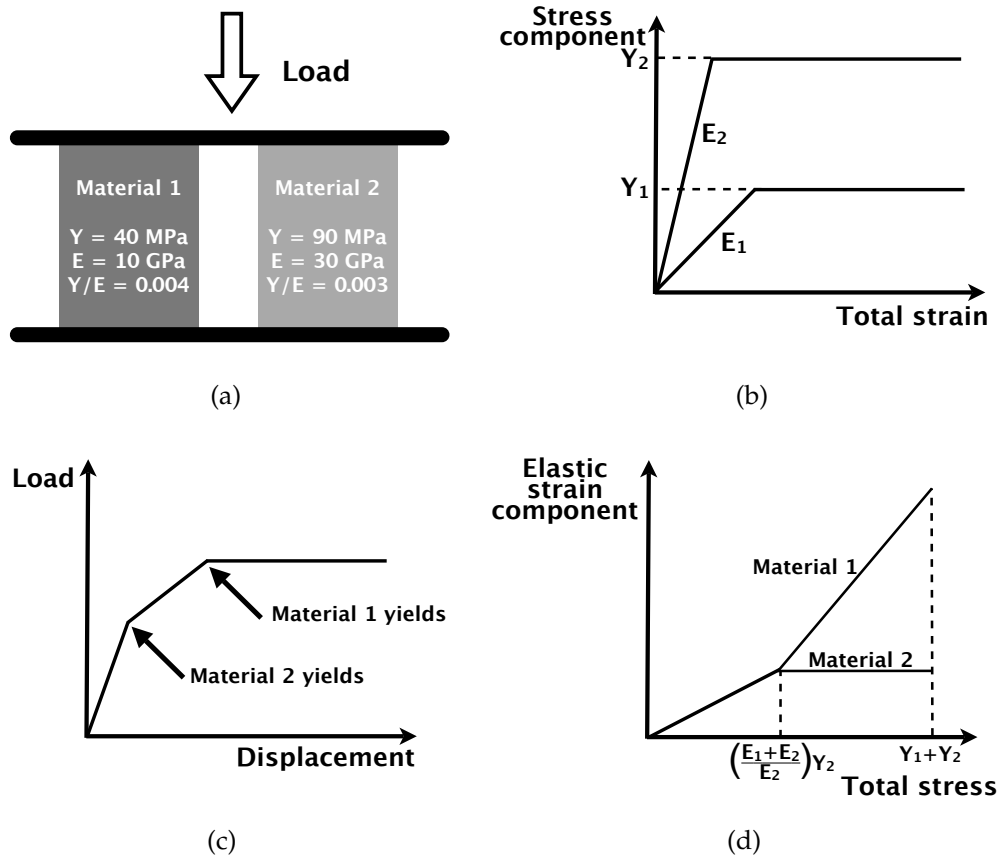


Figure 1.12: (a) Two blocks of identical dimensions but of different materials are loaded in compression between rigid plates which result in an isostrain condition for the two materials; (b) Individual stress-strain response of each material. Material 2 achieves its yield strength before Material 1 under the same strain even though Material 2 has the higher yield strength; (c) Combined load-displacement response of the whole system; (d) Elastic strain for each material as a function of the total stress of the whole system. Initially before either material yields, they both have the same elastic strain.

before Material 2. Figure 1.12(b) is a schematic showing the individual stress-strain response of each material. Under the same strain, Material 2 yields first because by having a higher Young's modulus it reaches its yield strength before Material 1, as shown in Figure 1.12(b). This behavior indicates that the Young's modulus, in addition to the yield strength, determines the relative order the

two materials will yield. Material 2, in fact, has the lower strength-to-stiffness ( $Y/E$ ) ratio and it yields before Material 1. Material 1 has the higher strength-to-stiffness ratio even though it has lower yield strength. Therefore, high  $Y/E$  ratio leads to the material yielding relatively later in a system having elements whose values of  $Y/E$  differ.

The combined load-displacement response for the whole system is shown in Figure 1.12(c). Once Material 2 yields, the effective stiffness of the whole system decreases, which causes the slope of the load-displacement curve to decrease. Because the materials have elastic-perfectly plastic responses, the displacement continues to increase with no increase in load after both materials have yielded. The individual elastic strain response is plotted as a function of the total stress of the whole system in Figure 1.12(d). Both materials experience the same elastic strain up to the point where Material 2 yields. Once Material 2 yields, any additional strain it accumulates is due to plastic strain. After Material 2 yields, Material 1 carries relatively more elastic strain than before Material 2 yielded which demonstrates that load redistribution occurs between the two materials after one of the materials yields.

An isostress structural analog is also considered, where the same two blocks of different materials are arranged in series instead and the whole system is loaded in compression between two rigid plates. Both blocks experience the same axial stress in this configuration. The isostress case is less interesting because the order in which the two different materials yield is determined solely by the relative magnitudes of the yield strength of the materials.

Individual crystals within a polycrystal, due to the effect of neighboring crystals, exhibit yielding behavior somewhere between isostress and isostrain conditions. Comparing Figure 1.12(d) to the lattice strains shown in Fig-

ures 1.6(a), 1.7(a), 1.8(a) and 1.9(a), an upward inflection exhibited by the lattice strains of the  $\{hkl\}$  fiber in the elastic-plastic transition is due to the crystals belonging to the  $\{hkl\}$  fiber yielding later on average. The structural analog indicates that crystals belonging to the fiber that yields relatively later on average are associated with higher strength-to-stiffness ratio compared to crystals belonging to other fibers. For  $r_E = 1.0$ , where the crystals are elastically isotropic, Figure 1.6(b) demonstrates that the average strengths of crystals belonging to different fibers are different. As the single crystal elastic anisotropy is increased, the average elastic stiffnesses of the crystals belonging to different fibers varies, which changes the relative values of the strength-to-stiffness ratio between crystals belonging to different fibers. The directional strength-to-stiffness ratio of the fibers determines the order in which crystals belonging to a fiber yield relative to crystals belonging to other fibers.

## 1.6.2 Directional strength-to-stiffness ratio for a single crystal

For single crystals that exhibit anisotropy in the elastic and plastic behavior, we can quantify the directional strength-to-stiffness ratio under uniaxial tension applied in different directions relative to the crystal lattice. Consider a single cubic crystal with a uniaxial stress component in the the  $\mathbf{d}$  direction of the crystal lattice, where  $\mathbf{d}$  is a function of the angles  $\theta$  and  $\phi$ . The crystal coordinate system is aligned with the three perpendicular directions of the crystal lattice and is denoted by the 123 coordinate axes shown in Figure 1.13. The uniaxial stress component in the  $\mathbf{d}$  direction,  $\tau_d$ , is defined in the  $\hat{\mathbf{d}}\hat{\mathbf{2}}\hat{\mathbf{3}}$  coordinate system. The rotation that aligns the 123 coordinate axes to the  $\hat{\mathbf{d}}\hat{\mathbf{2}}\hat{\mathbf{3}}$  coordinate axes is a rotation of  $\theta$  about the 3 axis, followed by a rotation of  $\phi$  about the  $\hat{\mathbf{2}}$  axis. For cubic symmetry, we need only consider the rotation that aligns the 1 axis with the  $\mathbf{d}$

direction.

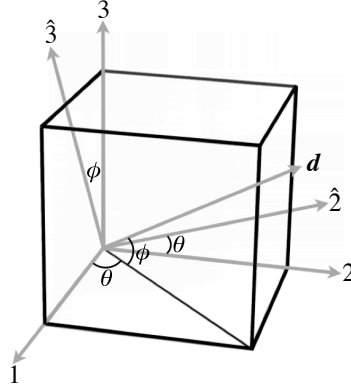


Figure 1.13: Cubic crystal lattice with the uniaxial stress component in the  $\mathbf{d}$  direction,  $\tau_d$ . The 123 coordinate system is aligned with the edges of the crystal lattice, while the stress tensor with the uniaxial stress component in the  $\mathbf{d}$  direction is defined in the  $\hat{\mathbf{d}}\hat{\mathbf{2}}\hat{\mathbf{3}}$  coordinate system.

The slip systems of a crystal are specified by its crystal structure; fcc crystals have  $\{111\}\langle 110 \rangle$  slip systems. The resolved shear stress,  $\tau^\alpha$ , on a slip system is computed as in Equation (1.14). The maximum value of the resolved shear stress among all the slip systems for a given  $\mathbf{d}$ ,  $\tau_d^*$ , normalized by the uniaxial stress component in the  $\mathbf{d}$  direction,  $\tau_d$ , results in the Schmid factor [40]:

$$m_d = \frac{\tau_d^*}{\tau_d} \equiv \frac{\max |\tau^\alpha(\mathbf{d})|}{\tau_d} \quad (1.18)$$

The Schmid factor is plotted over the fundamental orientation triangle as a function of the angles  $\theta$  and  $\phi$  in Figure 1.14(a). The Schmid factor quantifies the propensity of a single crystal to yield under an applied uniaxial stress state in a specified direction  $\mathbf{d}$ . A high value of the Schmid factor indicates that the crystal direction is associated with low strength and will yield earlier. Conversely, low values of the Schmid factor correspond to directions  $\mathbf{d}$  where the slip systems are not favorably oriented for slip and are associated with high strength. The

Schmid factor is independent of the elastic properties of the crystal. The directional strength measure,  $S_d^{\text{crys}}$ , for the direction  $\mathbf{d}$  of a single crystal is therefore defined as:

$$S_d^{\text{crys}} = \frac{1}{m_d} \quad (1.19)$$

The superscript, *crys*, denotes that the directional strength measure is computed for a single crystal under uniaxial tension.

We now define the directional elastic stiffness for a single crystal. Increasing the value of  $r_E$  increases the difference between the directional elastic stiffnesses in the  $\langle 100 \rangle$  and  $\langle 111 \rangle$  crystal directions. The appropriate directional stiffness measure for a single crystal with the uniaxial stress component in the direction  $\mathbf{d}$  is:

$$E_d^{\text{crys}} = \frac{\tau_d}{\epsilon_d} \quad (1.20)$$

where  $\epsilon_d$  is the strain component in the  $\mathbf{d}$  direction. The derivation of  $\epsilon_d$  from  $\tau_d$  and the single crystal elastic moduli is detailed in appendix B. The single crystal directional stiffness over the fundamental orientation triangle is shown for the single crystal elastic moduli of pure aluminum ( $r_E = 1.2$ ) in Figure 1.14(b). The directional stiffness,  $E_d^{\text{crys}}$ , has units of GPa.

Combining Equations (1.19) and (1.20), the directional strength-to-stiffness ratio,  $r_{S,d}^{\text{crys}}$ , for a single crystal under a uniaxial stress state is defined as:

$$r_{S,d}^{\text{crys}} = \frac{S_d^{\text{crys}}}{E_d^{\text{crys}}} \quad (1.21)$$

The directional strength-to-stiffness ratios,  $r_{S,d}^{\text{crys}}$ , for a single crystal under uniaxial stress state for two levels of the single crystal elastic anisotropy,  $r_E = 1.0$  and  $r_E = 3.0$  are shown in Figures 1.14(c) and 1.14(d), respectively. Crystal directions of interest that correspond to the crystallographic fibers shown in Figure 1.3 are indicated on the fundamental orientation triangle in Figures 1.14(c) and 1.14(d).

For  $r_E = 1.0$ , the directional strength-to-stiffness shown in Figure 1.14(c) is the inverse of the Schmid factor shown in Figure 1.14(a) because the crystal is elastically isotropic. For  $r_E = 1.0$ , the  $\langle 111 \rangle$  direction has the highest strength-to-stiffness ratio. For  $r_E = 3.0$ , the directional strength-to-stiffness ratio is shown in Figure 1.14(d) and the  $\langle 100 \rangle$  direction has the highest directional strength-to-stiffness ratio instead.

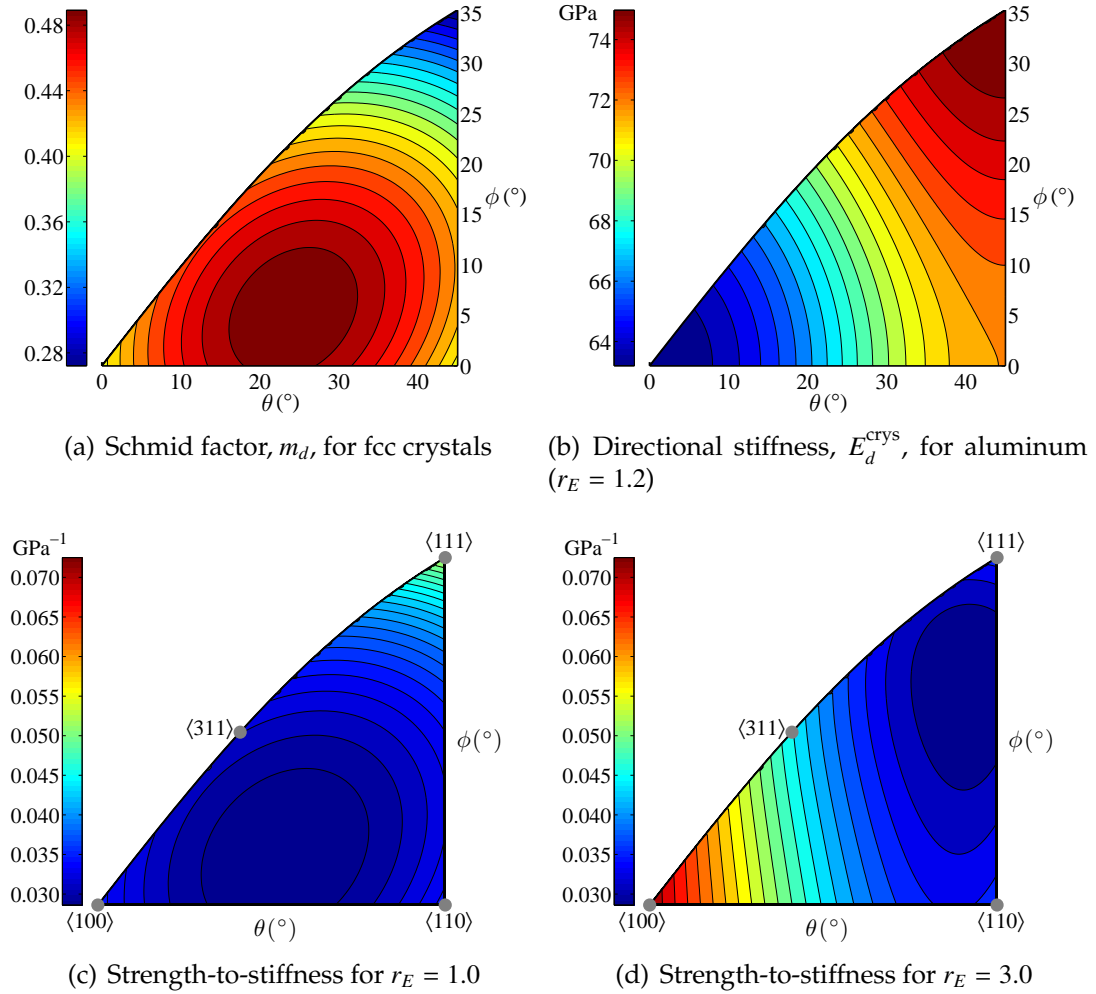


Figure 1.14: (a) Schmid factor,  $m_d$ , for fcc crystals plotted on the fundamental orientation triangle. (b) Directional elastic stiffness,  $E_d^{\text{crys}}$ , for pure aluminum ( $r_E = 1.2$ ) plotted on the fundamental orientation triangle. (c) Directional strength-to-stiffness ratio,  $r_{s,d}^{\text{crys}}$ , for  $r_E = 1.0$ . (d) Directional strength-to-stiffness ratio,  $r_{s,d}^{\text{crys}}$ , for  $r_E = 3.0$ .

Figure 1.15 shows the directional strength-to-stiffness corresponding to several  $\langle hkl \rangle$  directions of interest for increasing values of  $r_E$ . The directional strength-to-stiffness values shown in Figure 1.15 are computed using the single crystal elastic moduli in Table 1.1. As  $r_E$  increases, the strength-to-stiffness of the  $\langle 100 \rangle$  direction increases while the strength-to-stiffness of the  $\langle 111 \rangle$  direction decreases. The strength-to-stiffness of the  $\langle 110 \rangle$  direction remains approximately at the same level as  $r_E$  increases and the strength-to-stiffness of the  $\langle 311 \rangle$  direction increases slightly with  $r_E$ .

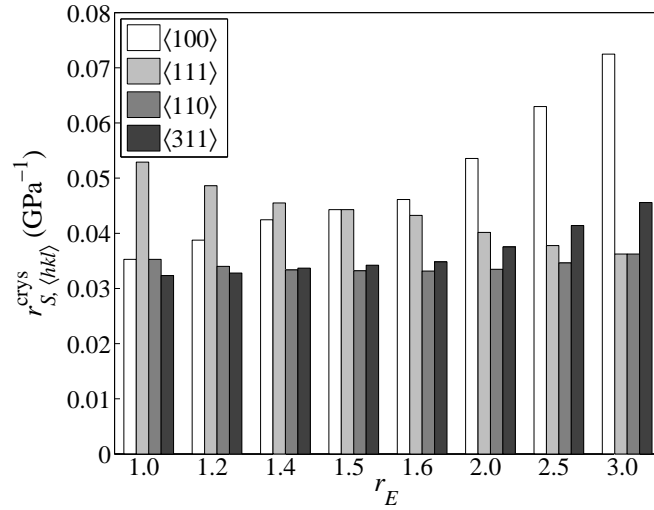


Figure 1.15: Directional strength-to-stiffness ratio,  $r_{S,\langle hkl \rangle}^{\text{crys}}$ , computed for a single crystal under uniaxial tension.

The lattice strains and plastic deformation rate magnitudes shown in Figures 1.7–1.9 are averaged among crystals belonging to the  $\{hkl\}$  fibers and these crystals do not necessarily have uniaxial stress states due to the interactions between neighboring crystals. For  $r_E = 1.0$ , however, the macroscopic stress and the crystal level stress are the same in the elastic regime because of the isotropic nature of the elastic response. Therefore, the directional strength-to-stiffness ratio should predict exactly which sets of crystals belonging to the crystallo-

graphic fibers will yield first for  $r_E = 1.0$ . Figure 1.6(b) shows that crystals belonging to  $\{311\}$  fiber yield on average at the lowest macroscopic stress while the crystals belonging to the  $\{111\}$  fiber yield on average at a much higher macroscopic stress relative to crystals belonging to other fibers. The crystals belonging to  $\{100\}$  and  $\{110\}$  fibers yield on average at approximately the same macroscopic stress. Comparing the average macroscopic stress at which crystals belonging to different fibers yield (Figure 1.6(b)) to the directional strength-to-stiffness (Figure 1.15) for  $r_E = 1.0$ , crystals belonging to fibers with relatively higher strength-to-stiffness yield at higher macroscopic stresses while crystals belonging to fibers with relatively lower strength-to-stiffness yield at lower macroscopic stresses.

Although elastically anisotropic crystals in the polycrystal may not exhibit uniaxial stress states, we will examine the directional strength-to-stiffness ratio of a single crystal under uniaxial tension in relation to the average macroscopic stress at which crystals belonging to a fiber begin to yield. The most prominent trend that is observed is that  $r_{S,\langle 100 \rangle}^{\text{crys}}$  increases with increasing  $r_E$ , while  $r_{S,\langle 111 \rangle}^{\text{crys}}$  decreases with increasing  $r_E$ , as shown in Figure 1.15. With increasing  $r_E$ , the macroscopic stress at which the crystals belonging to the  $\{100\}$  fiber yield on average increases relative to crystals belonging to other fibers. In contrast, the macroscopic stress at which crystals belonging to the  $\{111\}$  fiber yield on average decreases relative to crystals belonging to other fibers. These trends are evident in Figures 1.6(b), 1.7(b), 1.8(b) and 1.9(b). There is less change in the average macroscopic yield stress of the crystals belonging  $\{110\}$  and  $\{311\}$  fibers with increasing  $r_E$ , which is reflected in the values of  $r_{S,\langle 110 \rangle}^{\text{crys}}$  and  $r_{S,\langle 311 \rangle}^{\text{crys}}$  with increasing  $r_E$ .

The single crystal directional strength-to-stiffness is generally able to pre-

dict that increasing strength-to-stiffness corresponds to increasing macroscopic stress at which crystals belonging to a fiber yield on average, and that decreasing strength-to-stiffness corresponds to decreasing macroscopic stress at which crystals belonging to a fiber yield on average. For  $r_E = 1.5$ , the single crystal directional strength-to-stiffness for the  $\langle 100 \rangle$  and  $\langle 111 \rangle$  directions have similar values, as evident in Figure 1.15. However, crystals belonging to  $\{100\}$  and  $\{111\}$  fibers yield on average at approximately the same macroscopic stress when  $r_E = 2.0$ , as evident in Figure 1.8(b). This indicates that in general, the simple analytical model of a single crystal under uniaxial tension is able to predict which crystals belonging to a fiber will yield first at low and high values of  $r_E$ , such as for  $r_E = 1.0$  and  $r_E = 3.0$ , rather than at moderate values of  $r_E$ , such as  $r_E = 1.5$ .

### 1.6.3 Directional strength-to-stiffness ratio for a crystallographic fiber of the polycrystal

The computation of a directional strength-to-stiffness ratio for a crystallographic fiber is complicated by the fact that the crystals in the virtual polycrystal that belong to a crystallographic fiber do not necessarily exhibit uniaxial stress states.

The plastic flow rule is computed in Equation (1.12) for each crystal. The crystal stress drives the rate of shearing on each slip system. The Taylor factor quantifies the magnitude of the slip system shearing rates relative to the effective strain rate experienced by the crystal that takes place for the least expenditure of work. The Taylor factor of the  $\{hkl\} \parallel [001]$  crystallographic fiber is defined as:

$$M_{\{hkl\}}^{\text{fiber}} = \left( \frac{\sum_{\alpha} |\dot{\gamma}^{\alpha}|}{D_{\text{eff}}} \right)_{\{hkl\}} \quad (1.22)$$

where  $D_{\text{eff}}$  is the effective deformation rate experienced by a crystal. The sub-

script  $\{hkl\}$  denotes that the quantity is averaged among all crystals belonging to the  $\{hkl\} \parallel [001]$  crystallographic fiber.

In fully-developed plasticity, plastic flow occurs at a constant rate and the crystals stresses are expected to be invariant with increasing plastic strain in the absence of hardening. Crystals with certain orientations will experience more shearing on the slip systems relative to the strain rate experienced by the crystal. The Taylor factors computed from the simulation data for different crystallographic fibers are shown in Figure 1.16 for  $r_E = 1.0$  and  $r_E = 3.0$ . It is observed from Figure 1.16 that in fully-developed plasticity, the Taylor factors corresponding to different crystallographic fibers approach steady-state values. The Taylor factors vary between the two levels of elastic anisotropy in the elastic-plastic transition regime but at relatively large macroscopic strains in fully-developed plasticity, the Taylor factors are independent of the elastic anisotropy. Since the simulation is run under load control, the macroscopic strains achieved at the final target load are different between the two values of  $r_E$ , as shown in Figure 1.16.

The directional strength of the  $\{hkl\} \parallel [001]$  crystallographic fiber,  $S_{\{hkl\}}^{\text{fiber}}$ , is defined as the steady-state value of the Taylor factor achieved in fully-developed plasticity. The average directional strength of the crystals belonging to a crystallographic fiber is taken as the final value of the Taylor factor achieved at the nominal macroscopic stress of 580 MPa, which is the maximum engineering macroscopic stress in the simulation.

$$S_{\{hkl\}}^{\text{fiber}} = M_{\{hkl\}}^{\text{fiber}} \text{ in fully-developed plasticity} \quad (1.23)$$

The directional stiffness for a crystallographic fiber is computed using the same definition as the single crystal definition in Equation (1.20). The components of the Kirchhoff stress for the crystals belonging to each crystallographic

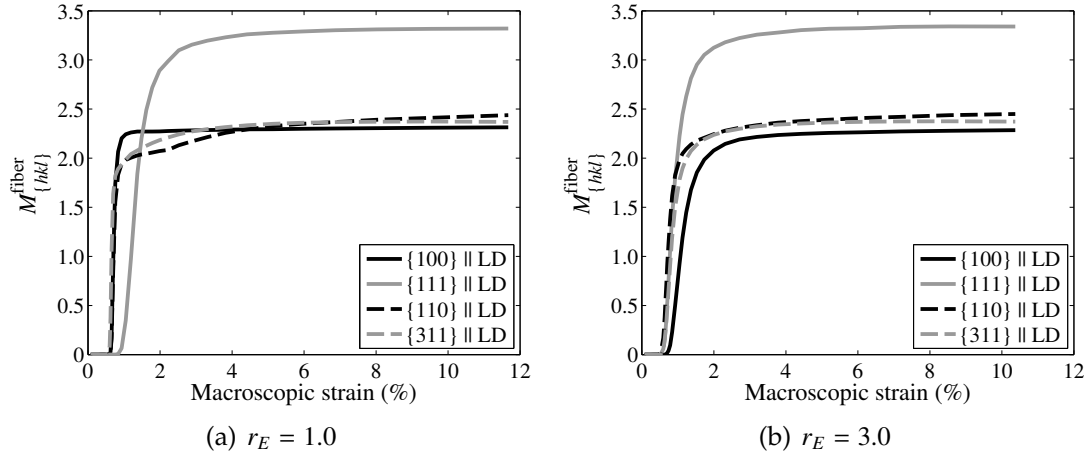


Figure 1.16: The Taylor factor,  $M_{\{hkl\}}^{\text{fiber}}$ , for different crystallographic fibers at two levels of the single crystal elastic anisotropy,  $r_E$ . The abscissa corresponds to the macroscopic true strain. In fully-developed plasticity, the Taylor factors approach a steady-state value and are independent of the single crystal elastic anisotropy.

fiber are transformed to the specimen coordinate system. Since the uniaxial tensile loading is applied in the specimen Z direction, the elastic stiffness for each crystal is computed as the ratio of the Kirchhoff stress component in the Z-direction to the elastic strain component in the Z-direction, and then averaged for all crystals belonging to the crystallographic fiber in the elastic regime:

$$E_{\{hkl\}}^{\text{fiber}} = \left( \frac{\tau_{zz}}{\epsilon_{zz}} \right)_{\{hkl\}} \quad \text{in the elastic regime} \quad (1.24)$$

where  $\{hkl\}$  denotes that the ratio  $(\tau_{zz}/\epsilon_{zz})$  is computed for each crystal belonging to the  $\{hkl\} \parallel [001]$  crystallographic fiber, and then averaged among all crystals belonging to the fiber.

The Kirchhoff stress instead of the Cauchy stress is used in the definition of the directional elastic stiffness,  $E_{\{hkl\}}^{\text{fiber}}$ , because  $E_{\{hkl\}}^{\text{fiber}}$  will then be independent of the macroscopic stress in the elastic regime. Recall that the Cauchy stress is related to the Kirchhoff stress by the equation  $\tau = \det(1 + \epsilon)\sigma$ . If the Cauchy

stress is used in the definition of  $E_{\{hkl\}}^{\text{fiber}}$ , the directional elastic stiffness will decrease with increasing macroscopic stress in the elastic regime. It is important to compute a definition of  $E_{\{hkl\}}^{\text{fiber}}$  that is independent of the macroscopic stress in the elastic regime.

The average value of  $(\tau_{zz}/\epsilon_{zz})_{\{hkl\}}$  for a crystallographic fiber is plotted as a function of the macroscopic stress for  $r_E = 1.0$  and  $r_E = 3.0$  in Figure 1.17. As expected, the values of  $(\tau_{zz}/\epsilon_{zz})_{\{hkl\}}$  are constant in the elastic regime. Once yielding begins, load redistribution occurs between crystals belonging to different crystallographic fibers and the values of  $(\tau_{zz}/\epsilon_{zz})_{\{hkl\}}$  are no longer constant. The directional elastic stiffness for a fiber,  $E_{\{hkl\}}^{\text{fiber}}$ , is therefore only valid in the elastic regime before yielding occurs.

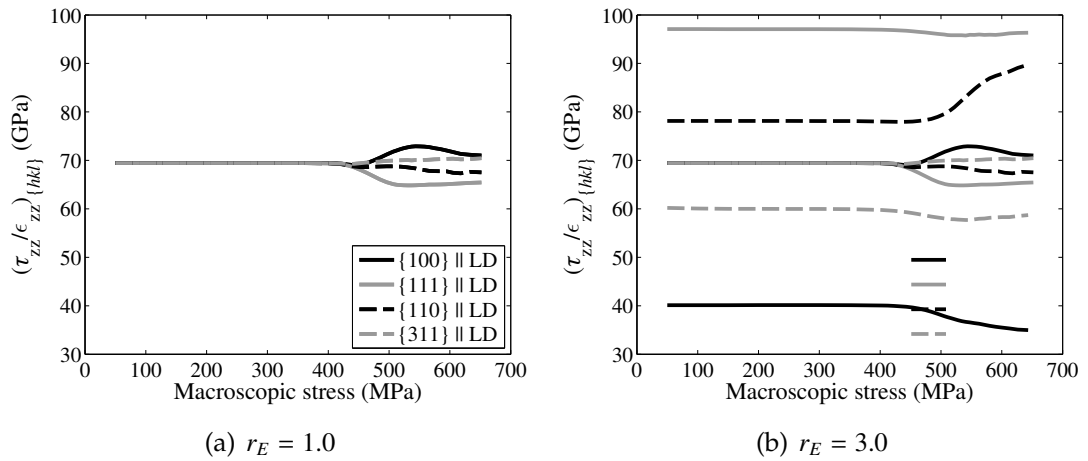


Figure 1.17:  $(\tau_{zz}/\epsilon_{zz})_{\{hkl\}}$  for different crystallographic fibers at two levels of the single crystal elastic anisotropy,  $r_E$ . The abscissa corresponds to the macroscopic true stress.

Combining Equations (1.23) and (1.24), the resulting definition of the directional strength-to-stiffness ratio of a crystallographic fiber is:

$$r_{S,\{hkl\}}^{\text{fiber}} = \frac{S_{\{hkl\}}^{\text{fiber}}}{E_{\{hkl\}}^{\text{fiber}}} \quad (1.25)$$

The average directional strength-to-stiffness ratio is computed for the crystals

belonging to a fiber using Equation (1.25) and the resulting values are shown in Figure 1.18 as a function of the single crystal elastic anisotropy. The error bars indicate the standard deviation in the strength-to-stiffness ratio among the crystals belonging to a crystallographic fiber due to the effect of neighboring crystals. Comparing the directional strength-to-stiffness trends in Figure 1.18 to the average macroscopic stress at which crystals associated with a fiber begin to yield (Figures 1.6(b)–1.9(b)), it is observed that the directional strength-to-stiffness is better at predicting the onset of yielding at extreme values of  $r_E$ , such as at  $r_E = 1.0$  and  $r_E = 3.0$ . At moderate values of  $r_E$ , the difference between the strength-to-stiffnesses of crystals belonging to the  $\{100\}$  and  $\{111\}$  fibers is within the standard deviation of the crystals belonging to the fiber. Crystals belonging to the  $\{100\}$  and  $\{111\}$  fibers have similar strength-to-stiffness values in the range of  $r_E = 1.4$ – $1.6$ , as evident in Figure 1.18. This indicates that at moderate values of  $r_E$ , the effect of neighboring grains is as significant as the directional strength-to-stiffness in determining when the crystals begin to yield.

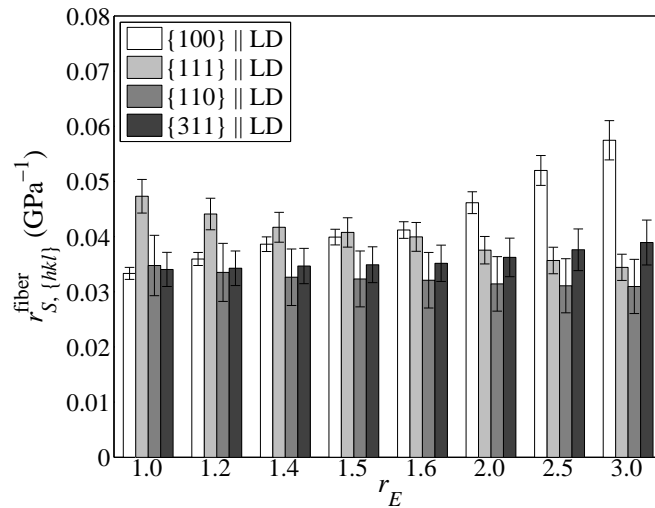


Figure 1.18: Directional strength-to-stiffness ratio,  $r_{S, \{hkl\}}^{\text{fiber}}$ , computed for several crystallographic fibers.

It is observed that the directional strength-to-stiffness for a single crystal (Figure 1.15) and the strength-to-stiffness for the crystallographic fiber (Figure 1.18) appear to have very similar trends. Both  $r_{S,\langle 100 \rangle}^{\text{crys}}$  and  $r_{S,\{100\}}^{\text{fiber}}$  increase with increasing  $r_E$ , while  $r_{S,\langle 111 \rangle}^{\text{crys}}$  and  $r_{S,\{111\}}^{\text{fiber}}$  both decrease with increasing  $r_E$ . Although the single crystal strength-to-stiffness is computed for a single crystal under a uniaxial stress state while the strength-to-stiffness for a crystallographic fiber is computed for many crystals which have multiaxial stress states, the trends in the strength-to-stiffness appear to be very similar between Figure 1.15 and Figure 1.18. The average of the stress tensor along a fiber is examined in more detail in the following section.

A suite of simulations have also been conducted for the range of  $r_E = 1.0\text{--}3.0$  without slip system strengthening and reorientation. The directional strength-to-stiffness ratio for a crystallographic fiber is not influenced by the rate of hardening because the directional strength measure,  $S_{\{hkl\}}^{\text{fiber}}$ , in Equation (1.23) is computed in fully-developed plasticity, while the directional stiffness measure,  $E_{\{hkl\}}^{\text{fiber}}$ , in Equation (1.24) is computed in the elastic regime only. The results are not presented here because the exclusion of slip system hardening and reorientation does not significantly change either the order in which crystals belonging to different fibers yield or the average directional strength-to-stiffness ratios of the crystals belonging to a fiber.

#### 1.6.4 Average stress of a crystallographic fiber

For the crystals belonging to the  $\{hkl\} \parallel [001]$  crystallographic fiber, the Kirchhoff stress tensors,  $\tau$ , of these crystals are averaged to obtain the average Kirchhoff stress tensor,  $\tau^{\text{fiber}}$ , in the specimen coordinate frame. Each component of the fiber-averaged Kirchhoff stress tensor is normalized by the axial component,

$\tau_{zz}^{\text{fiber}}$ . The results are shown in Figures 1.19 and 1.20 for different crystallographic fibers in the elastic regime and in the fully-developed plasticity regime, respectively.

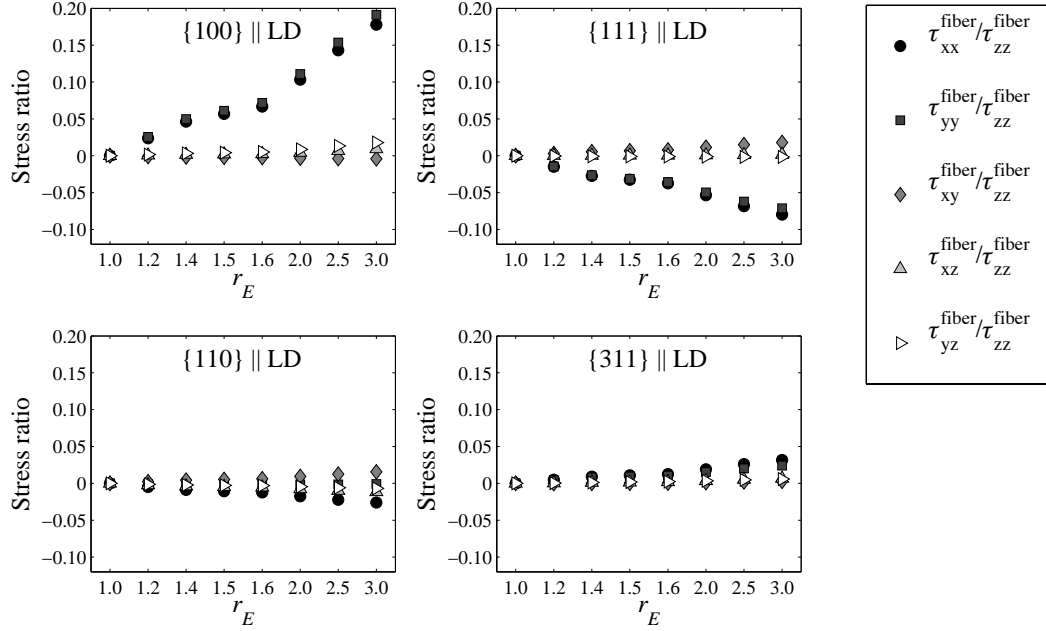


Figure 1.19: Non-axial components of the average Kirchhoff stress tensor for a crystallographic fiber, normalized by the axial stress component,  $\tau_{zz}^{\text{fiber}}$ , in the elastic regime.

Figure 1.19 shows that the average stress tensor of a crystallographic fiber in the elastic regime increasingly deviates from a uniaxial stress state as  $r_E$  increases. The diagonal components,  $\tau_{xx}^{\text{fiber}}$  and  $\tau_{yy}^{\text{fiber}}$ , increase as a proportion of the axial component,  $\tau_{zz}^{\text{fiber}}$ , with increasing  $r_E$ , while the shear components are relatively small compared to the diagonal components. The fiber-averaged stress tensor of the {100} fiber has the largest deviation from a uniaxial stress state compared to the fiber-averaged stress tensors of the other fibers and this deviation increases with increasing  $r_E$ . The average volumetric stress of the {100} fiber increases with  $r_E$  but the elastic stiffness definition for a fiber, which is shown in Equation (1.24), only takes into account the Kirchhoff stress and elastic strain

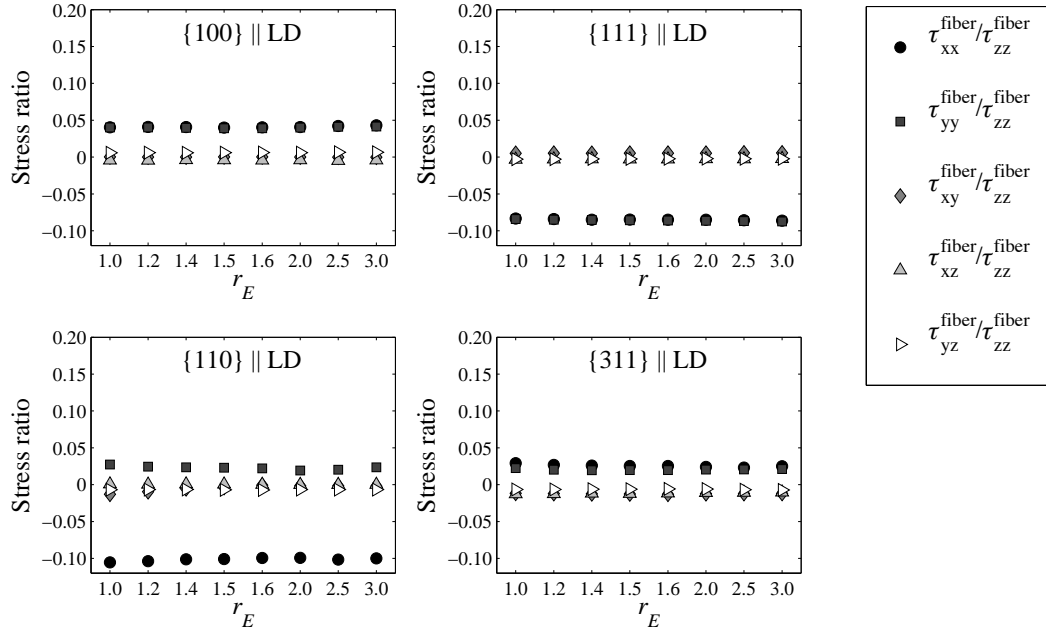


Figure 1.20: Non-axial components of the average Kirchhoff stress tensor for a crystallographic fiber, normalized by the axial stress component,  $\tau_{zz}^{\text{fiber}}$ , in the fully-developed plasticity regime.

components in the loading direction. However, the average stress components of the {111}, {110} and {311} fibers are only a small fraction of the  $\tau_{zz}^{\text{fiber}}$  component, which indicates that the fiber-averaged stress tensors do not deviate significantly from a uniaxial stress state. The results in Figure 1.19 are consistent with the axial stress distributions,  $\sigma_{zz}(\mathbf{r})$ , over the fundamental region in the elastic regime (Figures 1.11(a) and 1.11(b)), which indicates that the stress distributions are highly dependent on  $r_E$  in the elastic regime leading up to yielding.

The average stress tensor of a crystallographic fiber, however, does not show any dependence on the single crystal elastic anisotropy in fully-developed plasticity, as shown in Figure 1.20. The results in Figure 1.20 are consistent with the axial stress distributions,  $\sigma_{zz}(\mathbf{r})$ , over the fundamental region in fully-developed plasticity, which are shown in Figures 1.11(e) and 1.11(f).

## 1.7 Conclusion

A suite of finite element simulations was conducted to examine the effect of varying the single crystal elastic anisotropy on the lattice strain evolution of a fcc virtual polycrystal under uniaxial tensile loading. The evolution of the average response of crystals belonging to different crystallographic fibers was examined in the elastic-plastic transition regime leading up to fully-developed plasticity. The evolution of the lattice strains show markedly different behaviors for different values of the single crystal elastic anisotropy because crystals belonging to different crystallographic fibers begin yielding on average at different levels of the macroscopic stress. The orientation dependence of when different sets of crystals begin to yield on average is due to differences in the directional strength-to-stiffness ratio of crystals belonging different crystallographic fibers. The crystal lattice strains demonstrate that yielding is influenced by the combination of the elastic and plastic anisotropies of the crystal. At extremely low or high values of the single crystal elastic anisotropy, crystals associated with a fiber with higher average strength-to-stiffness will yield at a higher macroscopic stress and conversely, crystals associated with a fiber with lower strength-to-stiffness will yield at a lower macroscopic stress. At moderate values of single crystal elastic anisotropy, the influence of the directional strength-to-stiffness ratio is weaker due to the effect of neighboring crystals. Although the onset of yielding is influenced by the single crystal properties, the stress distribution in fully-developed plasticity is independent of the single crystal elastic properties. The stress distribution in fully-developed plasticity is determined by the single crystal yield surface.

CHAPTER 2  
EVOLUTION OF THE CRYSTAL STRESS DISTRIBUTIONS IN  
FACE-CENTERED CUBIC POLYCRYSTALS SUBJECTED TO CYCLIC  
LOADING

## 2.1 Abstract

Due to the heterogeneous nature of polycrystalline metals, the stress distribution at the crystal level is influenced by the complex interplay of factors such as the orientations of the crystal lattices, the elastic and plastic mechanical properties, the interactions between neighboring crystals, and the type of loading conditions. In this chapter, we investigate the evolution of the crystal scale stress and elastic strain distributions under cyclic loading. More specifically, we examine the orientation dependent lattice strains in face-centered cubic (fcc) polycrystals under fully-reversed, strain-controlled cyclic loading using a cyclic hardening model implemented within a crystal-based finite element formulation. The directional strength-to-stiffness ratio and the single crystal yield surface (SCYS) topology are used to provide a quantitative explanation of the observed hysteresis behavior when the lattice strains are plotted as a function of the macroscopic stress. The directional strength-to-stiffness ratio influences the progression of yielding in the elastic-plastic transition regime, leading to a non-linear response in the elastic-plastic transition regime and causing hysteresis behavior in the macroscopic stress versus lattice strain curves. The lattice strains after the elastic-plastic transition regime are influenced by the single crystal elastic moduli and the facet/vertex attributes of the SCYS. We found that the same trends hold in the absence of slip system hardening and in the presence of a strong rolling texture.

## 2.2 Introduction

Recent advances in both diffraction methods and polycrystal deformation modeling have enabled researchers to better quantify stresses and strains at the crystal level. Using diffraction methods it is possible to measure elastic lattice strains within crystals under *in situ* loading. With parallel computing and data parallel implementations of structural codes, it is possible to construct and load polycrystalline aggregates with thousands of crystals, each crystal highly resolved by many finite elements. These advances offer the promise to develop a quantitative link between macroscopic loading and spatial distribution of stress at the microstructural (crystal) scale under cyclic loading. Crystals within a polycrystalline aggregate tend not to share an applied load equally, but rather exhibit individual and heterogeneous responses that are dependent on the crystallographic orientation, the single crystal elastic and plastic anisotropy, and the interactions with neighboring crystals. It is generally accepted that these factors all play roles in determining crystal-scale stress distributions under cyclic loading, especially for the regime associated with low-cycle fatigue. However, a clear explanation is elusive due to the complexities of the modes and mechanisms of cyclic deformations.

To this end, it is instructive to examine the heterogeneous nature of the crystal stresses with respect to the anisotropy inherent in the single crystal properties. A specific goal is to identify correlations between the single crystal properties and the orientation dependence of the crystal stresses in the presence of equilibrium and compatibility constraints associated with grain interactions. In particular we examine two specific attributes of crystals: the directional strength-to-stiffness ratio and the single crystal yield surface (SCYS) topology. The directional strength-to-stiffness is an important metric for the relative load

sharing among crystals of a polycrystal, especially in the elastic-plastic transition. The yield surface constrains the stress tensor, both in magnitude and direction, and as with the directional strength-to-stiffness its topology affects the nature of the distributions of stress among crystals. As will be presented here, both of these attributes have important roles with respect to cyclic loading behavior.

The directional strength-to-stiffness provides a quantitative basis to explain the observed average lattice strains of crystals when loading proceeds into the elastic-plastic transition regime [1]. The orientation dependent lattice strain response observed in the elastic-plastic transition regime, typically referred to as intergranular strains, arise due to different sets of crystals yielding at different levels of the macroscopic stress. Load redistribution occurs between crystals of different orientations when some crystals begin to yield, forcing crystals that remain elastic to carry an increased proportion of the applied stress. The joint role of the elastic stiffness (elastic anisotropy) and yield strength (plastic anisotropy) on the development of these intergranular strains can be quantified using the directional strength-to-stiffness ratio. In general, crystals within a polycrystalline aggregate with lower directional strength-to-stiffness tend to yield before crystals with higher directional strength-to-stiffness. Here we demonstrate that the directional strength-to-stiffness ratio is a parameter that can be used to link the single crystal anisotropic properties and load sharing among differently orientated crystals acting collectively during cyclic loading.

Over a wide range of temperatures and strain rates, crystals deform plastically by restricted slip on prescribed slip systems in prescribed directions [41]. The yield condition for a slip system can be described as a plane in five dimensional (deviatoric) stress space and the rate-independent SCYS is the inner

envelope of the set of planes defined by all the slip systems of the single crystal [38]. A vertex of the SCYS is defined as the intersection of at least five of the slip system planes. For rate-dependent behavior, the SCYS depends on strain rate and temperature. The rate dependent surfaces lie within the rate independent surface, but for materials with low rate dependence, the two surfaces are close. During deformation that includes slip, the SCYS is actively influencing the stress. As the stress level within a crystal rises, the number of slip systems activated increases, beginning with only one or two and eventually activating the number associated with a vertex of the SCYS, a condition referred to as polyslip [42]. The crystal stress direction changes as the number of constraints from activated slip systems increases. Once the stress aligns with a vertex of the SCYS and all potentially active the slip systems have been activated, plastic flow is fully developed. The influence of the vertices of the SCYS on the crystal stress distributions in fully-developed plasticity has previously been discussed by Ritz et al. [2] for monotonic loading. Under cyclic loading, fully developed plasticity may not be reached before the loading reverses. Nevertheless, the topology of the SCYS influences the stress as soon as the stress exceeds the elastic limit and thus plays an important role in cyclic as well as monotonic loading behaviors.

The directional strength-to-stiffness and the SCYS topology will be used to better understand stress distributions in polycrystals subjected to cyclic loading. Both are useful in quantifying the influence of crystal anisotropy on the orientation dependence of the stress distribution in the presence of grain interactions. The grain interactions arise due to requirements of equilibrium of forces and compatibility of motion, which are enforced in the modeling by means of a well-established finite element formulation. To demonstrate the concepts, we

focus on providing a well-grounded explanation of the orientation dependence of lattice strains observed in cyclic loading, especially their evolution over loading cycles.

### 2.3 Experimental observations

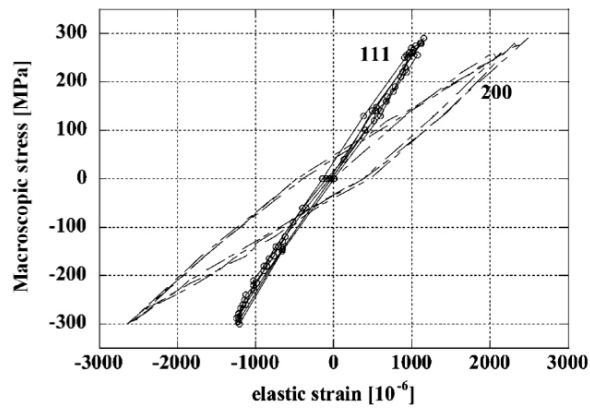
Diffraction methods have the ability to interrogate the elastic lattice strains within crystals with orientations associated with a particular crystallographic fiber. Since the elastic strains in crystals are directly related to the stresses through Hooke's law, diffraction experiments offer direct insight into the heterogeneous nature of the crystal stress distribution within a polycrystalline aggregate. Although many experimental studies measuring the evolution of lattice strains under monotonic tensile loading have been conducted on different types of polycrystalline materials [11, 14–16, 18, 24], the number of studies involving lattice strain diffraction measurements of polycrystalline materials under fully-reversed cyclic loading is very limited. Neutron diffraction has been used to measure the residual lattice strains in stainless steel under fully-reversed, high cyclic fatigue loading in load control [43, 44]. High energy synchrotron x-rays have been used to track the evolution the lattice strains associated with a few crystallographic fibers under fully-reversed cyclic loading in load control [45]. There have also been several studies based on using neutron diffraction techniques to measure the lattice strains for a limited number of crystallographic fibers under *in-situ*, fully-reversed, low cycle fatigue loading in strain control [46–49].

Examples of lattice strain data from fully-reversed cyclic loading experiments that are relevant to our current numerical study are presented in Fig-

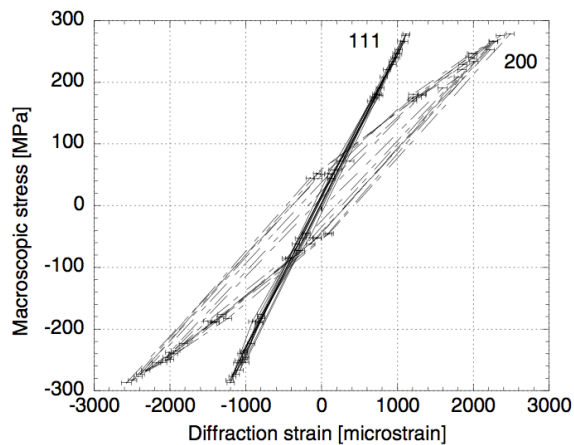
ure 2.1. The lattice strain measurements shown in Figure 2.1 were obtained from neutron diffraction experiments conducted by Lorentzen et al. [46] and Korsunsky et al. [47] on stainless steel under fully-reversed cyclic loading. Lorentzen et al. [46] measured the lattice strains for several crystallographic fibers aligned with the axial and transverse specimen directions in stainless steel under fully-reversed cyclic loading. The experiment was conducted in incremental load control and the specimen was cycled at a fixed strain amplitude of  $\pm 0.4\%$  for eight complete cycles. Diffraction measurements were conducted at 24 load increments throughout the cycle. Korsunsky et al. [47] used time-of-flight neutron diffraction to measure the lattice strains corresponding to two crystallographic fibers with the crystal directions aligned with the specimen axial loading direction for AISI 316L stainless steel. Two specimens were cycled at strain amplitudes of 0.25% and 0.44% in fully-reversed strain controlled cycling. Lattice strain measurements were conducted at eight macroscopic strain levels on each cycle.

The measured lattice strains shown in Figure 2.1, where the crystal directions are aligned with the specimen loading direction, exhibit an orientation dependent response over the course of a cycle. The lattice strains in crystals having  $\{111\}$  plane normals aligned with the specimen loading direction exhibit a close to linear response with increasing macroscopic stress. The lattice strains for crystals having  $\{200\}$  plane normals aligned with the specimen loading direction, on the other hand, exhibit significant hysteresis. The experimental data shown in in Figure 2.1 are an important example of how the lattice strains varying at the crystal level need to be explained in a consistent manner with respect to the single crystal anisotropic properties as part of any micromechanical description of fatigue processes.

These experimental results motivate our investigation into the orientation dependent nature of load sharing during cyclic loading from the perspective of how the directional strength-to-stiffness and the SCYS topology influence the grain interactions and give rise to the behavior characterized by Figure 2.1. We also examine the effect of texture and strain hardening on the progression of yielding through the elastic-plastic transition and on the evolution of the lattice strains during cyclic loading.



(a) Lorentzen, Daymond, Clausen & Tome (2002) [46]



(b) Korsunsky, James & Daymond (2004) [47]

Figure 2.1: Lattice strains of crystals with the  $\{111\}$  and  $\{200\}$  lattice plane normals aligned with the axial loading direction for stainless steel specimens under fully reversed cyclic loading between fixed strain limits.

## 2.4 Methodology

A crystal-based elastoplastic constitutive model implemented within a finite element framework is used to simulate the response of polycrystals under fully-reversed strain-controlled cyclic loading. A complete description of the constitutive model and its implementation within a finite element framework can be found in Refs. [35, 36, 50]. The capabilities of the crystal elastoplastic constitutive model are only briefly summarized here:

- multiplicative decomposition of the crystal deformation gradient into elastic, plastic and rotational portions
- anisotropic elasticity appropriate to the fcc crystal structure
- plastic deformation by rate-dependent restricted slip on the 12  $\{111\}\langle 110\rangle$  slip systems associated with the fcc crystal structure
- strain hardening with pseudosaturation under cyclic loading
- texture evolution through crystallographic lattice reorientation

This crystal constitutive model is incorporated into a finite element formulation which has the following capabilities:

- three-dimensional grain geometries, where each grain is resolved with multiple finite elements
- weak form of the equations of equilibrium
- implicit time-integration of the constitutive equations for numerical stability
- scalable parallel implementation using Fortran 90 and interprocessor communication based on the Message Passing Interface (MPI) standard

Although the plastic deformation mechanisms that take place during cyclic loading are similar to those that take place during monotonic loading, the ef-

fect of cyclic hardening must be taken into account when simulating the response of polycrystals under fully-reversed cyclic loading due to the reversals in straining direction during a cycle. Under fully-reversed cyclic loading, the hysteresis loops will typically saturate at a macroscopic stress level that is much lower than the steady-state macroscopic stress under monotonic loading (pseudosaturation), assuming the macroscopic strain achieved under monotonic loading is equal to the cumulative macroscopic strain under cyclic loading. The conventional Voce hardening model [51] is unable to capture the macroscopic stress-strain response associated with reversals in straining direction under fully-reversed cyclic loading conditions. With a small modification to the conventional Voce hardening model, Turkmen et al. [52] were able to capture the pseudosaturation behavior observed in fully-reversed cyclic loading experiments conducted on SS304L stainless steel.

The shearing rate on the  $\alpha$ -slip system,  $\dot{\gamma}^\alpha$ , for a rate-dependent slip formulation is typically prescribed by a power-law form:

$$\dot{\gamma}^\alpha = \dot{\gamma}_0 \left( \frac{|\tau^\alpha|}{g^\alpha} \right)^{1/m} \text{sgn}(\tau^\alpha) \quad (2.1)$$

where  $\tau^\alpha$  is the resolved shear stress on the  $\alpha$ -slip system,  $g^\alpha$  is the slip system strength,  $\dot{\gamma}_0$  is a reference shearing rate and  $m$  is the rate sensitivity of slip. The resolved shear stress,  $\tau^\alpha$ , is the projection of the stress tensor,  $\boldsymbol{\tau}$ , on the  $\alpha$ -slip system [35, 36].

The cyclic slip system hardening model tracks the accumulated slip system shear strains on individual slip systems and the net crystal shearing rates within each crystal during a cycle [52]. Although the evolution of the dislocation structure in the material is not explicitly modeled in the cyclic hardening model, the net effect of the accumulation of dislocations on strain hardening is modeled implicitly through the evolution equations for the slip system strengths. The slip

system strengths for each crystal,  $g$ , evolve according to an isotropic hardening law:

$$\dot{g} = h_0 \left( \frac{g_s(\dot{\gamma}) - g}{g_s(\dot{\gamma}) - g_0} \right) f, \quad g_s(\dot{\gamma}) = g_{s0} \left( \frac{\dot{\gamma}}{\dot{\gamma}_{s0}} \right)^{m'} \quad (2.2)$$

where  $\dot{\gamma} = \sum_{\alpha} |\dot{\gamma}^{\alpha}|$  is the sum of the slip system shearing rates and  $h_0$ ,  $g_0$ ,  $g_{s0}$ ,  $m'$  are slip system hardening parameters. The quantity  $f$  in Equation (2.2) is dependent on the number of active slip systems,  $n_a$ , contributing to hardening within a crystal:

$$f = \sum_{\beta=0}^{n_a} |\dot{\gamma}^{\beta}| \quad (2.3)$$

The  $\alpha$ -slip system is considered to be contributing to hardening if the accumulated shear strain on the slip system since the last change in shearing direction,  $\Delta\gamma^{\alpha}$ , exceeds a critical value,  $\Delta\gamma_{\text{crit}}$ :

$$\Delta\gamma^{\alpha} = \int_{t_{+/-}}^t |\dot{\gamma}^{\alpha}| dt, \quad \Delta\gamma_{\text{crit}} = a \left( \frac{g}{g_s} \right)^b \quad (2.4)$$

where  $a$ ,  $b$  are cyclic hardening model parameters and  $t_{+/-}$  is the time since the last change in straining direction. The critical accumulated shear strain on a slip system,  $\Delta\gamma_{\text{crit}}$ , is implemented in the cyclic hardening model to introduce a hiatus in hardening, which accounts for the rearrangement of dislocations after a reversal in straining direction. Only after the process of dislocation pile-up is complete can additional hardening take place. Using this modification it is possible to capture the pseudosaturation behavior exhibited by the macroscopic stress-strain response with only a minimal modification to the evolution equations of the slip system strengths used for monotonic loading. The slip system and cyclic hardening parameters used in our simulations are similar to those used in Ref. [52], which were obtained from a fit to the macroscopic stress-strain response of SS304L stainless steel. The slip system and cyclic hardening parameters used for this set of simulations are shown in Table 2.1.

$h_0$ (MPa)	$g_0$ (MPa)	$g_{s0}$ (MPa)	$m$	$m'$	$\dot{\gamma}_0$ (s <sup>-1</sup> )	$\dot{\gamma}_{s0}$ (s <sup>-1</sup> )	$a$	$b$
257	100	275	0.02	0.0	1.0	$5 \times 10^{10}$	0.5	4.0

Table 2.1: Slip system and cyclic hardening model parameters for SS304L stainless steel [52].

Simulations were conducted by deforming virtual polycrystals under fully-reversed cyclic loading. Virtual polycrystals were instantiated with 1098 rhombic dodecahedra crystals (or grains), where each complete crystal was comprised of 48 10-node tetrahedra elements. There were also additional partial crystals which make up the surfaces of the finite element mesh, contributing to a total of 81000 finite elements in the mesh. Mesh convergence studies were previously conducted by Miller et al. [53] using virtual specimens with 1098, 2916 and 10976 complete dodecahedra crystals, which corresponds to 81000, 192000 and 648000 elements, respectively. Only small differences in the crystal stress distributions were observed between the finite element meshes of varying sizes. We have also conducted a comparison of different mesh sizes in Ref. [1], using virtual specimens with 1098 and 2916 crystals. Quantities averaged along a crystallographic fiber were found to exhibit similar trends across different mesh sizes. On this basis, the mesh with 1098 complete crystals was used in the current study to permit a larger number of simulations to be performed.

The simulation results can be compared to diffraction measurements of lattice strains by using crystallographic fibers as the basis of comparison. A crystallographic fiber, represented as  $\mathbf{c} \parallel \mathbf{s}$ , is the collection of all orientations with a particular crystal direction,  $\mathbf{c}$ , aligned with a particular specimen direction,  $\mathbf{s}$ . A crystallographic fiber consists of crystals with orientation,  $\mathbf{R}$ , that satisfy the following equation:

$$\mathbf{R}\mathbf{c} = \pm\mathbf{s} \quad (2.5)$$

All orientations associated with a crystallographic fiber differ only by a rotation about a common axis. A crystallographic fiber corresponds directly to a particular Bragg diffraction condition, where  $c$  is the crystal  $\{hkl\}$  plane normal and  $s$  is a particular specimen direction. A cutoff angle of  $5^\circ$  between  $c$  and  $s$  is used in the current study to determine whether a crystal orientation belongs to a particular crystallographic fiber. The simulation data does not distinguish between lower order and higher order  $\{hkl\}$  reflections ( $\{hkl\} = n\{hkl\}$ ). Therefore, only the lowest order  $\{hkl\}$  lattice planes are considered. Details of the post-processing methodology has previously been reported in Ref. [1].

Two crystallographic fibers are examined in particular: the  $\{100\} \parallel$  LD fiber and the  $\{111\} \parallel$  LD fiber. The  $\{100\} \parallel$  LD crystallographic fiber connects all crystals with orientations where the  $\{100\}$  crystal plane normal is aligned with the specimen loading direction (LD). The  $\{100\} \parallel$  LD and  $\{111\} \parallel$  LD fibers are chosen because they correspond to crystal orientations with extreme values of the directional strength-to-stiffness and these values vary significantly with  $r_E$ .

## 2.5 Simulation results

Three sets of simulations, designated as Sets 1, 2 and 3, were conducted using identical virtual polycrystals, except as noted below. For Set 1, the initial orientations of the crystals were randomly assigned from a uniform orientation distribution function (ODF). The cyclic slip system hardening model was active. For Set 2, the initial orientations of the crystals were randomly assigned from an ODF generated under plane strain compression to 70% strain. The ODF used in Set 2 is similar to the ODF shown in Ref. [54] and therefore will not be shown here. As with Set 1, the cyclic slip system hardening model was active for Set

2. For Set 3, the initial orientations of the crystals were the same as in Set 1. For this set, the cyclic slip system hardening model was inactive (no hardening). The different combinations of hardening and initial texture instantiated for each simulation set are shown in Table 2.2.

Set	Hardening	Initial ODF
1	Yes	Uniform
2	Yes	Plane strain compression
3	No	Uniform

Table 2.2: The different combinations of hardening and initial ODF for each set of simulations

Within each set of simulations, the only quantity that was varied was the single crystal elastic anisotropy ratio,  $r_E$ , which is defined as:

$$r_E = \frac{E_{\langle 111 \rangle}}{E_{\langle 100 \rangle}} \quad (2.6)$$

where  $E_{\langle 111 \rangle}$  and  $E_{\langle 100 \rangle}$  are the single crystal directional Young's modulus in the  $\langle 111 \rangle$  and  $\langle 100 \rangle$  crystal directions, respectively. Two cases were considered:  $r_E = 1.0$  and  $r_E = 3.2$ . For  $r_E = 3.2$ , representative values of the single crystal elastic moduli ( $C_{11}$ ,  $C_{12}$  and  $C_{44}$ ) for stainless steel were used [55]. For  $r_E = 1.0$ , the moduli were adjusted to give isotropic single crystal behavior while leaving the macroscopic Young's modulus the same as that of stainless steel. The single crystal elastic moduli corresponding to these two values of  $r_E$  are shown in Table 2.3. The method of varying the single crystal elastic constants is described in detail in Refs. [1, 3].

Fully-reversed uniaxial tension-compression loading conditions were applied to the virtual polycrystals. A constant velocity was applied on the positive  $Z$  surface of the finite element mesh, while the  $Z = 0$  face of the mesh was constrained in the  $Z$ -direction. The two positive  $X$  and  $Y$  surfaces of the mesh were

$r_E$	$C_{11}$ (GPa)	$C_{12}$ (GPa)	$C_{44}$ (GPa)
1.0	266.433	106.784	79.826
3.2	204.600	137.700	126.200

Table 2.3: Single crystal elastic moduli corresponding to  $r_E = 1.0$  and  $r_E = 3.2$ . Representative values of the single crystal elastic moduli for stainless steel ( $r_E = 3.2$ ) were obtained from Ref. [55].

traction-free, while the  $X = 0$  and  $Y = 0$  surfaces had symmetry boundary conditions imposed. The simulations were conducted under fully reversed cyclic loading ( $R = -1$ ) in strain control at a constant strain rate of  $0.001 \text{ s}^{-1}$  for 20 complete cycles. The virtual specimen was cycled between fixed macroscopic strain limits of  $\pm 1\%$  strain.

### 2.5.1 Macroscopic stress-strain response

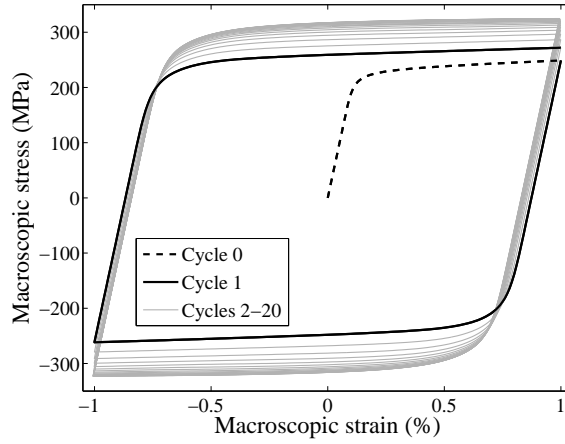
The macroscopic value of the axial stress was computed for the 20 loading cycles from the average normal traction over the loaded surface of the polycrystal. For Set 1, the resulting macroscopic stress for  $r_E = 3.2$  is plotted in Figure 2.2(a) as a function of the macroscopic strain, which is computed on the basis of the overall axial dimension changes of the polycrystal. Cycles 0 and 1 are highlighted in Figure 2.2(a). Cycle 0 corresponds to monotonic loading in tension up to 1% macroscopic strain. The outermost loop corresponds to Cycle 20 in the deformation history. The loops grow in size with increasing cycles due to continued strain hardening. Since the polycrystals were cycled between fixed strain limits, a higher macroscopic stress level was required to achieve the same macroscopic strain limits on each cycle due to cyclic hardening. However, the cycle-by-cycle change in macroscopic stress at 1% macroscopic strain decreases with increasing cycles due to pseudosaturation of the slip system strength that

is built into the model for the cyclic hardening behavior. With the exception of the elastic-plastic transition regime (the knee of the macroscopic stress-strain curve), the macroscopic stress-strain curves for the two values of  $r_E$  in Set 1 are very similar. The macroscopic stresses for Set 2 are slightly higher overall than those of Set 1. This is because the plane strain compression texture used in the Set 2 simulations results in a higher average Taylor factor than the uniform ODF used for Set 1. Aside from the slight difference in the macroscopic stress level, the stress-strain hysteresis loops between Sets 1 and 2 are very similar and, consequently are not shown.

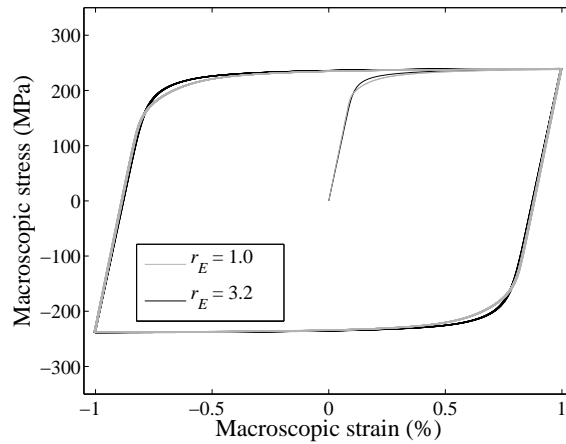
Figure 2.2(b) shows the macroscopic stress-strain curves for the two simulations of Set 3. In the absence of cyclic hardening, the slip system strength remains constant over the simulation and the macroscopic stress does not increase with cycles. Small differences between the macroscopic stress-strain curves are observed in the elastic-plastic transition as  $r_E$  is varied. The slopes of the macroscopic stress-strain curves in the elastic loading and unloading portions of each cycle demonstrate that the single crystal elastic moduli were changed such that the macroscopic Young's modulus is unchanged.

## 2.5.2 Lattice strain response

The lattice strain,  $\varepsilon_{\{hkl\}}$ , for the  $\{hkl\}$  || LD crystallographic fiber is computed as follows: for each element in the mesh whose orientation belongs to the  $\{hkl\}$  || LD fiber to within a given tolerance, its full elastic strain tensor,  $\epsilon$ , is projected in the LD direction. The lattice strain value,  $\epsilon_{\{hkl\}}$ , is then obtained by averaging the projected elastic strain tensor value among all  $n$  crystals belonging to the  $\{hkl\}$  ||



(a) Set 1 for  $r_E = 3.2$



(b) Set 3 for  $r_E = 1.0$  and  $r_E = 3.2$

Figure 2.2: Macroscopic true stress-strain curves for 20 complete cycles for simulation Sets 1 and 3.

LD fiber:

$$\varepsilon_{\{hkl\}} = \left( \sum_{i=1}^n \mathbf{s}_i \cdot \boldsymbol{\epsilon}_i \cdot \mathbf{s}_i^T \right) / n \quad (2.7)$$

The average lattice strains associated with the  $\{100\} \parallel$  LD and  $\{111\} \parallel$  LD crystallographic fibers for Sets 1 and 3 are plotted in Figures 2.3 and 2.4 with lattice strain on the abscissa and the macroscopic stress on the ordinate to facilitate comparison with the experimental data shown in Figure 2.1. As with the macroscopic stress-strain hysteresis loops, there is little difference between the results

for Sets 1 and 2 (uniform versus plane strain compression textures), so only Set 1 is shown.

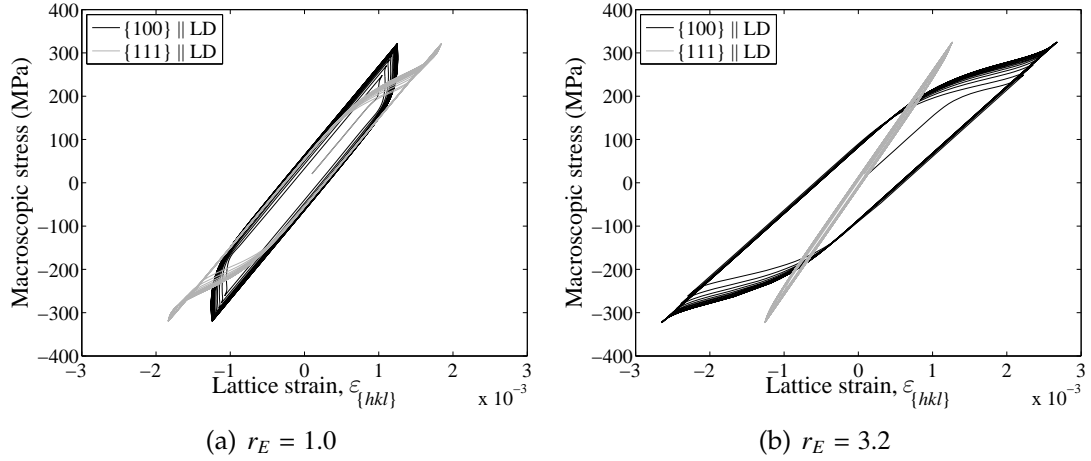


Figure 2.3: Lattice strain,  $\varepsilon_{\{hkl\}}$ , versus macroscopic true stress for the simulations of Set 1. The lattice strains are averaged among crystals belonging to the  $\{100\} \parallel \text{LD}$  and  $\{111\} \parallel \text{LD}$  crystallographic fibers, where LD corresponds to the  $[001]$  specimen loading direction.

Examining first the lattice strains for Set 1, it is evident that the lattice strains for  $r_E = 1.0$ , where the crystals are elastically isotropic, exhibit very different behaviors compared to the lattice strains for  $r_E = 3.2$ , where the crystals have high elastic anisotropy. For  $r_E = 1.0$ , shown in Figure 2.3(a), both the  $\{100\} \parallel \text{LD}$  and  $\{111\} \parallel \text{LD}$  lattice strains exhibit hysteresis over the course of a cycle. For  $r_E = 3.2$ , shown in Figure 2.3(b), the  $\{100\} \parallel \text{LD}$  lattice strains exhibit significant hysteresis, but the  $\{111\} \parallel \text{LD}$  crystals exhibit a linear relation between the lattice strains and macroscopic stress over the course of a cycle. The lattice strain response without strain hardening (Set 3) is shown in Figure 2.4. The lattice strain hysteresis loops do not increase in size with increasing cycles due to the absence of strain hardening. Nevertheless, the lattice strain hysteresis loops for Set 3 exhibit similar trends as the simulations in Sets 1 and 2.

The difference in the single crystal elastic anisotropy can be observed from

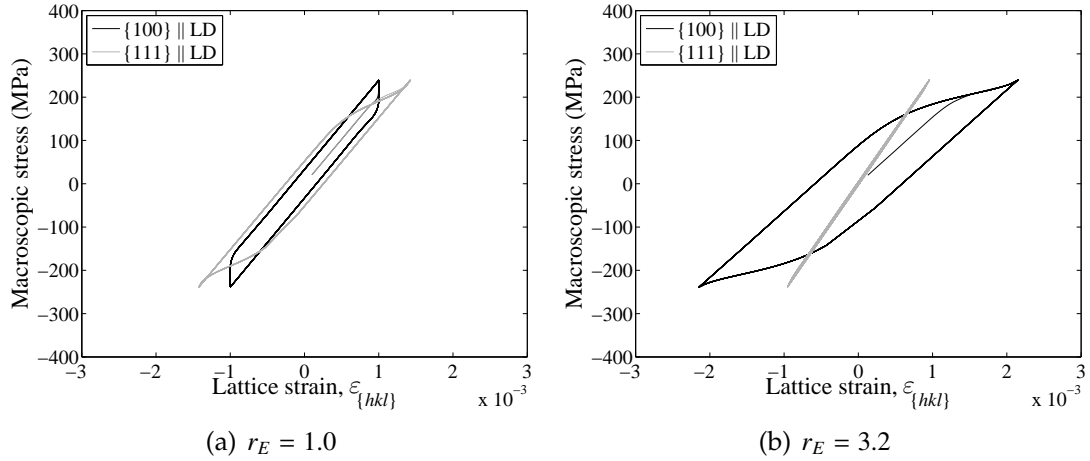


Figure 2.4: Lattice strain,  $\varepsilon_{\{hkl\}}$ , versus macroscopic true stress for the simulations of Set 3. The lattice strains are averaged among crystals belonging to the  $\{100\} \parallel \text{LD}$  and  $\{111\} \parallel \text{LD}$  crystallographic fibers, where LD corresponds to the  $[001]$  specimen loading direction.

the slopes of the elastic loading and unloading portions of macroscopic stress versus lattice strain curves. Note that for  $r_E = 1.0$ , shown in Figures 2.3(a) and 2.4(a), the  $\{100\} \parallel \text{LD}$  and  $\{111\} \parallel \text{LD}$  lattice strains have the same slope in the elastic loading and unloading portions of the cycle, which is consistent with the isotropic nature of the crystals. For  $r_E = 3.2$  however, where the lattice strains are shown in Figure 2.3(b) and 2.4(b), the lattice strains in the elastic loading and unloading portion of the cycle exhibit different slopes, illustrating the influence of elastic anisotropy on the  $\{100\} \parallel \text{LD}$  and  $\{111\} \parallel \text{LD}$  crystals.

We can compare the results for  $r_E = 3.2$  with the experimental data. The computed lattice strains shown in Figure 2.3(b) are qualitatively consistent with the measured lattice strains shown in Figure 2.1. The near-linear response of the  $\{111\} \parallel \text{LD}$  lattice strains with macroscopic stress, with no evidence of hysteresis loops, observed in the measurements is predicted in the simulations. Further, the computed  $\{200\} \parallel \text{LD}$  lattice strains exhibit significant hysteresis, which also agrees qualitatively with the measured  $\{200\} \parallel \text{LD}$  lattice strains. However, the

computed  $\{200\} \parallel$  LD lattice strains exhibit a gradual downward inflection in the elastic-plastic transition regime which is not evident in the measured  $\{200\} \parallel$  LD lattice strains. This discrepancy between the computed and measured  $\{200\} \parallel$  LD lattice strains has also been observed by Lorentzen et al. [46] when using a self-consistent elastoplastic model. Lorentzen et al. [46] attributed this to the lack of experimental data in the region just past zero macroscopic stress, since diffraction measurements were conducted at only 24 points during a cycle. The lattice strains measurements by Korsunsky et al. [47] shown in Figure 2.1(b) were conducted at eight points during a cycle. Given the rapid changes occurring during the elastic-plastic transition regime, the frequency of measurements is not sufficient to capture details of the elastic-plastic transition and we do not expect a close match between the measured and computed lattice strains in this regime.

### 2.5.3 Slip system activity

Although the  $\{111\} \parallel$  LD lattice strains for  $r_E = 3.2$  exhibit linear behavior between the elastic *lattice* strain and the *macroscopic* stress over the course of a cycle, this is not indicative of these crystals deforming within their elastic regime. To demonstrate this, we examine the plastic deformation rate magnitude,  $D_{\{hkl\}}^P$ , cycle by cycle for the crystals belonging to both the  $\{100\} \parallel$  LD and  $\{111\} \parallel$  LD fibers. The plastic deformation rate vector,  $\hat{\mathbf{D}}^P$ , is a five-dimensional deviatoric vector computed at the centroid of each element in the mesh. The second order tensor form of  $\hat{\mathbf{D}}^P$  for a single element in the mesh is computed as:

$$\hat{\mathbf{D}}^P = \sum_{\alpha} \dot{\gamma}^{\alpha} \text{sym}(\hat{\mathbf{s}}^{\alpha} \otimes \hat{\mathbf{m}}^{\alpha}) \quad (2.8)$$

where  $\dot{\gamma}^\alpha$  is the slip system shearing rate,  $\hat{s}^\alpha$  is the slip direction, and  $\hat{m}^\alpha$  is the slip plane normal for each  $\alpha$ -slip system. The vector norm for the deviatoric vector  $\hat{\mathbf{D}}^P$  is computed and averaged among all crystals belonging to the  $\{hkl\}$  || LD fiber to obtain the plastic deformation rate magnitude,  $D_{\{hkl\}}^P$ . For each cycle, we track  $D_{\{hkl\}}^P$  starting at a macroscopic stress of -100 MPa and continuing until a macroscopic strain of 1% is achieved, as indicated in Figure 2.5. The results for Sets 1 and 3 are presented in Figures 2.6 and 2.7, respectively. Again, Set 2 is similar to Set 1 and is not shown. A steep increase in  $D_{\{hkl\}}^P$  at a particular macroscopic stress indicates that on average, the crystals associated with the  $\{hkl\}$  || LD fiber have yielded and plastic flow is occurring among those crystals. The results indicate that the crystals belonging to both the  $\{100\}$  || LD and  $\{111\}$  || LD fibers experience plastic deformation over each cycle, even though there is no hysteresis associated with the  $\{111\}$  || LD lattice strains, as shown in Figures 2.3(b) and 2.4(b). Only a constant  $D_{\{hkl\}}^P$  value of zero over the course of a cycle for all macroscopic stress values would indicate that the crystals are remaining fully elastic.

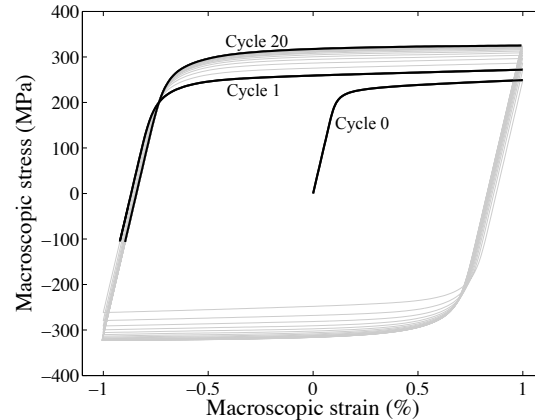


Figure 2.5: The solid black lines on the stress-strain curve correspond to the portions of the stress-strain curve where  $D_{\{hkl\}}^P$  is plotted on Cycles 0, 1 and 20 for Set 1.

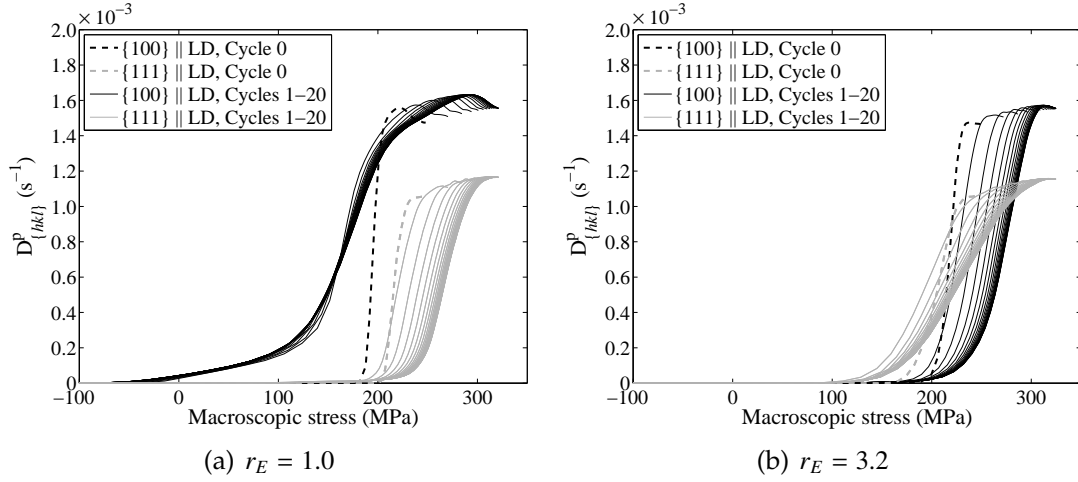


Figure 2.6: Plastic deformation rate magnitude,  $D_{\{hkl\}}^p$ , versus macroscopic true stress for crystals belonging to the  $\{100\} \parallel \text{LD}$  and  $\{111\} \parallel \text{LD}$  crystallographic fibers for the simulations of Set 1. The LD direction corresponds to the  $[001]$  specimen loading direction. The plastic deformation rate magnitude,  $D_{\{hkl\}}^p$ , is plotted starting at a macroscopic stress of  $-100$  MPa until a macroscopic strain of  $1\%$  is achieved, which is shown for Cycles 0, 1 and 20 in Figure 2.5.

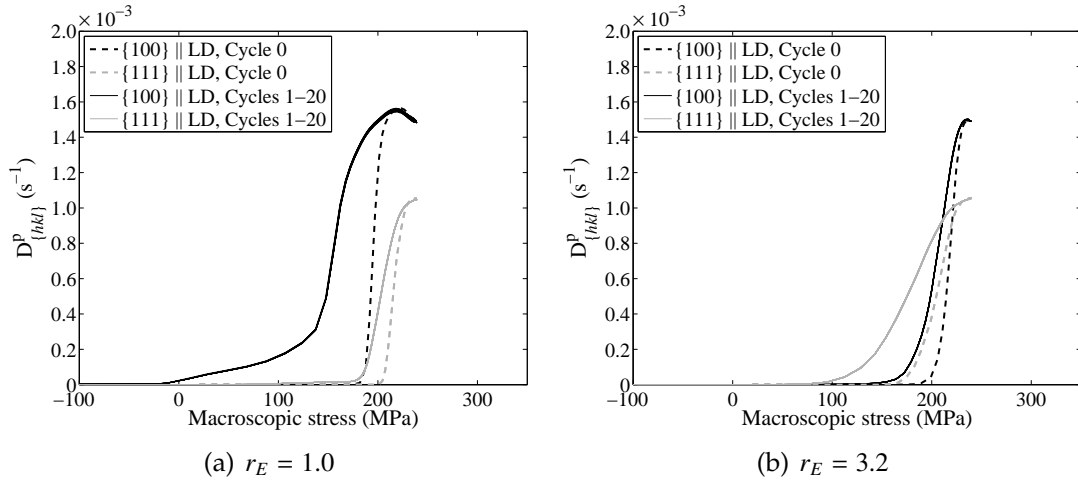


Figure 2.7: Plastic deformation rate magnitude,  $D_{\{hkl\}}^p$ , versus macroscopic true stress for crystals belonging to the  $\{100\} \parallel \text{LD}$  and  $\{111\} \parallel \text{LD}$  crystallographic fibers for the simulations of Set 3. The LD direction corresponds to the  $[001]$  specimen loading direction.

Figures 2.6(a) and 2.7(a) demonstrate that for  $r_E = 1.0$ , even though the crystals are elastically isotropic, the  $\{100\} \parallel \text{LD}$  and  $\{111\} \parallel \text{LD}$  crystals yield on average at different macroscopic stress levels. The difference in the macroscopic stress at which yielding occurs on average in these crystals, therefore, can be attributed to the plastic anisotropy (orientation dependent yield strength). Since the  $\{100\} \parallel \text{LD}$  crystals yield on average at a lower macroscopic stress compared to the  $\{111\} \parallel \text{LD}$  crystals, it implies that for  $r_E = 1.0$ , the  $\{100\} \parallel \text{LD}$  crystals on average are more favorably oriented for yielding than the  $\{111\} \parallel \text{LD}$  crystals. When  $r_E$  is increased to  $r_E = 3.2$ , the  $\{100\} \parallel \text{LD}$  crystals now yield at a higher macroscopic stress on average compared to the  $\{111\} \parallel \text{LD}$  crystals. Therefore, the value of  $r_E$  influences the macroscopic stress at which yielding begins for crystals associated with different fibers. This implies that the progression of yielding among these crystals is influenced by both the elastic and plastic properties, which will be examined in more detail in Section 2.6.1.

It is also observed from Figures 2.6 and 2.7 that the macroscopic stress at which yielding begins is lower on Cycle 1 compared to Cycle 0. This phenomena arises due to yield asymmetry, which is a Bauschinger-type phenomena first observed by Czyzak et al. [56] and Hutchinson et al. [57]. Barton et al. [58], using an elastoplastic crystal-based finite element model similar to the one used in our current study, demonstrated that a polycrystal yields at a lower macroscopic stress in compression after it has been yielded in tension due to residual crystal stresses that are present even in the macroscopically unloaded state. After Cycle 1 however, the macroscopic stress at which yielding begins increases with increasing cycles due to cyclic hardening. Yield asymmetry can still be observed even when the cyclic slip hardening model is inactive for Set 3, as seen in Figure 2.7, although the macroscopic stress at which yielding begins does not

increase with cycles after Cycle 1.

## 2.6 Influences of directional strength-to-stiffness and SCYS topology on the cyclic response

### 2.6.1 Directional strength-to-stiffness

To explain why the lattice strain hysteresis loops differ qualitatively with  $r_E$ , we consider the orientation dependence of both the elastic and plastic properties of the crystals. Although there exist minor differences stemming from the initial texture and from the absence or presence of hardening, a consistent trend emerged from the three sets of simulations. The  $\{100\}$  || LD crystals yield on average at a lower macroscopic stress compared to the  $\{111\}$  || LD crystals when  $r_E = 1.0$ , as shown in Figures 2.6(a) and 2.7(a). However, for  $r_E = 3.2$ , the reverse situation occurs, where the  $\{111\}$  || LD crystals yield on average at a lower macroscopic stress compared to the  $\{100\}$  || LD crystals, which is evident from Figures 2.6(b) and 2.7(b). Thus, the macroscopic stress at which yielding begins for anisotropic crystals is influenced by the combination of the elastic and plastic anisotropy of the crystals, which can be quantified using the directional strength-to-stiffness ratio [1]. The directional strength-to-stiffness ratio for a single crystal under uniaxial tension applied in the direction,  $\mathbf{d}$ , relative to the crystal lattice,  $r_s^{\text{crys}}$ , is defined as:

$$r_s^{\text{crys}} = \frac{1}{m_d \cdot E_d} \quad (2.9)$$

where  $m_d$  is the Schmid factor [40] and  $E_d$  is the single crystal directional Young's modulus [34] for the crystal direction  $\mathbf{d}$ . The Schmid factor,  $m_d$ , quantifies the

relative ease for single slip to occur in a single crystal with a uniaxial stress applied in the crystal direction  $\mathbf{d}$ . Since a high value of  $m_d$  indicates that a particular crystal direction is more favorably oriented for slip, the directional strength is defined as the inverse of  $m_d$  in Equation (2.9). The directional stiffness is defined as  $E_d$  in the direction  $\mathbf{d}$ . The orientation dependence of the single crystal directional strength-to-stiffness,  $r_S^{\text{crys}}$ , is shown within the basic cubic orientation triangle in Figure 2.8.

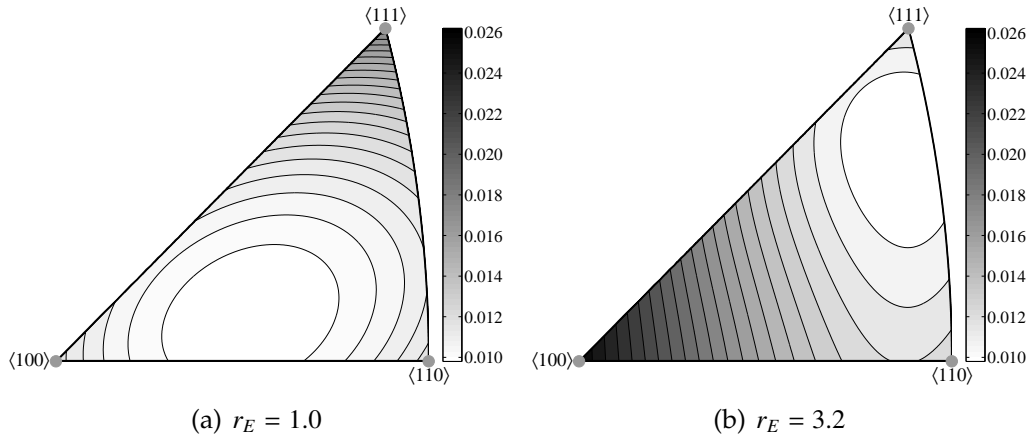


Figure 2.8: Single crystal directional strength-to-stiffness ratio shown within the basic orientation triangle for  $r_E = 1.0$  and  $r_E = 3.2$ . The figures have the same grayscale bar for comparison purposes.

We have previously demonstrated that for a polycrystalline aggregate under uniaxial tension, crystals with high directional strength-to-stiffness ratio will yield on average at a relatively higher macroscopic stress compared to crystals with low directional strength-to-stiffness ratio [1]. Figure 2.8(a) shows that for  $r_E = 1.0$ , the  $\langle 111 \rangle$  direction has the higher strength-to-stiffness ratio relative to the  $\langle 100 \rangle$  direction. Conversely, Figure 2.8(b) shows that for  $r_E = 3.2$ , the  $\langle 100 \rangle$  direction instead has the higher strength-to-stiffness relative to the  $\langle 111 \rangle$  direction. As  $r_E$  is increased, the  $\langle 100 \rangle$  strength-to-stiffness increases while the

$\langle 111 \rangle$  strength-to-stiffness decreases. The same trend exists for average strength-to-stiffness ratios taken over all the orientations lying along a crystallographic fiber, as reported in [1]. Table 2.4 gives the strength-to-stiffness values for the  $\{100\} \parallel \text{LD}$  and  $\{111\} \parallel \text{LD}$  fibers along with the corresponding single crystal values.

$r_E$	$\langle 100 \rangle$	$\langle 111 \rangle$	$\{100\} \parallel \text{LD}$	$\{111\} \parallel \text{LD}$
1.0	0.0119	0.0179	0.0113	0.0236
3.2	0.0261	0.0123	0.0213	0.0177

Table 2.4: Directional strength-to-stiffness values for selected single crystal directions and averages over crystallographic fibers.

Comparing Figure 2.6 to Figure 2.8, the macroscopic stress at which the  $\{100\} \parallel \text{LD}$  crystals begin yielding increases as the  $\langle 100 \rangle$  strength-to-stiffness increases. Conversely, the macroscopic stress at which the  $\{111\} \parallel \text{LD}$  crystals begin yielding decreases as the  $\langle 111 \rangle$  strength-to-stiffness decreases. Therefore, the macroscopic stress at which yielding begins on average for crystals associated with a crystallographic fiber correlates well with the directional strength-to-stiffness ratio at low and high values of  $r_E$ . For crystals with intermediate values of  $r_E$ , particularly in the range of  $r_E = 1.5 - 2.0$ , the  $\langle 100 \rangle$  and  $\langle 111 \rangle$  crystals have similar directional strength-to-stiffness values [1]. At intermediate values of  $r_E$ , the interaction with neighboring crystals together with the directional strength-to-stiffness ratio are important influences on the stress distribution of the crystals associated with a fiber.

We now focus on the results from the simulations of Set 1 to examine the role of the directional strength-to-stiffness in determining the lattice strain and plastic deformation rate response for crystals associated with the  $\{100\} \parallel \text{LD}$  and  $\{111\} \parallel \text{LD}$  fibers. For both values of  $r_E$ , the crystals that yield on average at a relatively higher macroscopic stress (Figure 2.6) also exhibit a downward

inflection in lattice strain (Figure 2.3). For  $r_E = 1.0$ , the  $\{111\} \parallel$  LD crystals yield at a higher macroscopic stress which is accompanied by a downward inflection in the lattice strain. For  $r_E = 3.2$ , the  $\{100\} \parallel$  LD crystals instead yield at a higher macroscopic stress which is also accompanied by a downward inflection in the lattice strain. The downward inflection of the lattice strains in the elastic-plastic transition regime is due to redistribution of additional load between crystals that have yielded and crystals that have not yielded [1, 29], where proportionally more elastic straining can occur in crystals that have not yielded. As  $r_E$  is increased from the isotropic case ( $r_E = 1.0$ ) to the highly anisotropic case ( $r_E = 3.2$ ), the behavior of the  $\{111\} \parallel$  LD lattice strains changes from a downward inflection to near-linear behavior with increasing macroscopic stress. Conversely, the  $\{100\} \parallel$  LD lattice strains exhibit an upward inflection for  $r_E = 1.0$  which becomes a downward inflection for  $r_E = 3.2$ . This is a consequence of the change in the  $\langle 100 \rangle$  directional strength-to-stiffness from low to high relative to that of other orientations which changes the macroscopic stress at which yielding begins for the  $\{100\} \parallel$  LD crystals.

## 2.6.2 Vertices of the single crystal yield surface

Plastic deformation via slip initiates when the crystal stress reaches the SCYS. With increasing plastic strain, the crystal stress traverses the SCYS until it reaches a vertex [38, 58]. The crystal stress moves toward a vertex to accommodate a deviatoric strain state that is compatible with the motion of the polycrystal. The SCYS defined by the 12  $\{111\}\langle 110 \rangle$  slip systems in fcc crystals has 56 vertices (28 positive vertices). The vertices can be grouped into five unique vertex families due to crystal symmetries, where the vertex stresses within a vertex family are indistinguishable from each other [39]. The relative magnitudes

of the vertex stresses for the five families are listed in Table 2.5. An important aspect of the behavior of fcc polycrystals is that under monotonic tensile loading, the crystal stresses associated with a particular crystallographic fiber tend to align more closely with certain vertex families than others in fully-developed plasticity [2]. Here, we examine the lattice strains with respect to the five unique vertex families of the SCYS for fully-reversed cyclic loading.

Vertex family number	Relative magnitude of $\sigma'_v$
V1	1.00
V2	1.50
V3	1.73
V4	1.33
V5	1.23

Table 2.5: Relative magnitude of the deviatoric vertex stress,  $\sigma'_v$ , for the five vertex families associated with the fcc SCYS [2].

For Set 1, the  $\{100\} \parallel \text{LD}$  and  $\{111\} \parallel \text{LD}$  lattice strains are plotted as a function of the macroscopic strain for  $r_E = 1.0$  and  $r_E = 3.2$  in Figure 2.9. First, note that the initial slopes of the curves during the elastic loading and unloading portions of the straining cycle reflect the elastic anisotropy. For  $r_E = 1.0$ , the  $\{100\} \parallel \text{LD}$  and  $\{111\} \parallel \text{LD}$  lattice strains have the same slopes as each other during both the elastic loading and unloading portions of the cycle. For  $r_E = 3.2$ , however, the lattice strains for these two fibers exhibit different slopes at the start of the elastic loading and unloading portions of each cycle, as expected from the single crystal elastic moduli. After the elastic-plastic transition regime, but before unloading, the straining of the sample is accommodated predominantly by plastic straining and the lattice strains approach approximately steady values consistent with fully-developed plasticity. (The lattice strains do change slightly between the elastic-plastic transition and unloading, but the changes are small in comparison to the changes in the elastic regime.) For  $r_E = 1.0$ , shown in Fig-

ure 2.9(a), the steady value of the  $\{111\} \parallel \text{LD}$  lattice strains is larger than the steady value of the  $\{100\} \parallel \text{LD}$  lattice strains. In contrast, for  $r_E = 3.2$  the reverse is true, as is evident from Figure 2.9(b).

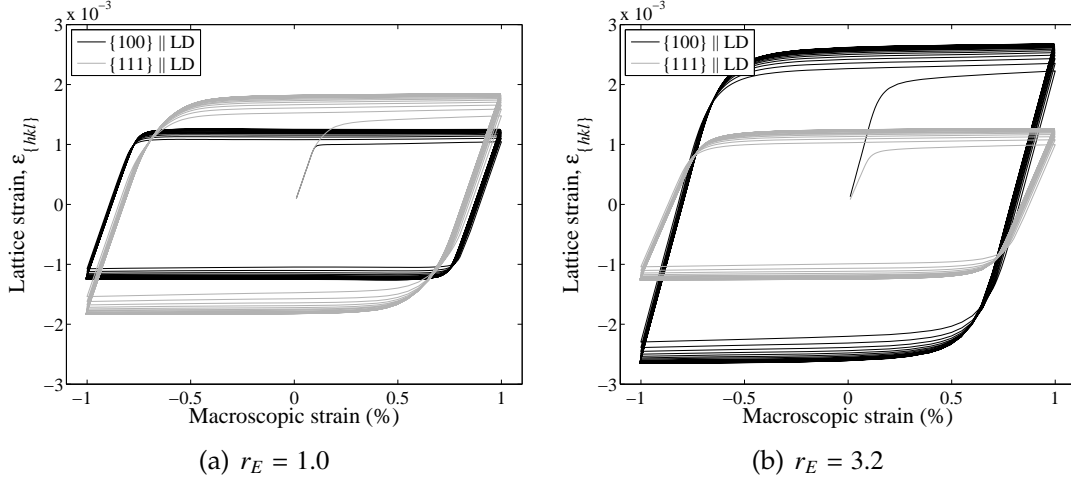


Figure 2.9: Lattice strain,  $\varepsilon_{\{hkl\}}$ , versus macroscopic true strain associated with the the  $\{100\} \parallel \text{LD}$  and  $\{111\} \parallel \text{LD}$  fibers for the simulations of Set 1, where LD is the specimen loading direction.

For the elastically isotropic case of  $r_E = 1.0$ , the relative differences in the lattice strains in fully-developed plasticity are a consequence of the SCYS. The crystal stresses are on average different for the two fibers. For the elastically anisotropic case of  $r_E = 3.2$ , the relative differences in lattice strains are a consequence of both the SCYS and the elastic anisotropy. The average moduli, as well as the crystal stresses, are on average different for the two fibers.

Using an analysis similar to that conducted by Ritz et al. [2], we can show that the average stresses for the two fibers reflect the constraint imposed by the SCYS. The angle of coaxiality,  $\phi_c^v$ , between the deviatoric form of the crystal stress,  $\sigma'_c$ , and the deviatoric form of the nearest vertex stress,  $\sigma'_v$ , is computed for each element associated with a crystallographic fiber as follows:

$$\phi_c^v = \cos^{-1} \left( \frac{\sigma'_c \cdot \sigma'_v}{\|\sigma'_c\| \|\sigma'_v\|} \right) \quad (2.10)$$

A coaxiality angle of zero indicates that the crystal stress is completely aligned with its preferred vertex stress. The  $\phi_c^v$  distributions corresponding to several crystallographic fibers are shown at 1% macroscopic strain on Cycle 1 for  $r_E = 1.0$  and  $r_E = 3.2$  in Figures 2.10(a) and 2.10(b), respectively. The distributions are very insensitive to the elastic anisotropy. The  $\phi_c^v$  distributions on Cycle 20 are very similar to the  $\phi_c^v$  distributions on Cycle 1, even with the stress increasing on successive cycles due to strain hardening. At both Cycle 1 and 20, the crystal stresses for the various fibers associate strongly with particular vertex families. The slip system strengths within a crystal evolve according to Equation (2.2), resulting in an increase in the size of the SCYS without a change in its shape. The preferred vertices for each fiber thus remain unchanged with increasing numbers of cycles. This observation for fully-reversed cyclic loading is consistent with previous results discussed by Ritz et al. for fcc polycrystals under monotonic tensile loading [2].

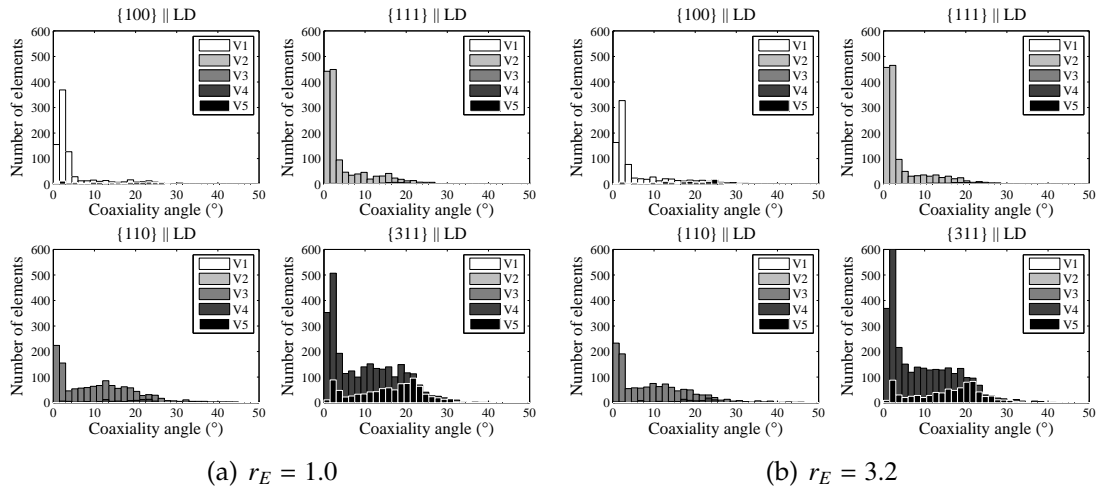


Figure 2.10: Coaxiality angle,  $\phi_c^v$ , between the crystal stress and the nearest vertex stress for several crystallographic fibers at 1% macroscopic strain on Cycle 1. V1-V5 correspond to the five unique vertex families.

We now return to the lattice strains presented in Figure 2.9. At 1% macro-

scopic strain on a particular cycle, the crystal stress distributions over the polycrystal are approximately the same for  $r_E = 1.0$  and  $r_E = 3.2$ , but the magnitudes of lattice strains differ. This is expected from the differences in the elastic moduli for the two levels of elastic anisotropy. For  $r_E = 1.0$ , the difference between the  $\{100\} \parallel \text{LD}$  and  $\{111\} \parallel \text{LD}$  lattice strains in Figure 2.9(a) is due solely to the difference between the magnitudes of the V1 and V2 vertex stresses. From Figure 2.10, the preferred vertex family of the  $\{100\} \parallel \text{LD}$  crystals is the V1 vertex family and the preferred vertex family of the  $\{111\} \parallel \text{LD}$  crystals is the V2 vertex family. Consequently, for  $r_E = 1.0$ , the  $\{111\} \parallel \text{LD}$  steady lattice strains are larger than the  $\{100\} \parallel \text{LD}$  steady lattice strains since the magnitude of the V2 vertex stress is larger than the V1 vertex stress, which is demonstrated in Table 2.5. The difference in the lattice strains for  $r_E = 3.2$ , however, which are shown in Figure 2.9(b), is due to a combination of the single crystal elastic moduli and the difference between the V1 and V2 vertex stresses.

The coaxiality angle distributions indicate that the crystal stresses near the end of each loading cycle tend to align with the same sets of SCYS vertices irrespective of the elastic anisotropy and the cycle number. This trend holds true for simulation Sets 1, 2 and 3. However, variability does exist in the stress magnitude among the crystals associated with a particular fiber. This variability is a function both of the elastic anisotropy and the cycle number. To examine the stress variability, crystal stress frequency distributions are constructed for the crystals associated with a particular fiber. Specifically, for all the finite elements with lattice orientation lying along a designated fiber, we construct the frequency distribution of the magnitude of the crystal deviatoric stress vector normalized with respect magnitude of the macroscopic deviatoric stress. The evolution of these frequency distributions over the course of the loading cycle,

as indicated on Figure 2.11, is examined for Cycles 0, 1 and 20, for both values of  $r_E$  and for several crystallographic fibers.

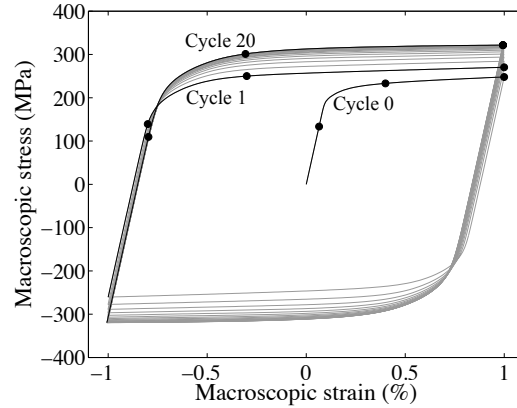


Figure 2.11: Points along the macroscopic stress-strain curve on Cycles 0, 1 and 20 for which the distributions of the normalized deviatoric stress magnitudes are plotted in Figures 2.12–2.14.

The normalized stress distributions on Cycle 0 for  $r_E = 1.0$  and  $r_E = 3.2$  are shown in Figures 2.12(a) and 2.12(b), respectively, at the three points along the macroscopic stress-strain curve. These correspond to 0.065%, 0.4% and 1% macroscopic strain. In the elastic regime at 0.065% macroscopic strain, the normalized stress distributions differ significantly between  $r_E = 1.0$  and  $r_E = 3.2$ , reflecting the difference in elastic anisotropy of the crystals. As the deformation proceeds, the crystal stresses evolve through the elastic-plastic transition toward similar distributions at 1% macroscopic strain. It is observed from the macroscopic stress-strain curve in Figure 2.11 that at 1% macroscopic strain on Cycle 0, the material is continuing to strain harden, which may cause differences in the stress distributions between  $r_E = 1.0$  and  $r_E = 3.2$  because the crystals may not be experiencing fully-developed plastic flow at this stage of the deformation.

The normalized stress distributions on Cycle 1 are plotted in Figure 2.13 at -0.8%, -0.3% and 1% macroscopic strain, as indicated in Figure 2.11. On this cy-

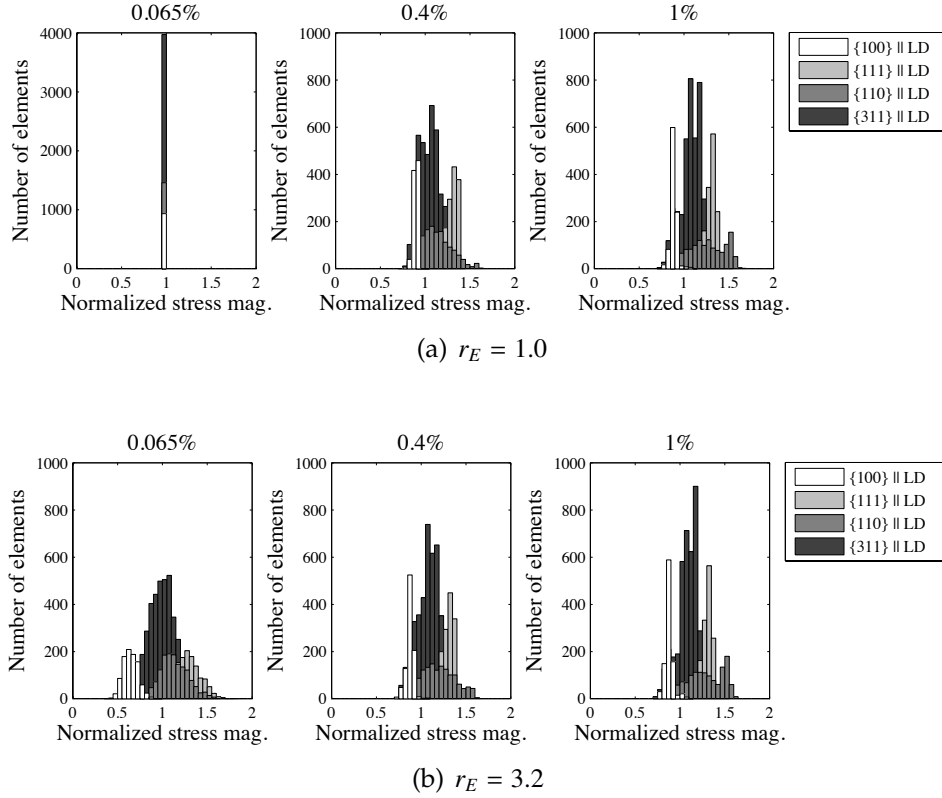
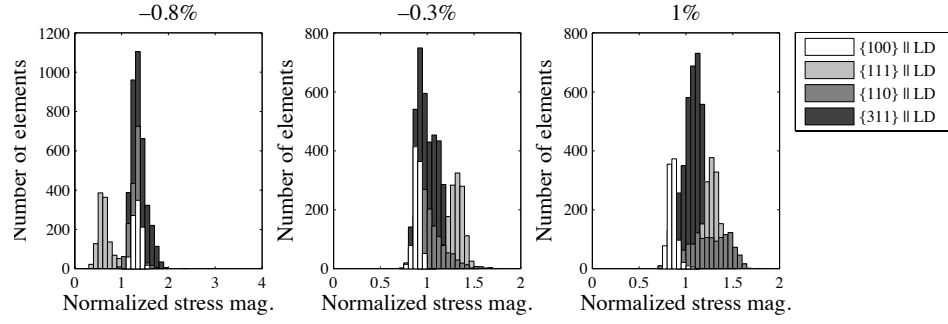
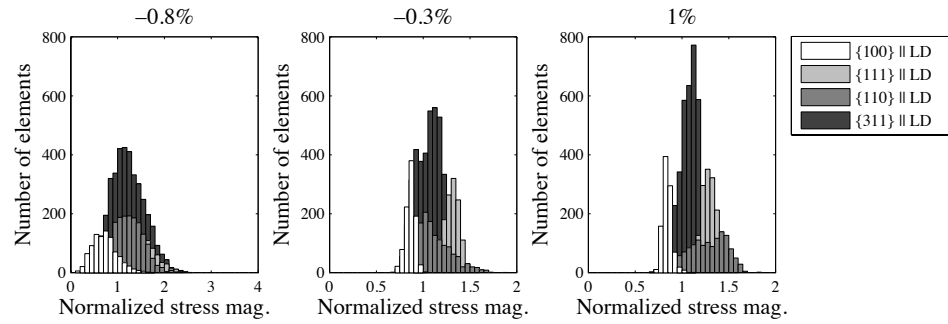


Figure 2.12: Normalized deviatoric stress magnitudes for  $r_E = 1.0$  and  $r_E = 3.2$  on Cycle 0 at 0.065%, 0.4% and 1% macroscopic strain.

cle, as well as all succeeding cycles, the normalized stress distributions at  $-0.8\%$  macroscopic strain (prior to the onset of the elastic-plastic transition) are not homogenous, even for isotropic elasticity ( $r_E = 1.0$ ). This is due to the presence of residual stresses induced by plastic straining on Cycle 0. The distributions at this stage of the deformation differ between  $r_E = 1.0$  and  $r_E = 3.2$  due to the influence of the directional strength-to-stiffness on load sharing among crystals, as discussed previously in Section 2.6.1. The presence of residual stresses as well as the directional strength-to-stiffness ratio influences the crystal stresses in the elastic-plastic transition as the deformation proceeds. With increasing macroscopic strain, the normalized stress distributions for both  $r_E = 1.0$  and  $r_E = 3.2$  evolve toward a similar pattern in fully-developed plasticity, as demonstrated



(a)  $r_E = 1.0$

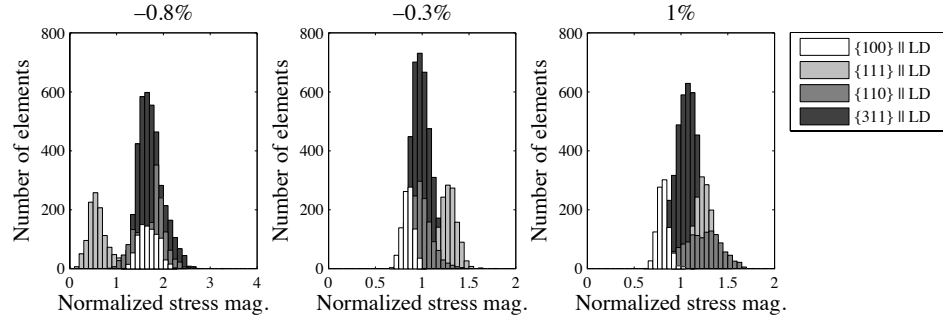


(b)  $r_E = 3.2$

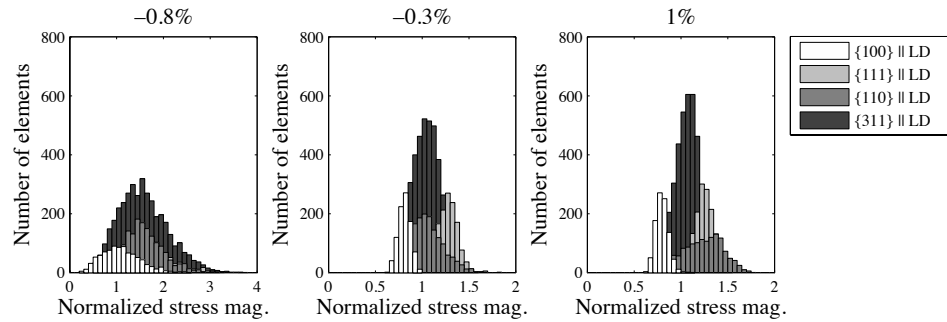
Figure 2.13: Normalized deviatoric stress magnitudes for  $r_E = 1.0$  and  $r_E = 3.2$  on Cycle 1 at -0.8%, -0.3% and 1% macroscopic strain.

by comparing Figures 2.13(a) and 2.13(b) at 1% macroscopic strain. At this point the stress distributions are dominated by the SCYS, which are the same for the two simulations.

The normalized stress distributions on Cycle 20, shown in Figure 2.14, exhibit some similarities and differences to the normalized stress distributions on Cycle 1. First, note that the normalized stress distributions on Cycles 1 and 20 at the point just prior to the knee of the macroscopic stress-strain curve (-0.8% macroscopic strain) are not directly comparable. Even though these two points on different cycles are at the same macroscopic strain level, they may correspond to different stages in the deformation. The macroscopic stresses differ between these two points in part due to continued cyclic hardening. The



(a)  $r_E = 1.0$



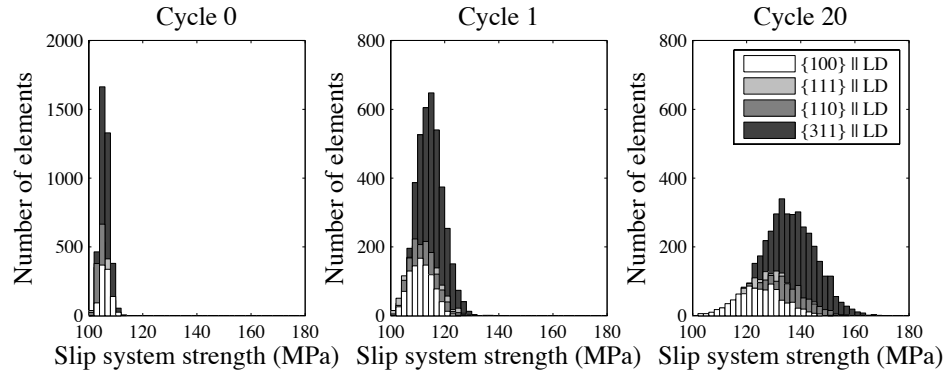
(b)  $r_E = 3.2$

Figure 2.14: Normalized deviatoric stress magnitudes for  $r_E = 1.0$  and  $r_E = 3.2$  on Cycle 20 at -0.8%, -0.3% and 1% macroscopic strain.

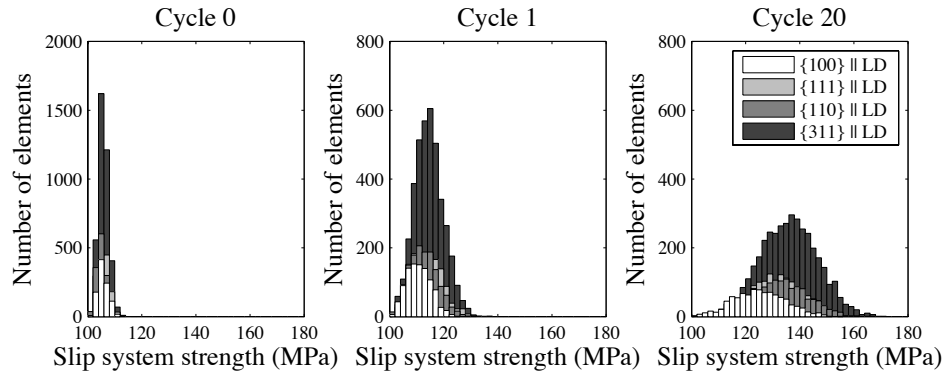
normalized stress distributions for Cycles 1 and 20 show similar trends in that the level of the elastic anisotropy influences the frequency distributions at -0.8% and -0.3% macroscopic strain, but not at 1.0% macroscopic strain.

The normalized stress distributions at 1.0% macroscopic strain on Cycles 1 and 20 differ from each other in terms of the spread of the stresses. With increased cycles, the standard deviations of the stress distributions increases for all fibers, which arises due to the evolution of the slip system strengths on each cycle. Because there exists variation in the crystal stresses, there also exists variation in the slip system shearing rates. Thus, the standard deviations of the slip system strengths also increase, as shown in Figure 2.15. Over the course of the cyclic loading, this leads to greater variation in the normalized stresses at 1%

macroscopic strain, which is shown in Figures 2.12-2.14.



(a)  $r_E = 1.0$



(b)  $r_E = 3.2$

Figure 2.15: Slip system strength distribution by crystallographic fiber at 1% macroscopic strain for  $r_E = 1.0$  and  $r_E = 3.2$ .

## 2.7 Conclusions

Several conclusions can be obtained from the simulations conducted in the current study. They are summarized in the following list:

- Lattice strain hysteresis behavior during cyclic loading exhibit an orientation dependent as well as elastic anisotropy dependent response. Hysteresis loops are evident in lattice strains versus macroscopic stress records.

The loops differ in slope and the degree to which they are open or closed. Both depend on the crystallographic fiber.

- The lattice strains for a particular fiber may exhibit a linear relation with macroscopic stress, which is characterized by a closed hysteresis loop. This behavior does not necessarily indicate that the crystals remain elastic over the whole cycle, as is demonstrated by examining the corresponding plastic deformation rates averaged along a fiber.
- The directional strength-to-stiffness ratio can be used to explain the lattice strain hysteresis behavior as well as the progression of yielding through the elastic-plastic transition for different fibers. In general, high directional strength-to-stiffness corresponds to the crystals yielding at a higher macroscopic stress, causing the crystals which have not yielded to exhibit an upward inflection in the lattice strains in the elastic-plastic transition regime since they are able to carry a higher proportion of the applied load.
- Open hysteresis loops indicate a difference in relative strength-to-stiffness from the average. Closed hysteresis loops indicate a relative strength-to-stiffness that is close to the average.
- After the elastic-plastic transition regime, crystals belonging to certain fibers tend to align more closely with certain vertex families of the SCYS. These crystal stresses in fully-developed plasticity are not dependent on the elastic anisotropy. The lattice strains in this regime, however, are influenced by the elastic anisotropy and the relative magnitudes of the SCYS vertex stresses.
- The distribution of crystal stress magnitudes in the elastic and elastic-plastic transition regime are influenced by the elastic anisotropy and the residual stresses. Even with continued strain hardening with cycles, these

crystal stresses on each cycle evolve toward the same SCYS vertex families in fully-developed plasticity irrespective of the elastic anisotropy.

- The standard deviation of the crystal stress magnitudes for a fiber increases with increasing cycles due to the different boundary conditions experienced by the crystals on each cycle with continued cyclic loading, leading to increased variation with cycles in the slip system strengths for the crystals belonging to a fiber.
- These results were found not to be significantly influenced by the absence of slip system hardening and in the presence of a strong rolling texture. However, these results hold only for an isotropic slip system hardening model because an anisotropic slip system hardening model may influence the evolution of the slip system strengths with cycles.

CHAPTER 3  
QUANTIFYING THE EVOLUTION OF CRYSTAL STRESSES DURING  
CYCLIC LOADING USING FINITE ELEMENT SIMULATIONS AND  
HIGH-ENERGY X-RAY DIFFRACTION

### 3.1 Abstract

A coordinated program of crystal-based finite element simulations and high-energy synchrotron x-ray diffraction experiments was conducted to establish a framework for quantifying the evolution of lattice strains in AA7075-T6 aluminum under *in situ* cyclic loading. The experiments and simulations were not intended to be used to validate each other, but rather they are used in a complementary manner to build a more complete picture of the evolving micromechanical state in polycrystals during cyclic loading. The simulations require information from the experiments to instantiate a virtual polycrystal and to define the single crystal elastic and plastic properties. Conversely, the experiments require information from the simulations to establish whether the measured cycle-by-cycle changes can be attributed to micromechanical evolution or experimental fluctuations. Lattice Strain Pole Figures (SPFs) for several  $\{hkl\}$  families were constructed from both the experiment and simulation data and compared at the same macroscopic stress level on each cycle. The SPFs demonstrate that the lattice strains exhibit a clear dependence on crystallographic orientation and that both the experiment and simulation lattice strains evolve with cycles. Using the simulations, orientation dependent trends are identified from the evolution of the crystal stress magnitudes and directions, the slip system activity and the slip system strengths. These trends can be explained in a consistent manner with respect to the single crystal yield surface.

## 3.2 Introduction

Traditional approaches to cyclic loading typically associated with fatigue involve constructing empirical correlations between the macroscopic cyclic loading conditions and fatigue life [59, 60], which typically do not include the evolution of stress-driven micromechanical phenomena during the life of a material. Although a mechanical component under cyclic loading may be subjected to a simple macroscopic stress state such as uniaxial tension, significant variations in the stress histories may be experienced at the crystal level due to the polycrystalline nature of most metals and metallic alloys. To better understand the processes by which fatigue damage initiates, it is necessary to measure and compute stresses at the level where the damage initiates, which is at the crystal level. The stress state of a crystal depends on the orientation of the crystal itself, anisotropy of the single crystal elastic and plastic properties as well as the orientations of neighboring crystals. More intensely stressed crystals can serve as defect or crack initiation sites.

Recent advances in both diffraction methods and polycrystal deformation modeling have enabled researchers to quantify the evolution of stresses and strains at the crystal level [3, 24, 46, 61]. *In situ* diffraction methods have enabled the measurement of elastic lattice strains in many different directions within crystals under monotonic or cyclic loading [7, 62]. Parallel computing and data parallel implementations of programs have allowed us to construct and cyclically load polycrystalline aggregates comprised of thousands of crystals, each crystal highly resolved by many finite elements. These experimental and computational capabilities can be tightly coupled to provide a more complete picture of the evolving micromechanical state of the material under cyclic loading.

In the current study, a coordinated program of crystal-based finite element simulations and high energy synchrotron x-ray diffraction experiments were conducted on the AA7075-T6 aluminum alloy under *in situ* cyclic loading to examine cycle-by-cycle changes in the lattice (elastic) strains. Since the elastic strains in crystals are directly related to the stresses through Hooke's law, the ability to measure and compute the lattice strain distributions offer direct insight into the evolving crystal stress distribution within a polycrystalline aggregate. Neither the simulations nor the experiments are regarded as the standard here, but rather we seek to use our experimental and computation capabilities in a tightly coupled and complementary manner to quantify the evolution of lattice strains within a polycrystalline aggregate under *in situ* cyclic loading.

The current study involves a direct comparison between lattice Strain Pole Figure (SPF) results from high energy synchrotron x-ray experiments and similar SPF results constructed from crystal-based, elastoplastic finite element simulations. The experiments interrogate the lattice strains for the  $\{111\}$ ,  $\{200\}$  and  $\{220\}$  families of crystal lattice planes oriented in many different sample directions, enabling SPFs to be constructed from the large number of lattice strain measurements collected. The elastic strains computed from the simulations are cast in an analogous form as the measured SPFs. The measured and simulated SPFs are compared at the same macroscopic stress level on several cycles along the loading history up to 100 cycles. The crystal stresses, slip system activity and slip system strengths from the simulations are also examined to identify trends in the evolution of these quantities and these trends are explained with respect to the single crystal yield surface.

### 3.3 Background

Over the past 40 years, electron microscopy has been widely employed to make surface observations of microstructural features such as dislocations and dislocations structures in cyclically loaded specimens [63]. Electron microscopy has made it possible to produce images of surface microstructural features resulting from cyclic plasticity such persistent slip bands (PSBs), cell wall structures, intrusions and extrusions [64–68]. Electron microscopy techniques such as transmission electron microscopy (TEM) and scanning electron microscopy (SEM) had important implications for the field of fatigue because they led to the discovery of the link between PSBs and the initiation of microcracks [69–71]. Various factors have been found to influence fatigue crack initiation, such as the grain size distribution, a corrosive environment, inclusions and precipitates within the material, the presence of residual stresses prior to fatigue loading and the presence of mean stresses during cyclic loading in AA7075-T6 aluminum, the material that we have chosen to investigate in the current study [72–75].

The limitation of electron microscopy techniques is that quantitative data pertaining to the stress state that drives these microstructural features cannot be obtained, which makes it difficult to establish a link between fatigue crack initiation and the micromechanical conditions which cause it. Often the stresses within crystals in a polycrystalline aggregate are assumed to be the same as the applied macroscopic stress and traditional approaches to fatigue have often focused on building empirical correlations between the macroscopic loading conditions and fatigue life [59, 76]. However, it has been shown that there can exist significant heterogeneity at the crystal level and that the stress state within a crystal in a polycrystalline aggregate may not be equal to the applied macroscopic stress [53, 77]. Since fatigue cracks initiate at the crystal level, an

effort must be made to quantify the micromechanical conditions leading up to the initiation of a crack.

Polychromatic and monochromatic neutron and synchrotron x-ray diffraction enable the measurement of lattice (elastic) strains within a crystalline sample from shifts in diffraction peaks. Although neutron diffraction has been extensively used to measure the evolution of lattice strains under *in situ* loading, slow collection times limit the amount of lattice strain information that can be obtained [3, 14, 46–48], making it harder to establish a complete picture of the evolving stress state of the crystals under *in situ* cyclic loading. High intensity synchrotron x-rays experiments conducted in transmission with high speed area detectors require much shorter collection times compared to neutron diffraction methods, enabling lattice strain data for many  $\{hkl\}$  families of crystal lattice planes in thousands of different directions to be collected simultaneously [7, 78, 79].

Numerical simulation of deforming polycrystals also provides a valuable tool for quantifying the evolution of stress and strain distributions at the crystal level. A variety of polycrystal deformation models are available to simulate the response of a polycrystalline aggregate, where different assumptions can be made regarding stress equilibrium and strain compatibility between crystals within the aggregate. Iso-stress and iso-strain modeling assumptions can be used [80, 81], while more complex formulations such the Taylor-Lin model, self-consistent polycrystal deformation models and finite element models have been used to model the elastic-plastic behavior of polycrystals [21, 29, 46, 61, 82–84].

There have been some previous efforts in investigating the behavior of a polycrystalline aggregate under *in situ* cyclic loading in terms of quantifying the evolution of the micromechanical response at the crystal level. Park et al.

[45] utilized synchrotron x-ray diffraction and a high speed rotating shutter to measure the real-time evolution of lattice strains in the loading and transverse directions of a copper specimen cycled at 20 Hz. The results of this study demonstrated that the lattice strains in the specimen loading and transverse directions were evolving with cycles, which led to the current efforts here to measure lattice strains in a larger number of sample directions. Huang et al. utilized neutron diffraction to measure the lattice strains in a nickel-based alloy under fully-reversed cyclic loading at a fixed macroscopic strain amplitude of 1% [48, 49]. The lattice strains in the specimen loading direction were measured at the maximum and minimum macroscopic strains as well as at zero macroscopic stress and strain. A couple of studies have been conducted on stainless steel using neutron diffraction techniques to measure the lattice strains in the specimen loading and transverse directions under *in situ* low cycle fatigue loading in strain control [46, 47].

### 3.3.1 Crystal orientations and crystallographic fibers

The description of the lattice orientation of a crystal within a polycrystalline aggregate requires two coordinate systems to be specified: a crystal coordinate system and a sample coordinate system. A rotation or orientation matrix,  $\mathbf{R}$ , transforms a vector in the crystal coordinate system,  $\mathbf{v}^c$ , to a vector in the sample coordinate system,  $\mathbf{v}^s$ , as follows:

$$\mathbf{R}\mathbf{v}^c = \mathbf{v}^s \quad (3.1)$$

A crystallographic fiber is represented as  $\mathbf{c} \parallel \mathbf{s}$  and it connects all orientations that align a particular crystal direction,  $\mathbf{c}$ , with a particular sample direction,  $\mathbf{s}$ :

$$\mathbf{R}\mathbf{c} = \pm \mathbf{s} \quad (3.2)$$

All orientations associated with a crystallographic fiber differ only by a rotation about a common direction. In Rodrigues orientation space, a crystallographic fiber appears as a straight line [32]. Crystallographic fibers provide a basis for comparison between simulations and diffraction measurements because a particular crystallographic fiber corresponds directly to a particular Bragg diffraction condition.

## 3.4 Experiments

### 3.4.1 Diffraction and lattice strains

A lattice Strain Pole Figure (SPF) experiment combines high-energy x-ray diffraction with *in situ* mechanical loading to measure lattice strains in polycrystalline samples in many different directions [7]. Each lattice strain measurement interrogates a subset of crystals within a polycrystalline sample. This type of experiment is referred to as an aggregate or powder diffraction experiment. An important characteristic of this type of experiment is that many crystals contribute to each lattice strain measurement. The experimental results presented in this chapter were taken from SPF experiments conducted by Jay Schuren of Cornell University at the A2 experimental station of the Cornell High Energy Synchrotron Source (CHESS).

Diffraction is fundamentally described by Bragg's law as follows [85]:

$$n\lambda = 2d_{c||s} \sin \theta_{c||s} \quad (3.3)$$

where  $n$  is an integer,  $\lambda$  is the wavelength,  $d_{c||s}$  is the lattice plane spacing for the subset of crystals with the plane normal  $c$  aligned with the sample direction  $s$ , and  $\theta_{c||s}$  is the Bragg angle.

A schematic of a typical diffraction experiment conducted in transmission is shown in Figure 3.1. The scattering vector,  $\mathbf{q}_{c||s}$ , is the bisector of the incoming and the diffracted x-ray beam. In a diffraction experiment, a shift in a diffraction peak corresponds to a change in the average lattice spacing among crystals with a particular  $\{hkl\}$  lattice plane normal aligned with the scattering vector.

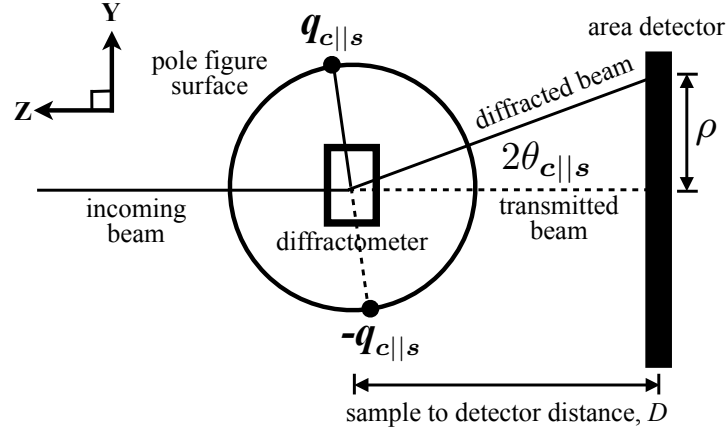


Figure 3.1: Schematic of a lattice Strain Pole Figure (SPF) experiment conducted in transmission. Here  $D$  and  $\rho$  are the sample to detector distance and the radial distance on the detector, respectively.

Using the experimental geometry and the radial position of each diffraction peak on the detector, the Bragg angle,  $\theta_{c||s}$ , in Equation (3.3) can be measured. From Equation (3.3), the mean lattice plane spacing,  $d_{c||s}$ , in the crystals satisfying a particular Bragg condition can be determined at any point in the deformation history. Given a reference (or unstrained) lattice plane spacing,  $d_{c||s}^0$ , the average lattice strain for the crystals with  $\{hkl\}$  plane normals aligned with scattering vector  $\mathbf{q}_{c||s}$  is defined as:

$$\epsilon_{c||s} = \frac{d_{c||s} - d_{c||s}^0}{d_{c||s}^0} \quad (3.4)$$

For cubic crystals, the initial or unstrained lattice plane spacing,  $d_{c||s}^0$ , is defined by a single lattice parameter.

### 3.4.2 Material and mechanical testing method

The AA7075-T6 aluminum alloy has a face-centered cubic (fcc) crystal structure and is commonly used in the construction of the wings and fuselage of both commercial and military aircraft. The Electron Backscatter Diffraction (EBSD) maps for the rolling and transverse planes of an AA7075-T6 aluminum sheet, which was manufactured by Alcoa, are shown in Figure 3.2. The average grain size of the material was determined to be approximately  $19.5 \mu\text{m}$  using EBSD and optical micrographs [79].

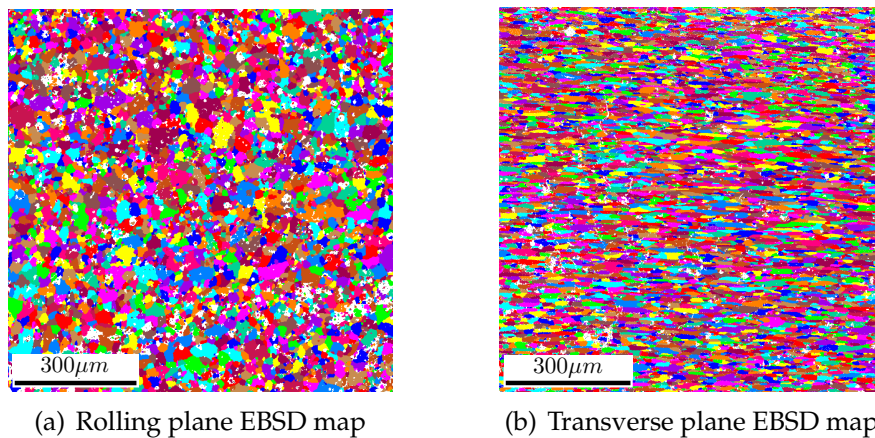


Figure 3.2: EBSD maps for the rolling and transverse planes of the AA7075-T6 aluminum alloy sheet.

The Orientation Distribution Function (ODF) of the material, shown in Figure 3.3, was determined from the experimental diffraction data using Rietveld analysis [86–88]. The ODF is required to assign the initial orientations of the grains in the simulations.

The AA7075-T6 specimens were loaded using an electromagnetic loadframe. The loadframe is mounted within a two axis diffractometer which allows for re-orientation of the loaded samples to increase the number of independent diffraction measurements [78]. The specimens were cycled in zero-tension cyclic load-

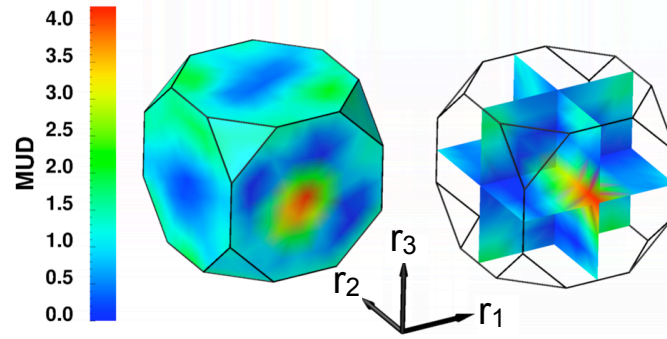


Figure 3.3: The ODF determined from the experiments, plotted over the cubic fundamental region of Rodrigues orientation space. The ODF is represented in terms of Multiples of Uniform Distribution (MUD).

ing between 0 MPa and 572 MPa. The specimens were loaded to the maximum macroscopic load of 572 MPa on each cycle, then the macroscopic load was reduced to 90% of the target value (515 MPa) to conduct the diffraction measurements. The macroscopic load was held at the reduced load level to reduce creep effects while sample rotations and diffraction measurements were being conducted [3]. The lattice strain diffraction measurements were conducted at 515 MPa on cycles 0, 1, 5, 10, 20, 50, 100, 500 and 1000. More details on the experimental procedure and illustrations of the experimental setup can be found in [79].

Diffraction of a polycrystalline sample in a SPF powder experiment produces a series of concentric rings, known as Debye rings. The diffraction pattern is captured using a MAR345 area detector. Each concentric Debye ring corresponds to diffraction from a particular  $\{hkl\}$  family of crystal lattice planes. Each point on a Debye ring corresponds to a crystallographic fiber in Rodrigues space. To sample an equiaxed region of Rodrigues space and to increase the number of crystals contributing to a lattice strain measurement, the sample was reoriented, or rocked, by  $\pm 2.5^\circ$  about two axes: a vertical axis normal to the x-

ray beam and the specimen loading direction (LD). A more detailed description of this rocking technique is available in [79].

### 3.4.3 Lattice Strain Pole Figures (SPFs)

By measuring lattice strains in many sample directions, we are able to construct SPFs, which are three dimensional representations of the micromechanical state as a function of crystallographic orientation. A SPF is constructed for a specific  $\{hkl\}$  family of lattice planes in many different measurement directions,  $s$ , where each lattice strain measurement is plotted at the intersection of its scattering vector,  $\mathbf{q}_{c||s}$ , and the surface of a unit sphere. Increased SPF coverage is achieved by rotating the sample relative to the x-ray beam.

A point on a pole figure corresponds to a crystallographic fiber. A point on the  $\{200\}$  pole figure with a scattering vector in the sample LD direction corresponds to the  $\{200\} \parallel \text{LD}$  crystallographic fiber shown in Figure 3.4(a). The scattering vectors on the pole figure encompassed by a  $\pm 2.5^\circ$  rock about two axes are shown in Figure 3.4(b). Each lattice strain measurement plotted on a SPF corresponds to the average normal strain among all crystals belonging to a particular crystallographic fiber. The SPF powder experiment does not have the ability to resolve different crystal orientations lying along a crystallographic fiber. However, the exact orientation of each crystal is known in the finite element simulations and the orientation of each crystal can be plotted as a point in Rodrigues space.

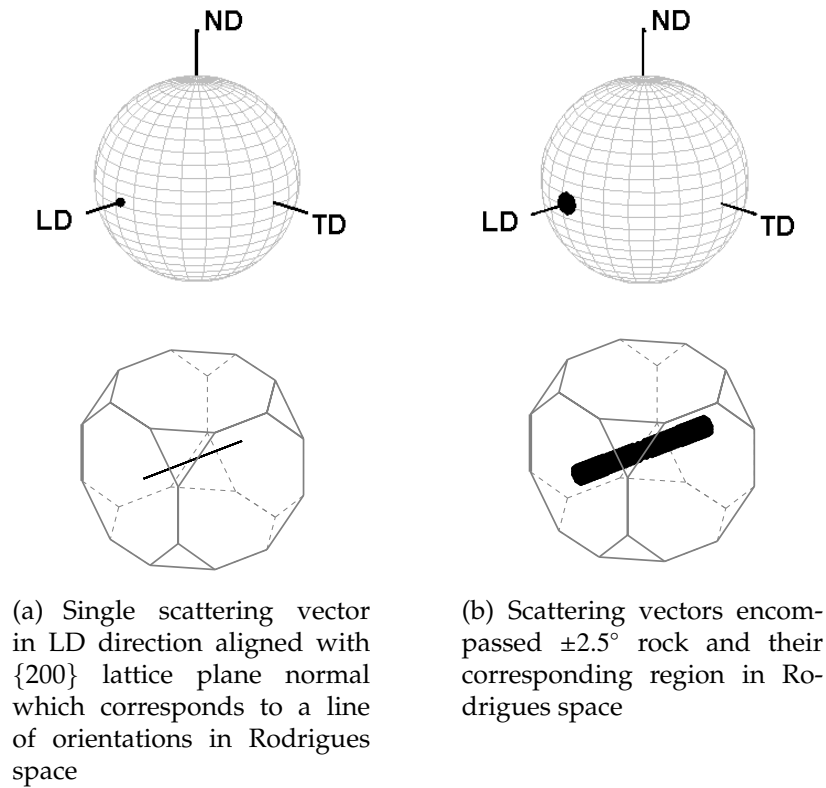


Figure 3.4: Relationship between a point on a pole figure and a crystallographic fiber in Rodrigues space

### 3.4.4 Determination of lattice strain uncertainty

The use of the SPF powder experiment technique to investigate cycle-by-cycle changes in lattice strains for many different sample directions requires careful consideration of the uncertainty associated with each lattice strain measurement. Without an estimate for the uncertainty, it is not possible to separate real micromechanical evolution from random experimental fluctuations. The method of quantifying the uncertainty associated with a lattice strain measurement was developed by Schuren et. al. [79] for a monotonic tensile loading SPF experiment on AA7075-T6 aluminum, the same material used in the current study.

The uncertainty of a lattice strain measurement in the experiment,  $U_{c||s}$ , has

a contribution from the instrument,  $U_{c||s}^i$ , and a contribution from the material,  $U_{c||s}^m$  [79]. The total uncertainty,  $U_{c||s}$ , associated with a particular lattice strain measurement is thus computed as:

$$U_{c||s} = \sqrt{U_{c||s}^i{}^2 + U_{c||s}^m{}^2} \quad (3.5)$$

The material portion of the uncertainty,  $U_{c||s}^m$ , is influenced by the number of crystals contributing to a lattice strain measurement, grain morphology and the standard deviation of the lattice strains among the crystals contributing to each measurement. The lattice strains from the simulations are required to compute the material portion of the uncertainty,  $U_{c||s}^m$ , demonstrating the complementary nature of the experiments and simulations in this study. More details on how  $U_{c||s}^i$  and  $U_{c||s}^m$  are computed can be found in [79].

## 3.5 Simulations

### 3.5.1 Numerical formulation

A crystal-based elastoplastic finite element model is used to simulate the response of a virtual polycrystalline specimen under similar loading conditions as in the SPF experiments. An elastoplastic constitutive model, which dictates the behavior of a single crystal, is implemented within a finite element formulation which dictates the behavior of an aggregate of crystals. A complete description of the finite element model and its implementation can be found in [35–37]. The capabilities of the single crystal constitutive model and its finite element implementation are briefly summarized here. The crystal elastoplastic constitutive model has the following features:

- multiplicative decomposition of the crystal deformation gradient into elastic, plastic and rotational portions
- anisotropic elasticity appropriate to the fcc crystal structure
- plastic deformation by rate-dependent restricted slip on the 12  $\{111\}\langle 110\rangle$  slip systems associated with the fcc crystal structure
- strain hardening via integration of a modified Voce law for evolution of the slip system strengths
- texture evolution through crystallographic lattice reorientation

This crystal constitutive model is implemented in a finite element formulation which has the following capabilities:

- three-dimensional grain geometries, where each grain is resolved with multiple finite elements
- weak form of the equations of equilibrium
- implicit time-integration of the constitutive equations for numerical stability
- scalable parallel implementation using Fortran 90 and interprocessor communication based on the Message Passing Interface (MPI) standard

Crystallographic slip through the crystal lattice is assumed to be the dominant mode of plastic deformation. The deformation gradient,  $\mathbf{F}$ , experienced by a crystal in the current configuration is decomposed into an elastic, plastic and rotational portion as follows [35]:

$$\mathbf{F} = \mathbf{V}^* \mathbf{R}^* \mathbf{F}^P \quad (3.6)$$

where  $\mathbf{F}^P$  is the purely plastic part of  $\mathbf{F}$ ,  $\mathbf{R}^*$  is the lattice rotation and  $\mathbf{V}^*$  is the elastic stretch.

Plastic deformation occurs by crystallographic slip on a restricted number of slip systems. For each  $\alpha$ -slip system, a slip direction,  $\hat{\mathbf{s}}^\alpha$ , and a slip plane normal,  $\hat{\mathbf{m}}^\alpha$ , are defined. The plastic shearing rate on the  $\alpha$ -slip system,  $\dot{\gamma}^\alpha$ , is related to the crystal stress through a power law form:

$$\dot{\gamma}^\alpha = \dot{\gamma}_0^\alpha \left( \frac{|\tau^\alpha|}{g^\alpha} \right)^{\frac{1}{m}} \text{sgn}(\tau^\alpha) \quad (3.7)$$

where  $g^\alpha$  is the slip system strength,  $\dot{\gamma}_0^\alpha$  is a reference shear rate and  $m$  is the rate sensitivity of slip. The resolved shear stress,  $\tau^\alpha$ , is the projection of the deviatoric part of the Kirchhoff stress,  $\boldsymbol{\tau}'$ , on the  $\alpha$ -slip system:

$$\tau^\alpha = \boldsymbol{\tau}' : \text{sym}(\hat{\mathbf{s}}^\alpha \otimes \hat{\mathbf{m}}^\alpha) \quad (3.8)$$

The Kirchhoff stress,  $\boldsymbol{\tau}$ , is related to the crystal elastic strains,  $\boldsymbol{\epsilon}$  through Hooke's law:

$$\begin{pmatrix} \tau_{11} \\ \tau_{22} \\ \tau_{33} \\ \tau_{23} \\ \tau_{13} \\ \tau_{12} \end{pmatrix} = \begin{bmatrix} C_{11} & C_{12} & C_{12} & 0 & 0 & 0 \\ C_{12} & C_{11} & C_{12} & 0 & 0 & 0 \\ C_{12} & C_{12} & C_{11} & 0 & 0 & 0 \\ 0 & 0 & 0 & C_{44} & 0 & 0 \\ 0 & 0 & 0 & 0 & C_{44} & 0 \\ 0 & 0 & 0 & 0 & 0 & C_{44} \end{bmatrix} \begin{pmatrix} \epsilon_{11} \\ \epsilon_{22} \\ \epsilon_{33} \\ \epsilon_{23} \\ \epsilon_{13} \\ \epsilon_{12} \end{pmatrix} \quad (3.9)$$

where  $C_{11}$ ,  $C_{12}$  and  $C_{44}$  are the single crystal elastic moduli for the cubic crystal structure.

The slip system strengths for each crystal,  $g$ , evolve according to an isotropic hardening law ( $g^\alpha = g$ ):

$$\dot{g} = h_0 \left( \frac{g_s(\dot{\gamma}) - g}{g_s(\dot{\gamma}) - g_0} \right) \dot{\gamma}, \quad g_s(\dot{\gamma}) = g_{s0} \left( \frac{\dot{\gamma}}{\dot{\gamma}_{s0}} \right)^{m'} \quad (3.10)$$

where  $\dot{\gamma} = \sum_\alpha |\dot{\gamma}^\alpha|$  is the sum of the slip system shearing rates and  $h_0$ ,  $g_0$ ,  $g_{s0}$ ,  $m'$  are slip system hardening parameters.

### 3.5.2 Virtual specimen and simulation of cyclic loading tests

In the diffraction experiment, only a small volume of the specimen is irradiated by the x-ray beam. This volume is referred to as the diffraction volume and it is modeled in the simulations as a virtual polycrystal specimen. A finite element mesh in the shape of a cube is instantiated with 2916 complete rhombic dodecahedra grains to represent the virtual polycrystalline specimen. Each complete rhombic dodecahedra grain consists of 48 10-node tetrahedra elements but there are also partial grains which make up the flat surfaces of the finite element mesh. The mesh is comprised of a total of 192,000 finite elements. The finite elements contributing to a grain are assigned the same initial lattice orientation but these orientations are allowed to evolve independently with deformation. The ODF of the AA7075-T6 aluminum sheet, shown in Figure 3.3, is randomly sampled to generate a list of orientations which are assigned to the grains of the finite element mesh.

The virtual specimen is loaded under uniaxial, zero-tension cyclic loading conditions ( $R = 0$ ), similar to the loading conditions applied in the experiment. The sample LD, TD and ND directions correspond to the X, Y and Z directions of the finite element mesh, respectively. A constant velocity was applied on the positive X surface of the finite element mesh, while the  $X = 0$  face of the mesh was constrained in the X-direction. The two positive Y and Z surfaces of the mesh are traction-free, while the  $Y = 0$  and  $Z = 0$  surfaces had symmetry boundary conditions imposed. Both the experiments and simulations were conducted in load control with a target macroscopic engineering stress of 572 MPa on each cycle. Lattice strain data between the experiments and simulations were compared at 90% of the target macroscopic load on each cycle. Although the AA7075-T6 specimen in the experiments was cycled up to at least 1000 cy-

cles, the virtual specimen was only cycled up to 100 cycles due to the excessive computation time and resources required to achieve 500 and 1000 cycles in the simulations.

The simulations also do not take into account the residual stress distribution which is present in the material prior to loading because assigning a residual stress state to each element in the finite element mesh while satisfying equilibrium and compatibility is a non-trivial problem. Therefore, for the purposes of this study, the crystals are assumed have a zero initial stress state prior to cyclic loading in the simulations.

### **3.5.3 Determination of model constants**

Data from the monotonic loading experiments (which will be referred to as Cycle 0) is used to determine the single crystal elastic and plastic properties for the AA7075-T6 aluminum alloy. The single crystal elastic moduli for pure aluminum may not be suitable for AA7075-T6 because of the addition of alloying elements and the presence of precipitates in the material can perturb the single crystal elastic moduli from those of the pure material. The single crystal elastic anisotropy ratio and the hardening constants are determined by conducting two different suites of simulations.

The first suite of simulations is used to determine the hardening constants of AA7075-T6. Before conducting a simulation, the elastic and plastic properties of the material need to be specified as inputs. In the first suite of simulations, the single crystal elastic moduli ( $C_{11}$ ,  $C_{12}$  and  $C_{44}$ ) for pure aluminum reported by Hosford [34] was used, keeping in mind that these will not be the final values of the single crystal elastic moduli used for AA7075-T6. The hardening constants in Equation (3.10) are varied in this first suite of simulations until a good

match between the experiment and simulation macroscopic engineering stress-strain curves is obtained. The hardening constants determined from this first set of simulations are shown in Table 3.1. The comparison of the simulation and experiment macroscopic stress-strain curves for monotonic loading (Cycle 0) using the hardening constants in Table 3.1 is shown in Figure 3.5.

$h_0$ (MPa)	$g_0$ (MPa)	$g_{s0}$ (MPa)	$m$	$m'$	$\dot{\gamma}_0$ ( $s^{-1}$ )	$\dot{\gamma}_{s0}$ ( $s^{-1}$ )
195	218	280	0.007	0.0	1.0	$5 \times 10^{10}$

Table 3.1: Slip system and hardening model parameters determined for AA7075-T6 in the first suite of simulations.

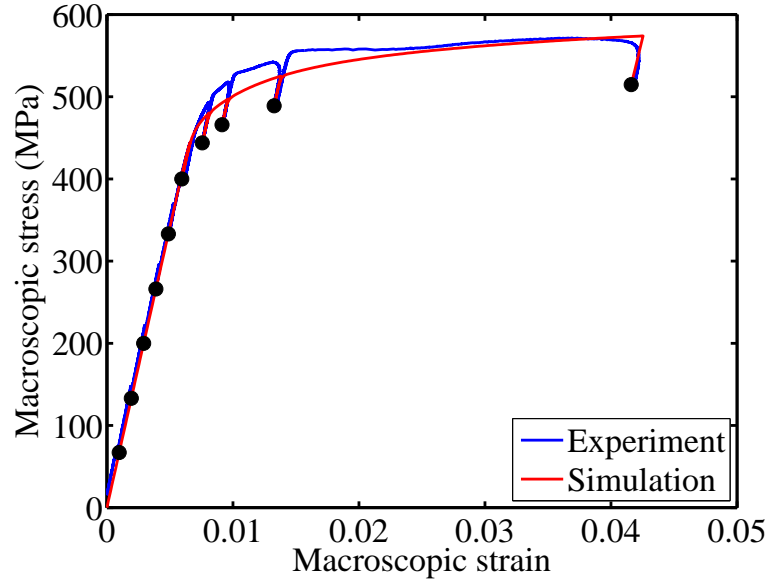


Figure 3.5: Macroscopic stress-strain curves from the experiments and simulations on Cycle 0. Points are indicated on the macroscopic stress-strain curve where diffraction measurements were conducted. Strain Pole Figure (SPF) comparisons were made between the experiments and simulations at the macroscopic stress levels corresponding to these points.

Once the hardening constants were determined, a second suite of simulations was conducted to determine the single crystal elastic anisotropy,  $r_E$ . The

single crystal elastic anisotropy ratio,  $r_E$ , is defined as:

$$r_E = \frac{E_{\langle 111 \rangle}}{E_{\langle 100 \rangle}} \quad (3.11)$$

where  $E_{\langle 111 \rangle}$  is the stiffness in the  $\langle 111 \rangle$  crystal direction and  $E_{\langle 100 \rangle}$  is the stiffness in the  $\langle 100 \rangle$  crystal direction.

For crystals with the cubic crystal structure, three independent elastic constants are required to describe the elastic response of the material. In addition to the single crystal elastic anisotropic ratio,  $r_E$ , two average parameters are also defined: an average Young's modulus,  $E_{\text{avg}}$  and an average Poisson's ratio,  $\nu_{\text{avg}}$  for a polycrystalline aggregate with a uniform ODF. To simplify the problem, the effect of texture on  $E_{\text{avg}}$  and  $\nu_{\text{avg}}$  was not taken into account in the current study.

The single crystal elastic anisotropy,  $r_E$ , of the material and correspondingly, the single crystal elastic moduli are determined through the following procedure using the second suite of simulations:

1. Starting from the single crystal elastic moduli ( $C_{11}$ ,  $C_{12}$  and  $C_{44}$ ) for pure aluminum reported by Hosford [34], where  $r_E = 1.2$ ,  $r_E$  and  $\nu_{\text{avg}}$  are kept constant and single crystal elastic moduli are changed such that  $E_{\text{avg}}$  in the simulations matches the Young's modulus of the macroscopic stress-strain curve in the monotonic tensile loading experiments (Cycle 0).
2. Using the new value of  $E_{\text{avg}}$  determined in Step 1,  $E_{\text{avg}}$  and  $\nu_{\text{avg}}$  are now kept constant while the single crystal elastic moduli are changed to result in  $r_E$  values in the range of 1.2–1.7. Six simulations were conducted for  $r_E$  in the range of 1.2–1.7, in increments of 0.1. The method of varying the single crystal elastic moduli to result in different values of  $r_E$  has been described in detail in Refs. [1, 3].

3. The SPFs generated from the simulations for different values of  $r_E$  are compared to the measured SPFs at various macroscopic stress levels along the macroscopic stress-strain curve on Cycle 0, as shown in Figure 3.5. The value  $r_E$  of which results in the minimum difference between all SPFs at all macroscopic stress levels is chosen as the final value of  $r_E$  and is used for the cyclic loading simulations.

By taking a least-squares difference between the experiment SPFs and simulation SPFs at the macroscopic stress values indicated in Figure 3.5, it was determined that the value of  $r_E = 1.3$  resulted in the best match between the experiment and simulation SPFs. The single crystal elastic moduli corresponding to the value of  $r_E = 1.3$  are shown in Table 3.2. Using this value of  $r_E$ , the cyclic simulations were then conducted and the resulting macroscopic stress-strain curve for cyclic loading up to 100 cycles is shown in Figure 3.6. It is observed that the macroscopic stress-strain curve in the simulations accumulates more plastic strain compared to the macroscopic stress-strain curve from the experiments.

$C_{11}$ (GPa)	$C_{12}$ (GPa)	$C_{44}$ (GPa)
102.223	59.641	57.001

Table 3.2: Single crystal elastic moduli corresponding to  $r_E = 1.3$  determined for AA7075-T6.

A second simulation conducted using  $r_E = 1.35$  demonstrated no significant changes in the evolution of the lattice strains with cycles, which is expected when there is only a small difference in  $r_E$ . Therefore, the results for  $r_E = 1.35$  will not be presented here.

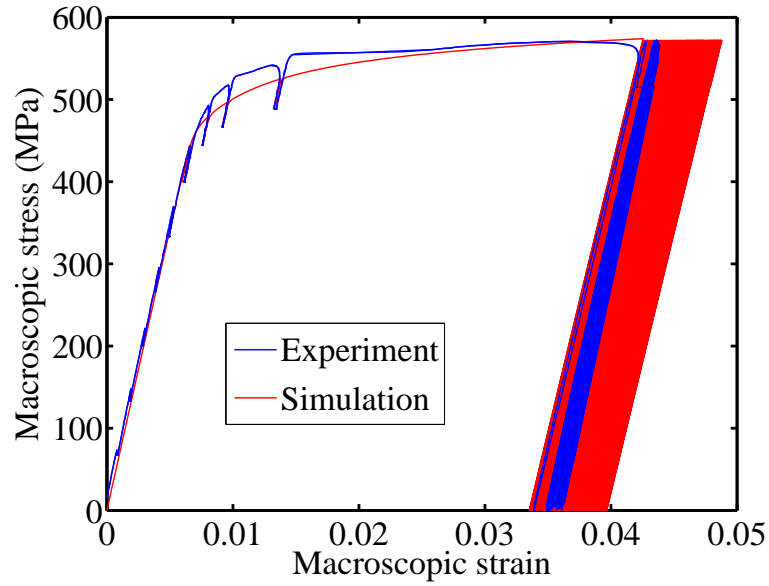


Figure 3.6: Macroscopic stress-strain curves from the experiments and simulations for cyclic loading.

### 3.5.4 Generation of SPFs from simulated data

The simulation results can be compared to individual lattice strain diffraction measurements using crystallographic fibers, which were defined in Section 3.3.1, as the basis for comparison. A crystallographic fiber corresponds directly to a particular Bragg diffraction condition, where  $c$  corresponds to the  $\{hkl\}$  lattice plane normal and  $s$  is aligned with a particular scattering vector,  $\mathbf{q}_{c\parallel s}$ .

To construct a SPF from the simulation data for a particular  $\{hkl\}$  family of lattice planes, the list of measurement directions in the experiment and an angle of resolution is required. The lattice orientation of each element in the mesh is examined to determine whether its  $\{hkl\}$  lattice plane normal and a particular measurement direction,  $s$ , are aligned to within the angle of resolution. The angle of resolution chosen in the simulation is  $5^\circ$  to ensure that a statistically significant number of elements are contributing to a crystallographic fiber.

For the  $n$  number of elements in the mesh whose orientation belongs to a

particular crystallographic fiber to within a given tolerance, its full elastic strain tensor,  $\epsilon$ , is projected in the measurement direction. The lattice strain value,  $\epsilon_{c\parallel s}$ , is then computed by averaging all the projected values of  $\epsilon$  among the  $n$  elements belonging to the crystallographic fiber:

$$\epsilon_{c\parallel s} = \left( \sum_{i=1}^n s_i \cdot \epsilon_i(\mathbf{R}_i) \cdot s_i^T \right) / n \quad (3.12)$$

As in the experiments, the value of  $\epsilon_{c\parallel s}$  can then be plotted as a point on a pole figure at the intersection of a unit sphere and its corresponding scattering vector,  $\mathbf{q}_{c\parallel s}$ .

## 3.6 Results

### 3.6.1 Residual lattice strain distribution

The lattice strain distribution at a macroscopic stress of 0 MPa is measured prior to loading in the experiments. The lattice strains present in the macroscopically unloaded state are often referred to as residual strains. The residual lattice strain pole figures are shown in Figure 3.7. The  $\{200\}$  SPF has the largest residual lattice strains compared to the other  $\{hkl\}$  pole figures. The compressive residual lattice strains are also much larger compared to the tensile residual lattice strains for the  $\{200\}$  SPF. It is important to note that in the simulations, the crystals are not initialized with a residual stress state. Therefore, the simulation SPFs prior to loading are zero everywhere on the pole figure and are not presented here.

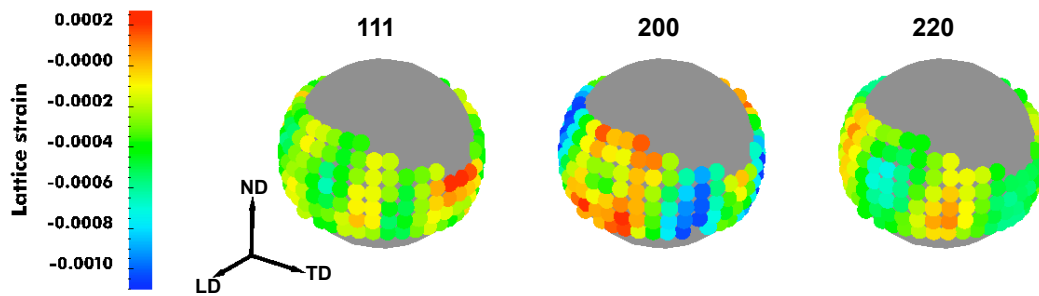
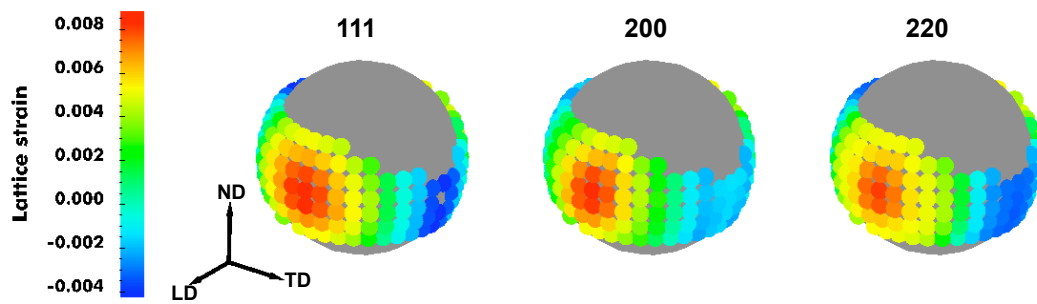


Figure 3.7: Measured residual SPFs at a macroscopic stress of 0 MPa, prior to loading. Note that the colorbar scale is not symmetric.

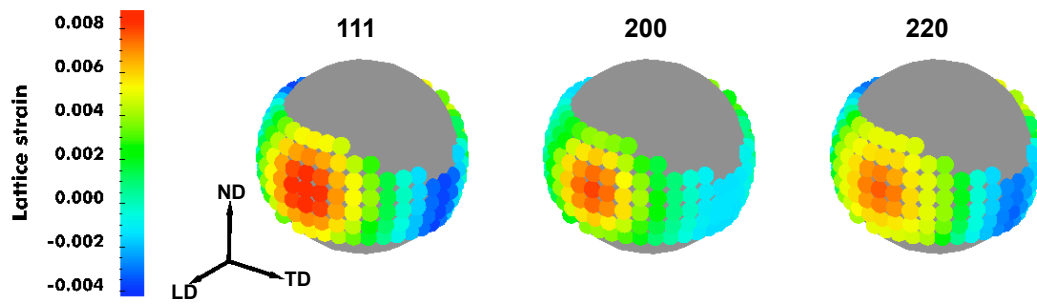
### 3.6.2 Comparison between measured and simulated SPFs

The  $\{111\}$ ,  $\{200\}$  and  $\{220\}$  SPFs from the experiments and simulations on Cycle 0 are shown in Figures 3.8(a) and 3.8(b). The comparison between the experiment and simulation SPFs are made at the last point indicated in Figure 3.5, which is at 90% of the maximum macroscopic engineering stress of 572 MPa and corresponds to approximately 515 MPa. The differences between the measured and simulated SPFs on Cycle 0 are shown in Figure 3.8(c). Although the experiment and simulation SPFs appear to exhibit the same trends over the pole figure, the differences between the experiment and simulation SPFs are non-negligible, which indicates that the match between the experiment and simulation SPFs can be improved. It is also observed that the  $\{200\}$  SPF, which has the largest residual strains as shown in Figure 3.7, also has the largest difference between the measured and simulated SPFs (Figure 3.8(c)).

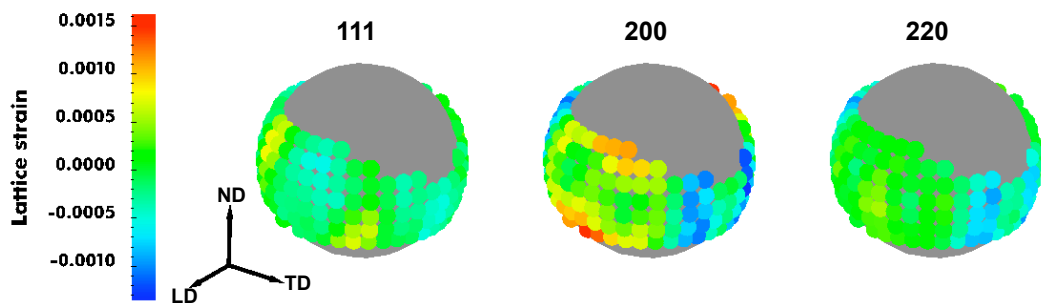
The measured and simulated SPFs at 515 MPa on Cycle 100 are shown in Figure 3.9. The SPFs for other cycles are not shown here because they exhibit trends similar to those in Figures 3.8 and 3.9. The lattice strains evolve between Cycle 0 and Cycle 100 but these differences are not discernible between Figure 3.8 and Figure 3.9 because the changes are at least an order of magnitude smaller than



(a) Experiment SPFs



(b) Simulation SPFs

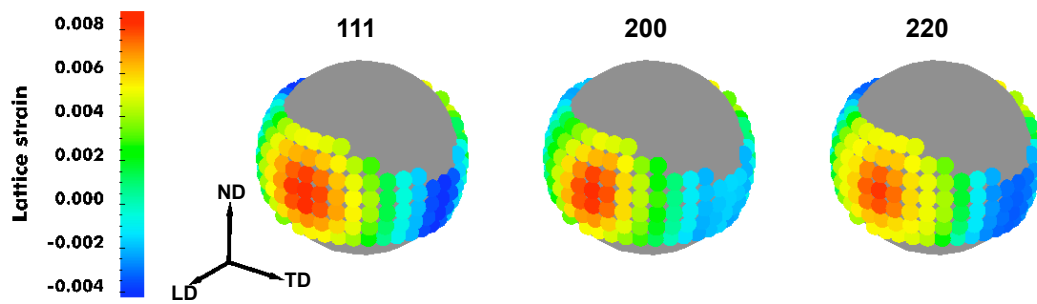


(c) Difference between experiment and simulation SPFs

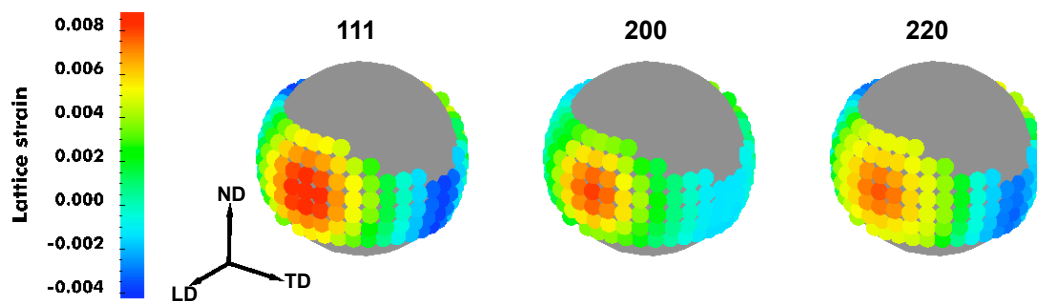
Figure 3.8: Experiment, simulation and difference SPFs for three different  $\{hkl\}$ s at 515 MPa on Cycle 0. Note that the colorbar scale for Figure 3.8(c) is different.

the lattice strains. Therefore, changes in the SPFs between two cycles will be plotted as difference SPFs in Section 3.6.3.

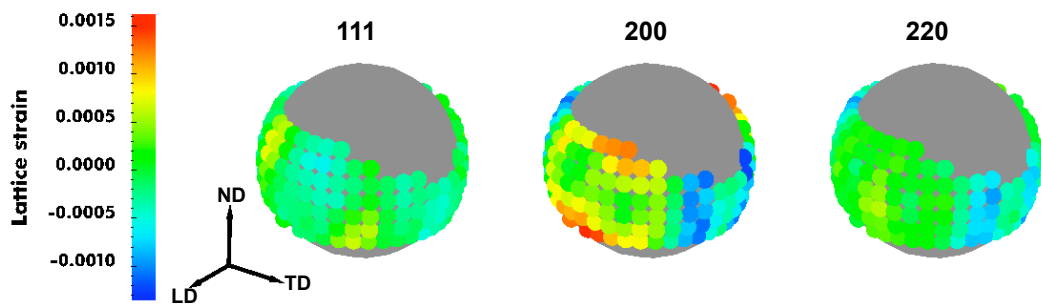
For Cycle 0 and Cycle 100, the lattice strain values in the experiment and simulation SPFs are on the same order of magnitude and also exhibit similar



(a) Experiment SPFs



(b) Simulation SPFs



(c) Difference between experiment and simulation SPFs

Figure 3.9: Experiment, simulation and difference SPFs for three different  $\{hkl\}$ s at 515 MPa on Cycle 100. Note that the colorbar scale for Figure 3.9(c) is different.

trends which are consistent with the macroscopic loading direction. A tensile lattice strain develops in the crystals with scattering vectors close to the specimen loading direction (LD) and a compressive lattice strain develops in the crystals with scattering vectors close to the specimen transverse direction (TD),

which is consistent with the Poisson effect. The lattice strains vary gradually from tensile to compressive as a scattering vector moves from the LD to the TD direction. Figures 3.8(c) and 3.9(c) demonstrate that on Cycle 0 and Cycle 100, the largest difference between the experiment and simulation SPFs occurs for the {200} SPF, particularly for the scattering vectors along the edges of the pole figure coverage. The magnitude of the difference between the experiment and simulation SPFs on Cycle 100 is also comparable to the magnitude of the difference between the experiment and simulation SPFs on Cycle 0.

### 3.6.3 Evolution of SPFs with cycles

The differences between the SPFs on Cycles 1, 10 and 100 with respect to Cycle 0 are presented in Figures 3.10–3.12. Examining first the difference between Cycle 1 and Cycle 0 for the measured SPFs (Figure 3.10(a)), it is observed that for some points on the difference SPFs, the differences are on the order of the experimental uncertainty [79]. Therefore, it is difficult to observe definitive trends in the evolution of the lattice strains between Cycle 1 and Cycle 0. The difference between Cycle 1 and Cycle 0 for the simulation SPFs (Figure 3.10(b)) develop clear patterns on the pole figure, but these differences are an order of magnitude smaller compared to the differences observed in the experiments and also cannot be used to draw conclusions regarding the evolution of the lattice strains after only one cycle.

The differences between the Cycle 10 and Cycle 0 SPFs for the experiments and the simulations are shown in Figure 3.11. The experimental SPFs evolve at a faster rate compared to the simulation SPFs in the first ten cycles. For the experimental SPFs, the lattice strains close to the LD direction increase while the lattice strains close to the TD direction decrease after ten cycles across all the

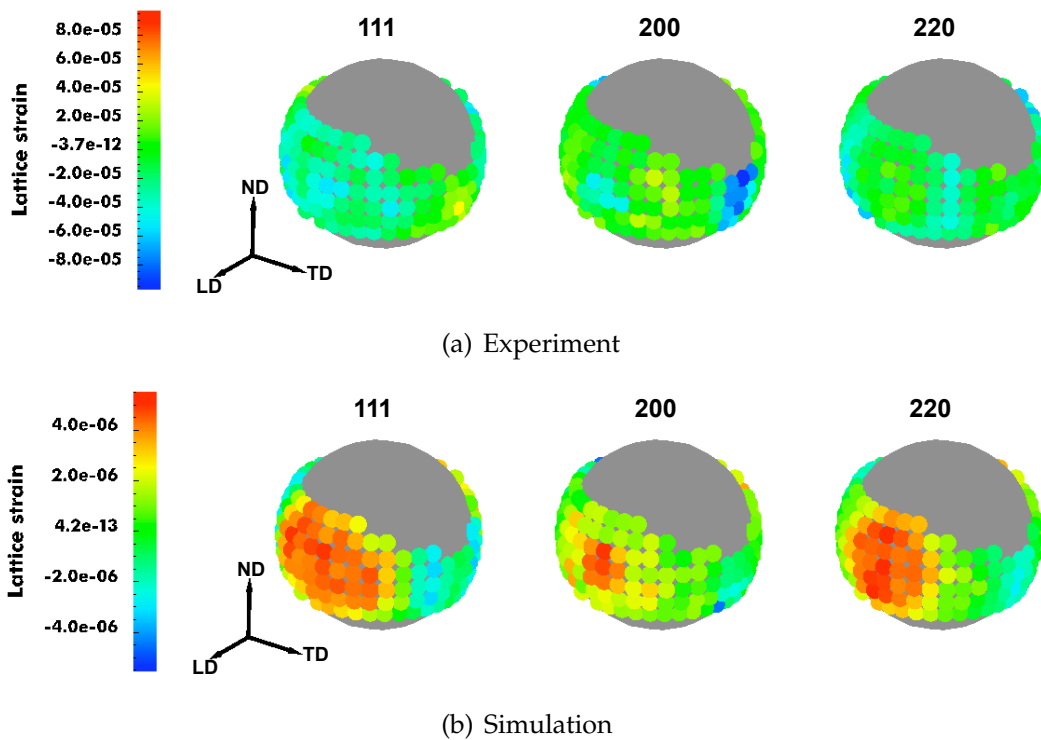


Figure 3.10: Difference SPFs between Cycle 1 and Cycle 0 at 515 MPa for the experiments and simulations, where the Cycle 0 SPF is subtracted from the Cycle 1 SPF. Note that the colorbar scales for the two figures are different.

pole figures. The difference SPFs for the simulations are an order of magnitude smaller than the difference SPFs for the experiments when comparing Cycles 10 and 0, as seen in Figure 3.11(b).

The differences between the Cycle 100 and Cycle 0 SPFs for the experiments and the simulations are shown in Figure 3.12. Comparing Figure 3.11(a) and Figure 3.12(a), it is observed that most changes in the measured lattice strains occur during the first ten cycles. In the measured SPFs, the lattice strains close to the LD direction increase with cycles, while the lattice strains close to the TD direction decrease with cycles for all the pole figures. Only the simulation  $\{111\}$  and  $\{220\}$  SPFs evolve in similar directions as the measured SPFs. The lattice strains close to the LD direction increase with cycles and the lattice strains close

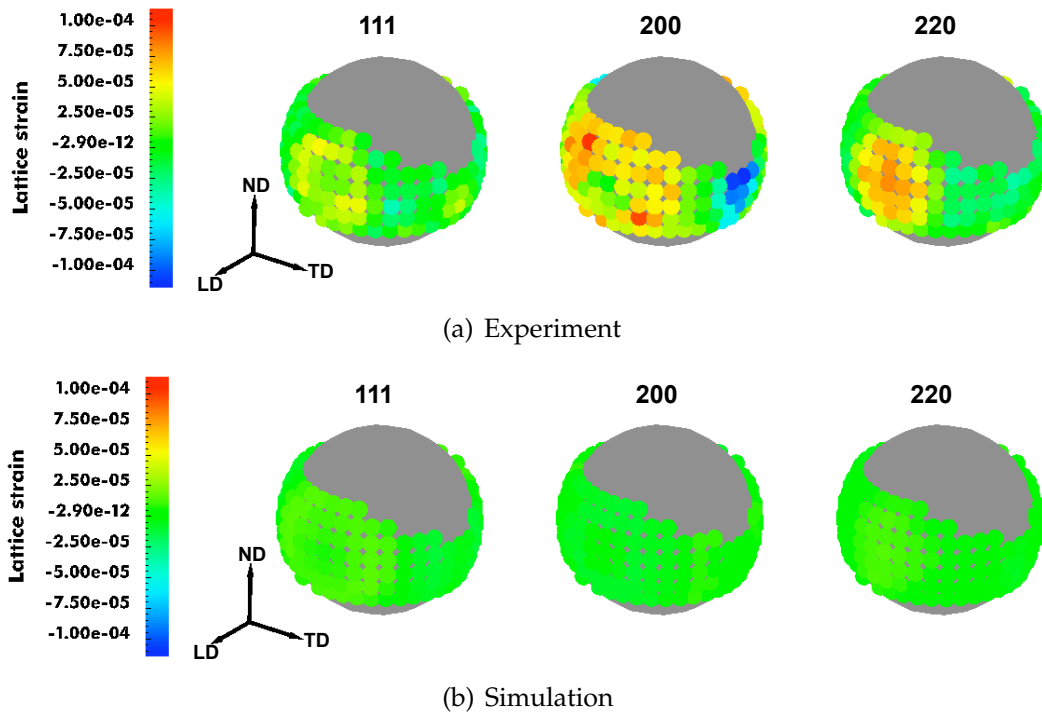


Figure 3.11: Difference SPFs between Cycle 10 and Cycle 0 at 515 MPa for the experiments and simulations, where the Cycle 0 SPF is subtracted from the Cycle 10 SPF.

to the TD direction decrease with cycles for the  $\{111\}$  and  $\{220\}$  simulation SPFs, but at a slower rate compared to the experiment. For the simulated  $\{200\}$  SPF, however, the lattice strains close to the LD direction tend to decrease with cycles while the lattice strains close to the TD direction tend to increase with cycles. This trend observed in the evolution of the simulated  $\{200\}$  SPF is not consistent with the evolution of the measured  $\{200\}$  SPF.

The changes in the lattice strains between Cycle 100 and Cycle 0 for the simulation SPFs are approximately on the same order of magnitude as the experiment SPFs. This indicates that after the first ten cycles, the lattice strains in the experiment evolve at a slower rate compared to the lattice strains in the simulations.

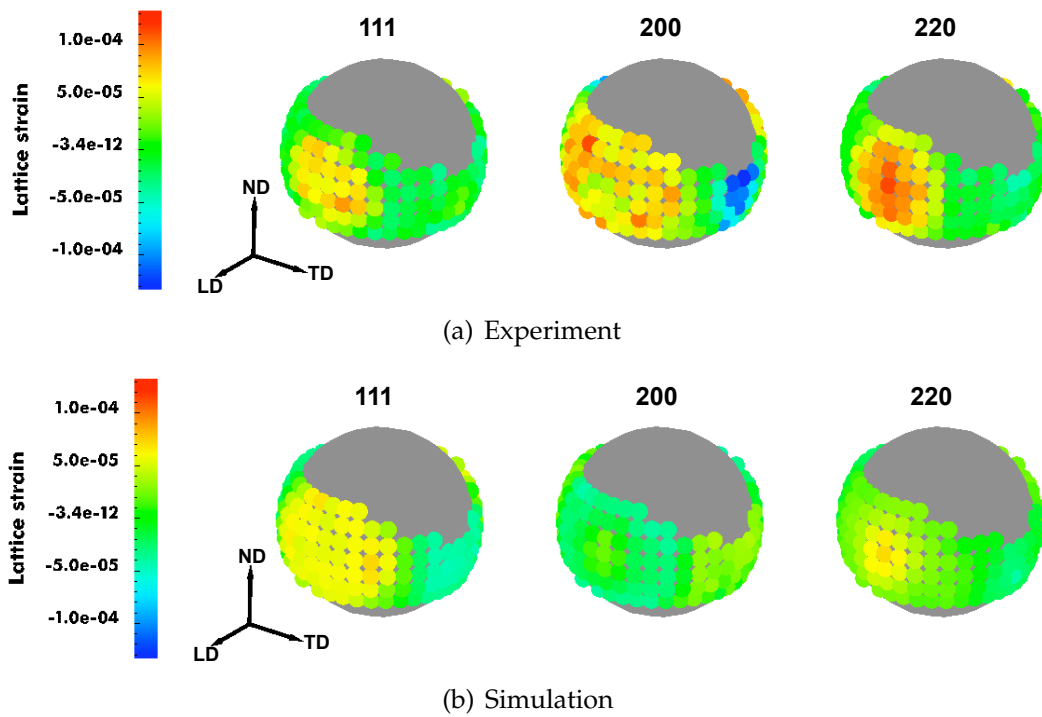


Figure 3.12: Difference SPFs between Cycle 100 and Cycle 0 at 515 MPa for the experiments and simulations, where the Cycle 0 SPF is subtracted from the Cycle 100 SPF.

### 3.6.4 Evolution of the computed crystal stresses with cycles

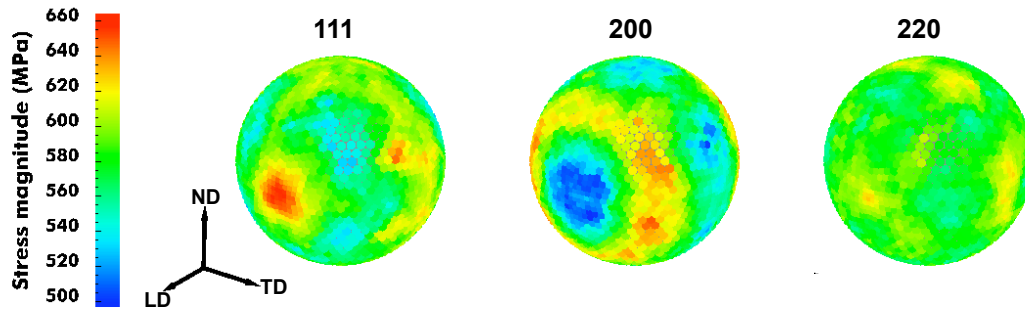
The simulations possess information such as the crystal stress states, the slip system shearing rates and the slip system strengths which currently cannot be measured in the experiments. The lattice strains and crystal orientation information in the simulations are also more highly resolved than in the experiments. In the simulations, the exact lattice orientation along a crystallographic fiber and the full elastic strain tensor of each crystal is known. However, in the SPF powder experiments the orientation of a diffracting crystal is known only to within a rotation about its scattering vector and only the average lattice strain among all crystals satisfying a particular Bragg condition can be measured.

In addition to generating SPFs from the simulation data to be compared to

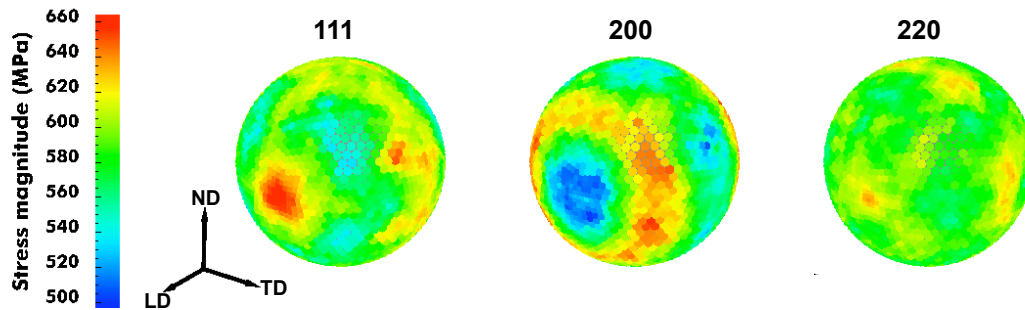
the measured SPFs, the crystal stresses which drive the evolution of the lattice strains can also be examined from the simulation data. Due to the symmetric nature of the crystal stress tensor, the crystal stresses can be cast into a 6-dimensional vector form. The magnitudes of the crystal stress vectors, which are averaged along a crystallographic fiber, are plotted on a pole figure in Figure 3.13. Since the crystal stress information for all crystals within the virtual specimen is readily available, the crystal stress magnitudes are plotted over the entire pole figure and since these simulation results cannot be compared to the experiments, the crystal quantities plotted in this section are not grouped into larger regions on the pole figure.

The magnitudes of the crystal stress vectors on Cycle 0 and Cycle 100 are plotted on the pole figure in Figures 3.13(a) and 3.13(b), respectively. The differences in the stress magnitudes between Cycle 100 and Cycle 0 are shown in Figure 3.13(c), where the Cycle 0 stress magnitudes are subtracted from the Cycle 100 stress magnitudes. The stress magnitudes on Cycle 0 and Cycle 100 exhibit very similar trends, although there is some change in the stress magnitudes on the order of approximately 10 MPa between Cycle 0 and Cycle 100.

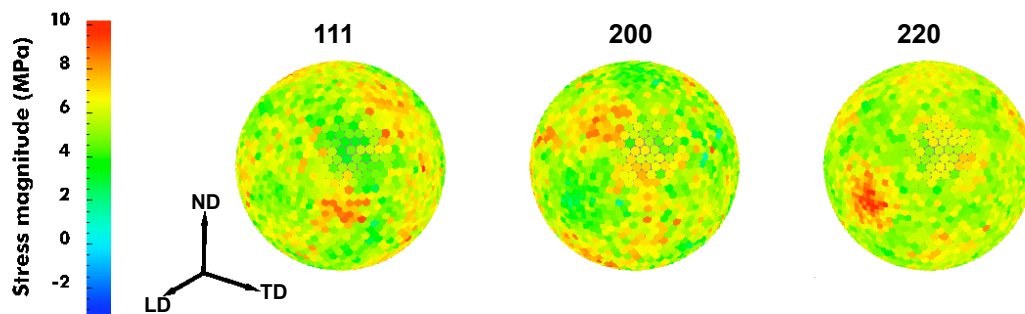
Examining the stress magnitudes on the  $\{111\}$  pole figure shown in Figures 3.13(a) and 3.13(b), the  $\{111\} \parallel$  LD stress magnitudes are the largest compared to other orientations on the pole figure. For the  $\{200\}$  pole figure, the  $\{200\} \parallel$  LD stress magnitudes are the smallest compared to other orientations on the pole figure. For the  $\{220\}$  pole figure, the  $\{220\} \parallel$  LD orientations have only slightly higher stress magnitudes relative to other orientations on the pole figure. The  $\{hkl\} \parallel$  LD notation refers to the  $\{hkl\} \parallel$  LD crystallographic fiber, which corresponds to the set of crystals with their  $\{hkl\}$  lattice plane normals aligned with the specimen loading direction (LD).



(a) Magnitudes of the crystal stress vectors on Cycle 0



(b) Magnitudes of the crystal stress vectors on Cycle 100



(c) Differences in the magnitudes of the crystal stress vectors between Cycle 100 and Cycle 0, where the values on Cycle 0 is subtracted from the values on Cycle 100.

Figure 3.13: Magnitudes of the crystals stress vectors computed from the simulations and plotted on pole figures. Note that the color-bar scale for Figure 3.13(c) is different.

We can also compare the stress magnitudes with the simulation SPFs on Cycle 0, by comparing Figure 3.8(b) and Figure 3.13(a). For a particular  $\{hkl\}$  family of lattice planes, the scattering vectors close to the LD direction exhibit the largest tensile lattice strain. However, the scattering vectors closest to the LD direction do not necessarily have the largest stress magnitudes. This can be attributed to the fact that since the crystal stresses are related to the crystal elastic strains through anisotropic Hooke's law, the lattice strains and the stress magnitudes will not exhibit a one-to-one correspondence in their values.

The specimen in the experiment and the virtual specimen in the simulations are both cycled out to approximately 3–4 % macroscopic strain as shown in Figure 3.6, indicating that significant plastic deformation has been achieved. Ritz et al. [2] have demonstrated that under monotonic tensile loading, the crystal stresses move towards the vertices of the single crystal yield surface (SCYS) in fully-developed plasticity. A vertex is the intersection of at least five planes of the SCYS and the vertex stress is the five dimensional deviatoric stress vector associated with the vertex. Although the fcc SCYS has 56 vertices (28 positive vertices), Ritz et al. have shown that these vertices can be grouped into five unique vertex families due to crystal symmetries, where the vertex stresses within a vertex family are indistinguishable from each other. Although the SCYS analysis conducted by Ritz et al. applied to monotonic tensile loading, the analysis is still relevant to our current study because the crystal stresses follow the same loading path to the yield surface upon reloading on each cycle [58].

The preferred vertex family for several crystallographic fibers and the relative magnitudes of the vertex stresses are shown in Table 3.3. The preferred vertex family of the  $\{111\} \parallel$  LD crystals is the V2 vertex family and the preferred vertex family of the  $\{200\} \parallel$  LD crystals is the V1 vertex family. Ritz et al.

have also shown that the  $\{111\} \parallel \text{LD}$  and  $\{200\} \parallel \text{LD}$  crystals are well-aligned with their preferred vertex stresses upon yielding and their preferred vertex families in fully-developed plasticity are aligned with the macroscopic stress. Although the  $\{220\} \parallel \text{LD}$  crystal stresses do have a preferred vertex family (V3), the crystal stresses are less well aligned with their preferred vertex stress family even at 3–4% macroscopic strain [2]. Comparing Figure 3.13 to Table 3.3, the relative values of the  $\{111\} \parallel \text{LD}$  and  $\{200\} \parallel \text{LD}$  stress magnitudes are consistent with the relative magnitudes of their preferred vertex stresses. The  $\{111\} \parallel \text{LD}$  stress magnitudes are larger than the  $\{200\} \parallel \text{LD}$  stress magnitudes, consistent with the relative magnitudes of the V2 and V1 vertex stresses which are 1.50 and 1.00, respectively. The  $\{220\} \parallel \text{LD}$  stress magnitudes, however, do not compare well to the relative magnitude of their preferred vertex stress possibly due to the fact that the  $\{220\} \parallel \text{LD}$  crystal stresses are not highly aligned with their preferred vertex stress at 3–4% macroscopic strain and require more plastic straining for the crystal stresses to move into a vertex [2].

Crystallographic fiber	Vertex family	Relative magnitude of $\sigma'_v$
$\{111\} \parallel \text{LD}$	V2	1.50
$\{200\} \parallel \text{LD}$	V1	1.00
$\{220\} \parallel \text{LD}$	V3	1.73

Table 3.3: Magnitude of the deviatoric form of the vertex stress,  $\sigma'_v$ , for each vertex stress family [2].

Although the stress magnitudes are plotted at a macroscopic stress level that is not on the yield surface, we found that the trends in the stress magnitudes at 90% of the target macroscopic stress mirrored the trends in the stress magnitudes at the target macroscopic stress on each cycle. Therefore, the SCYS analysis can still be used to explain the trends in the stress magnitudes shown in Figure 3.13.

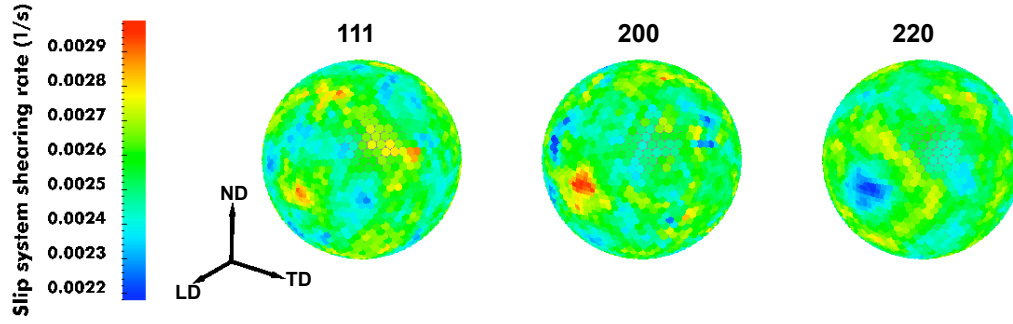
We can also examine the influence of the crystal stresses on the net slip system shearing rates, which are shown in Figure 3.14. The net slip system shearing rate for each element in the mesh,  $\dot{\gamma}$ , is computed as:

$$\dot{\gamma} = \sum_{\alpha} |\dot{\gamma}^{\alpha}| \quad (3.13)$$

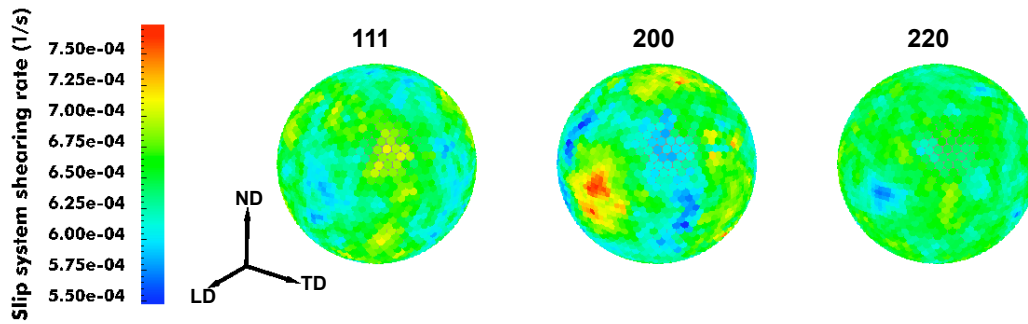
where  $\dot{\gamma}^{\alpha}$  is the slip system shearing rate for the  $\alpha$ -slip system, computed in Equation (3.7). The values of  $\dot{\gamma}$  are averaged along a crystallographic fiber and plotted on the pole figure in Figure 3.14. It is observed that the net slip system shearing rates on Cycle 100 are an order of magnitude smaller than the net slip system shearing rates on Cycle 0, therefore the differences of the net slip system shearing rates between Cycle 100 and Cycle 0 are not presented here. Since the specimen is cycled between fixed macroscopic stress limits, strain hardening occurring with increasing cycles causes less slip system activity on each cycle.

In general, orientations on the pole figure with relatively high stress magnitudes do not necessarily correspond to higher slip system activity. Comparing Figures 3.13(a)–3.13(b) to Figure 3.14, the  $\{111\} \parallel$  LD crystals on Cycle 100 have relatively high stress magnitudes but relatively low slip system activity whereas the  $\{200\} \parallel$  LD crystals have relatively low stress magnitudes but relatively high slip system activity on both Cycles 0 and 100. The slip system shearing rates result from the resolved shear stress on each slip system, which is projection of the crystal stress onto the slip plane in the slip direction for all of the slip systems. This implies that certain crystal orientations are more favorably orientated for slip system shearing than others and therefore it is possible that a lower crystal stress magnitude, depending on its direction, is able to produce higher resolved shear stresses and therefore result in more slip system activity.

The implication of the stress magnitudes and the slip system activity on the evolution of the slip system strengths is examined in Figure 3.15. The slip sys-



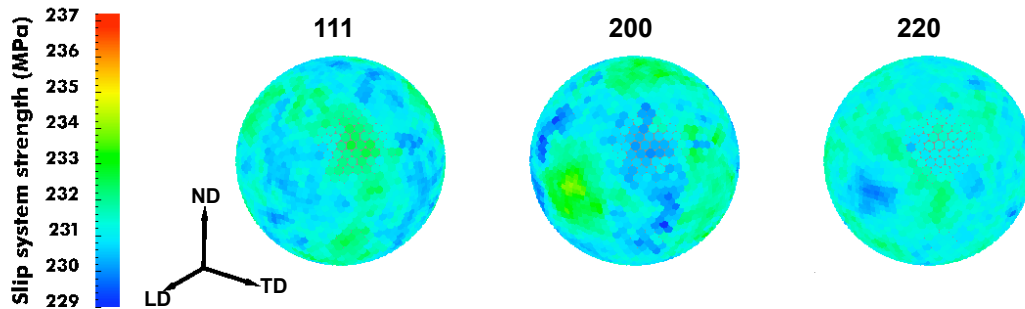
(a) Net slip system shearing rate on Cycle 0



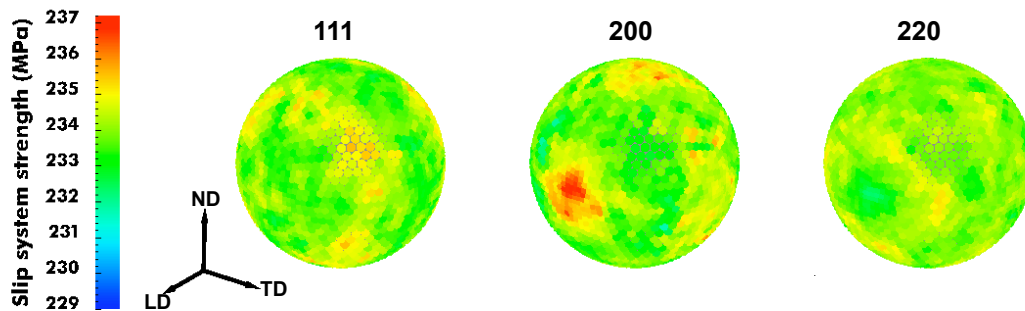
(b) Net slip system shearing rate on Cycle 100

Figure 3.14: Net slip system shearing rate,  $\dot{\gamma}$ , plotted over a pole figure for Cycles 0 and 100. Note that the colorbar scales are different.

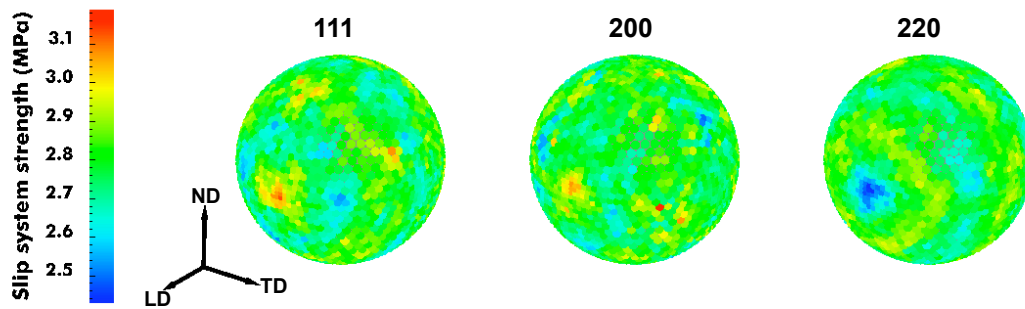
tem strengths increase with cycles for all orientations in general due to strain hardening although the slip system strengths for different orientations increase at different rates. Comparing Figure 3.14 to Figure 3.15, it appears that orientations with high slip system activity tend to correspond to orientations with relatively high slip system strength for a particular  $\{hkl\}$  pole figure. However, the  $\{111\} \parallel \text{LD}$  slip system activity on Cycle 0 is relatively higher compared to other scattering vectors on the  $\{111\}$  pole figure whereas the slip system strengths for the  $\{111\} \parallel \text{LD}$  crystals are relatively lower compared to other orientations on the  $\{111\}$  pole figure. This can be attributed to the fact that these quantities plotted on a pole figure are averaged along a crystallographic fiber and therefore have a significant number of crystals contributing to the average value which is



(a) Slip system strength on Cycle 0



(b) Slip system strength on Cycle 100



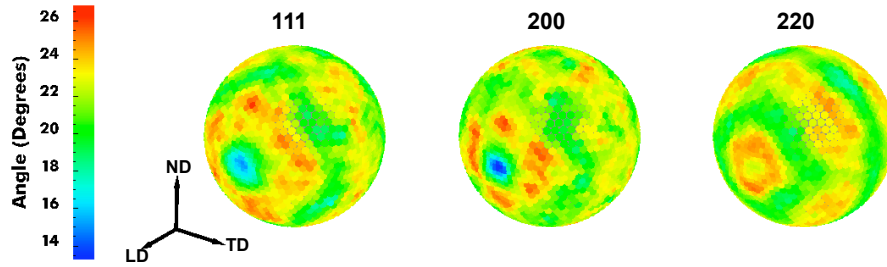
(c) Difference in slip system strengths between Cycle 100 and Cycle 0

Figure 3.15: Slip system strength computed from the simulations. Note that the scale for Figure 3.15(c) is different.

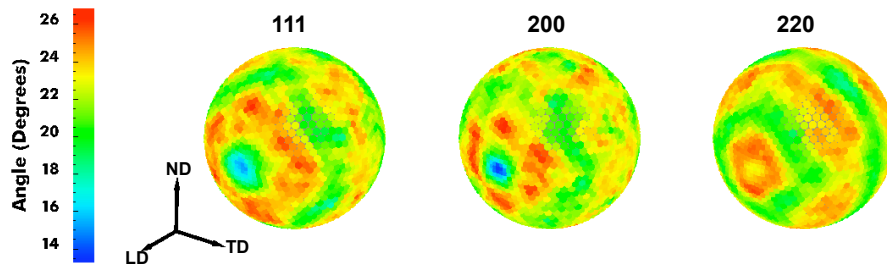
plotted on the pole figure. It is known that grain interactions between neighboring grains will influence the crystal stress state and therefore influence the slip system shearing rates and slip system strengths among the crystals belonging to a crystallographic fiber.

In Figure 3.13(c), the  $\{220\} \parallel$  LD stress magnitudes increase relatively more with increasing cycles compared to other fibers on the  $\{220\}$  pole figure. However, in Figure 3.15(c) the  $\{220\} \parallel$  LD slip systems strengths increase relatively less with increasing cycles compared to other fibers on the  $\{220\}$  pole figure. This phenomena can be attributed to the fact that even though the  $\{220\} \parallel$  LD stress magnitudes increase relatively more with cycles, these crystals are less well oriented to cause slip system activity and slip system hardening. The preferred vertex stresses for the  $\{220\} \parallel$  LD crystals are also relatively farther away from the center of stress space compared to the preferred vertex stresses of the  $\{111\} \parallel$  LD and  $\{200\} \parallel$  LD crystals, as shown in Table 3.3. Even though the  $\{220\} \parallel$  LD stress magnitudes increase relatively more with cycles, they are not increasing enough to cause relatively more strain hardening.

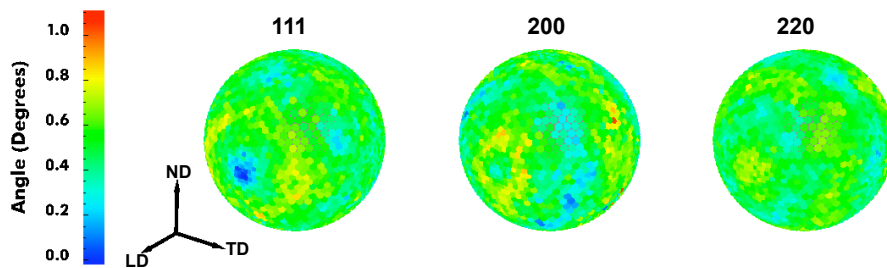
The angles between the crystal stress vectors and the vector form of the macroscopic stress are shown in Figure 3.16. It is observed that the  $\{111\} \parallel$  LD and  $\{200\} \parallel$  LD crystal stress vectors are more closely aligned with the macroscopic stress compared to other crystallographic fibers while the  $\{220\} \parallel$  LD crystal stresses are less well-aligned with the macroscopic stress. Since the  $\{111\} \parallel$  LD and  $\{200\} \parallel$  LD crystal stresses align with their respective preferred vertex stresses very early in the deformation [2], the stresses associated with these fibers will also have the smallest angle with the macroscopic stress, as shown in Figures 3.16(a) and 3.16(b). There is very little change in the angle between the crystal stress and the macroscopic stress after 100 cycles. In fact, they align



(a) Angle between macroscopic stress and crystal stress on Cycle 0



(b) Angle between macroscopic stress and crystal stress on Cycle 100



(c) Difference of angle between macroscopic stress and crystal stress between Cycle 100 and Cycle 0

Figure 3.16: Angle between macroscopic stress and crystal stress computed from the simulations. Note that the scale for Figure 3.16(c) is different.

more closely with the macroscopic stress with increasing cycles. The preferred vertex stresses of the  $\{220\} \parallel$  LD crystals however, are not highly aligned with the macroscopic stress. With increasing cycles and increasing plastic deformation, the  $\{220\} \parallel$  LD crystal stresses move toward their preferred vertices and away from the macroscopic stress, therefore the angle between the crystal stress and the macroscopic stress increases, as shown in Figure 3.16(c).

### 3.7 Discussion

An important observation from the experiment and simulation SPFs presented in Section 3.6 is that there is a clear dependence of the lattice strains on crystallographic orientation. The difference SPFs shown in Figures 3.10–3.12 demonstrate that the lattice strains in both the experiment and simulation evolve with cycles, although they evolve at different rates at various points in the loading history.

The  $\{111\}$  and  $\{220\}$  SPFs in Figures 3.8 and 3.9 show reasonable agreement in terms of the evolution of the lattice strains, where the lattice strains in the LD direction increase with cycles while the lattice strains in the TD direction decrease with cycles. The  $\{200\}$  SPFs, however, do not evolve in similar directions between the experiments and simulations. The crystals associated with the  $\{200\}$  SPF have the largest residual lattice strain distribution prior to loading, as shown in Figure 3.7 and they also have the largest difference between the experiment and simulation SPFs shown in Figures 3.8 and 3.9.

The crystals in the virtual specimen were not assigned residual stress states, which influences the determination of the single crystal elastic anisotropy of the material. Since the single crystal elastic moduli influences the crystal stress

state, any inaccuracy in the determination of the single crystal elastic moduli will in turn influence the evolution of the crystal stresses during cyclic loading. However, the procedure for assigning a residual stress state to each crystal in the virtual specimen from measured residual lattice strain distributions is a non-trivial problem. As a first step, a suite of simulations can be conducted by imposing different types of deformation conditions on the virtual polycrystal prior to cyclic loading to investigate the effect of different residual stress distributions on the evolution of the lattice strains during cyclic loading.

The crystal stress magnitudes and lattice strains do not have a one-to-one correspondence due to the anisotropic elastic relationship between the crystal stresses and elastic strains. Therefore, it is necessary to use the simulations to examine the crystal stresses as part of building a more complete understanding of the micromechanical state in these crystals under cyclic loading. The simulations can be used to examine the evolution of various crystal quantities such as the magnitude and direction of the stress, the slip system activity and the slip system strengths which cannot be measured in the experiments. The trends in the crystal stresses were found to be consistent with the trends in the slip system activity and the slip system strengths when examined with respect to the vertices of the single crystal yield surface.

The current study is not intended to be a comprehensive description of the evolution of the micromechanical state in polycrystalline aggregates under *in situ* cyclic loading, but rather a first attempt at conducting a coordinated program of experiments and simulations to investigate the evolving stress distribution in polycrystals. Neither the simulations nor the experiments are used to validate the other, but rather they are used in a complementary manner to build a more complete picture of the evolution of the micromechanical state of

the polycrystal. Using the currently available experimental and computational tools, a framework has been developed to quantify the evolution of the lattice strains during *in situ* loading. This framework has the potential for additional sophistication to more accurately characterize the microstructure of the material and the stress/strain distribution of the crystals within the polycrystalline aggregate.

### 3.8 Conclusions

- The lattice strains, in both the experiments and simulations, exhibit a clear dependence on crystallographic orientation. The evolution of these lattice strains with cycles exhibit an orientation dependent response as well.
- In both the experiment and simulation SPFs for all  $\{hkl\}$  pole figures under investigation, the lattice strains are tensile in the loading direction (LD) and compressive in the transverse direction (TD), which is consistent with the Poisson effect.
- The largest difference between the experiment and simulation SPFs occurs for the  $\{200\}$  SPF, which also has the largest measured residual lattice strains.
- For the measured  $\{111\}$  and  $\{220\}$  SPFs, the lattice strains close to the LD direction increase with cycles and the lattice strains close to the TD direction decrease with cycles. However, for the measured  $\{200\}$  SPF, the lattice strains close to the LD direction decrease with cycles and the lattice strains close to the TD direction increase with cycles.
- The trends in the evolution of the computed  $\{111\}$  and  $\{220\}$  SPFs with increasing cycles are consistent with the measured  $\{111\}$  and  $\{220\}$  SPFs

but there is less agreement between the experiment and simulation for the  $\{200\}$  SPF in terms of the direction of evolution with increasing cycles, particularly for the lattice strains close to the LD and TD directions. The differences in the lattice strains between Cycles 0 and 100 are on the same order of magnitude in the experiments and simulations.

- In the simulations, orientations on the pole figure with relatively large lattice strains do not necessarily correspond to relatively high crystal stress magnitudes because the crystal stresses and strains are related through anisotropic Hooke's law.
- Even though the stress magnitudes for a particular fiber increase relatively more with cycles compared to other fibers, the slip system strengths associated with that fiber can exhibit relatively less increase with cycles compared to other fibers. Possible reasons for this are that the crystal stresses are less favorably oriented for slip system activity and consequently less strain hardening occurs or that the preferred vertex is relatively farther away from the origin of stress space.
- The  $\{111\} \parallel \text{LD}$  and  $\{200\} \parallel \text{LD}$  crystal stresses align with their preferred vertex stresses as soon as yielding occurs and their relative stress magnitudes on the pole figure correlate well with the relative magnitudes of their preferred vertex stresses. The  $\{220\} \parallel \text{LD}$  stresses are not as well aligned with their preferred vertex stress, even at 3–4% macroscopic strain.
- The angle between the  $\{111\} \parallel \text{LD}$  and  $\{200\} \parallel \text{LD}$  crystal stresses and the macroscopic tends to decrease with cycles whereas the angle between the  $\{220\} \parallel \text{LD}$  crystal stresses and the macroscopic tends to increase with cycles. The preferred vertex families of the  $\{111\} \parallel \text{LD}$  and  $\{200\} \parallel \text{LD}$  crystals are aligned with the macroscopic stress and therefore the crystal

stresses move into a vertex with increasing plastic straining. The preferred vertex family of the  $\{220\}$  || LD crystals however, is not aligned with the macroscopic stress and therefore with increasing plastic deformation the  $\{220\}$  || LD crystal stresses tend to move into a vertex and away from the macroscopic stress.

## CHAPTER 4

### SUMMARY AND FINDINGS

The deviations of the lattice strains as a function of macroscopic stress from linear behavior in the elastic-plastic transition regime have long been observed experimentally in polycrystals under monotonic tensile loading. By conducting a single crystal elastic anisotropy parametric study using a crystal-based finite element model, the combined influence of the single crystal elastic and plastic anisotropy on the lattice strain behaviors in fcc polycrystals can be examined. The combination of the single crystal elastic and plastic anisotropy is quantified using the directional strength-to-stiffness ratio, which provides a means of explaining the observed lattice strain behaviors in a consistent manner. The different lattice strain behaviors in the elastic-plastic transition regime, which result from different values of the directional strength-to-stiffness ratio, can also be used to determine the single crystal elastic anisotropy of a material, if it is unknown.

The concepts of the directional strength-to-stiffness ratio and the vertices of the single crystal yield surface, which were previously applied to fcc polycrystals under monotonic tensile loading, have also been extended to examine the lattice strains response under fully-reversed cyclic loading. Although only a qualitative comparison was made with previously published lattice strain data, the lattice strains computed in the finite element simulations showed good qualitative agreement with measured lattice strains in stainless steel. By examining the computed lattice strains for isotropic crystals and crystals with high single crystal elastic anisotropy, it was found that the directional strength-to-stiffness ratio and the residual stress distribution due to cyclic loading influences the progression of yielding on each cycle. In fully-developed plasticity, however,

the crystal stresses are determined by the vertices of the single crystal yield surface. Although the crystal stresses are determined by the vertex stresses, the lattice strains, which are related to the crystal stresses through Hooke's law, are also influenced by the elastic anisotropy in fully-developed plasticity. Additional simulations were also conducted to examine the influence of texture and cyclic hardening on the progression of yielding of the crystals through the elastic-plastic transition and on the shape of lattice strain hysteresis loops during cyclic loading. It was found that the texture and cyclic hardening do not significantly influence the results presented.

A coordinated approach using crystal-based finite element simulations and high-energy synchrotron diffraction experiments has been conducted to quantify the evolution of the lattice strains in an AA7075-T6 aluminum alloy under *in situ* cyclic loading. Lattice Strain Pole Figures (SPFs) are compared between the experiments and simulations at the same macroscopic stress level on several cycles in the loading history. This lattice strain comparison represents the first time a quantitative comparison has been made to quantify and track the evolution of the micromechanical response of polycrystals under *in situ* cyclic loading using our most current experimental and numerical tools. Orientation dependent evolution in both the measured and computed lattice strains can be observed from the SPFs. By examining the crystal stresses available in the simulation data, we observe that the crystallographic fibers with the largest stress magnitudes do not correspond to the crystallographic fibers with the largest lattice strains due to the anisotropic nature of the single crystal elastic moduli relating the crystal stresses to the crystal strains. We also examine trends in the evolution of the slip system strengths, the net slip system shearing rates and the angle between the crystal stresses and the macroscopic stress. The vertices of

the single crystal yield surface can be used to explain the trends in the evolution of these quantities from a consistent, micromechanical point of view.

## APPENDIX A

### APPROACH FOR VARYING SINGLE CRYSTAL ELASTIC MODULI

The approach used for varying the single crystal elastic moduli follows the approach used by Dawson et. al. [3]. The elastic strain tensor,  $\epsilon$ , can be decomposed into its off-diagonal, deviatoric diagonal and spherical parts,  $\epsilon_{\text{off}}$ ,  $\epsilon_{\text{ddg}}$  and  $\epsilon_{\text{sph}}$  respectively:

$$\begin{bmatrix} \epsilon_{11} & \epsilon_{12} & \epsilon_{13} \\ \epsilon_{12} & \epsilon_{22} & \epsilon_{23} \\ \epsilon_{13} & \epsilon_{23} & \epsilon_{33} \end{bmatrix} = \begin{bmatrix} 0 & \epsilon_{12} & \epsilon_{13} \\ \epsilon_{12} & 0 & \epsilon_{23} \\ \epsilon_{13} & \epsilon_{23} & 0 \end{bmatrix} + \begin{bmatrix} \epsilon_{11} - \epsilon_m & 0 & 0 \\ 0 & \epsilon_{22} - \epsilon_m & 0 \\ 0 & 0 & \epsilon_{33} - \epsilon_m \end{bmatrix} + \begin{bmatrix} \epsilon_m & 0 & 0 \\ 0 & \epsilon_m & 0 \\ 0 & 0 & \epsilon_m \end{bmatrix} \quad (\text{A.1})$$

where  $\epsilon_m = \frac{1}{3}\text{trace}(\epsilon)$ .

In the crystal coordinate system, the elastic strain can related to the Kirchoff stress tensor,  $\tau$ , through scaling coefficients:

$$\tau = C_{\text{off}}\epsilon_{\text{off}} + C_{\text{ddg}}\epsilon_{\text{ddg}} + C_{\text{sph}}\epsilon_{\text{sph}} \quad (\text{A.2})$$

The scaling coefficients  $C_{\text{off}}$ ,  $C_{\text{ddg}}$  and  $C_{\text{sph}}$  are related to the single crystal elastic moduli for a cubic crystal:

$$C_{\text{off}} = C_{44}$$

$$C_{\text{ddg}} = C_{11} - C_{12}$$

$$C_{\text{sph}} = C_{11} + 2C_{12}$$

Three independent parameters are required to describe the single crystal anisotropic behavior of a crystal. The three parameters that are chosen are the single crystal elastic anisotropy ratio ( $r_E$ ), an average Young's modulus ( $E_{\text{avg}}$ ) and an average Poisson's ratio ( $\nu_{\text{avg}}$ ). The average parameters  $E_{\text{avg}}$  and  $\nu_{\text{avg}}$

are based on the average response of a polycrystalline aggregate composed of anisotropic single crystals with uniformly distributed lattice orientations which results in an isotropic elastic response on the macroscopic scale. Our approach to varying the level of single crystal elastic anisotropy is to keep  $E_{\text{avg}}$  and  $\nu_{\text{avg}}$  constant, while varying  $r_E$ .

A simple relationship can be established between the single crystal elastic moduli and the average parameters  $E_{\text{avg}}$  and  $\nu_{\text{avg}}$  for a polycrystalline aggregate with uniform texture. Recall that Hooke's law for an isotropic material (or an elastically isotropic aggregate) is written as:

$$\boldsymbol{\tau} = 3K_{\text{avg}} \left( \frac{1}{3} \text{trace}(\boldsymbol{\epsilon}) \cdot \mathbf{I} \right) + 2G_{\text{avg}} \left( \boldsymbol{\epsilon} - \frac{1}{3} \text{trace}(\boldsymbol{\epsilon}) \cdot \mathbf{I} \right) \quad (\text{A.3})$$

where  $\mathbf{I}$  is the identity tensor,  $K_{\text{avg}}$  is the average bulk modulus and  $G_{\text{avg}}$  is the average shear modulus. Since the volumetric behavior of the single crystal is inherently isotropic, the single crystal elastic moduli can be related to the average isotropic parameters:

$$3K_{\text{avg}} = C_{\text{sph}} \quad (\text{A.4})$$

The shear behavior of the single crystal is represented by the scaling coefficients  $C_{\text{off}}$  and  $C_{\text{ddg}}$  in Equation (A.2). The single crystal shear behavior is related to the average shear behavior using a crude average of the  $C_{\text{off}}$  and  $C_{\text{ddg}}$  coefficients, by assuming that the aggregate is elastically isotropic due to uniform texture:

$$2G_{\text{avg}} = \frac{1}{2}(C_{\text{off}} + C_{\text{ddg}}) \quad (\text{A.5})$$

The average Young's modulus,  $E_{\text{avg}}$ , and average Poisson's ratio,  $\nu_{\text{avg}}$ , can be written in terms of  $K_{\text{avg}}$  and  $G_{\text{avg}}$ :

$$E_{\text{avg}} = \frac{9K_{\text{avg}}G_{\text{avg}}}{3K_{\text{avg}} + G_{\text{avg}}} \quad (\text{A.6})$$

$$\nu_{\text{avg}} = \frac{3K_{\text{avg}} - 2G_{\text{avg}}}{2(3K_{\text{avg}} + G_{\text{avg}})} \quad (\text{A.7})$$

$r_E$  is computed from the single crystal elastic moduli as:

$$r_E = \frac{1 + 2C_{\text{sph}}/C_{\text{ddg}}}{1 + 2C_{\text{sph}}/C_{\text{off}}} \quad (\text{A.8})$$

Equations (A.6)–(A.8) can be solved simultaneously for the single crystal elastic moduli.

## APPENDIX B

### DERIVATION OF SINGLE CRYSTAL DIRECTIONAL STIFFNESS

The Kirchhoff stress tensor in the  $d\hat{2}\hat{3}$  coordinate system is given as:

$$\tau_{d\hat{2}\hat{3}} = \begin{bmatrix} \tau_d & 0 & 0 \\ 0 & 0 & 0 \\ 0 & 0 & 0 \end{bmatrix} \quad (\text{B.1})$$

The stress tensor in the  $d\hat{2}\hat{3}$  coordinate system is rotated to the 123 coordinate system because the single crystal elastic constants are defined in the 123 coordinate system. The rotation matrix,  $\mathbf{A}$ , that rotates the 123 axes to the  $d\hat{2}\hat{3}$  axes is defined as follows:

$$\mathbf{A}(\theta, \phi) = \begin{bmatrix} \cos \phi & 0 & \sin \phi \\ 0 & 1 & 0 \\ -\sin \phi & 0 & \cos \phi \end{bmatrix} \begin{bmatrix} \cos \theta & \sin \theta & 0 \\ -\sin \theta & \cos \theta & 0 \\ 0 & 0 & 1 \end{bmatrix} \quad (\text{B.2})$$

The stress tensor in the  $d\hat{2}\hat{3}$  coordinate system,  $\tau_{d\hat{2}\hat{3}}$ , then is rotated to the 123 coordinate system:

$$[\tau_{123}] = [\mathbf{A}]^T [\tau_{d\hat{2}\hat{3}}] [\mathbf{A}] \quad (\text{B.3})$$

where  $\tau_{123}$  is the stress tensor in the 123 coordinate system.

The elastic strains in the 123 coordinate system are computed using Voigt notation with the inverse of Equation (1.7):

$$\begin{Bmatrix} \epsilon_{11} \\ \epsilon_{22} \\ \epsilon_{33} \\ \epsilon_{23} \\ \epsilon_{13} \\ \epsilon_{12} \end{Bmatrix} = \begin{bmatrix} C_{11} & C_{12} & C_{12} & 0 & 0 & 0 \\ C_{12} & C_{11} & C_{12} & 0 & 0 & 0 \\ C_{12} & C_{12} & C_{11} & 0 & 0 & 0 \\ 0 & 0 & 0 & C_{44} & 0 & 0 \\ 0 & 0 & 0 & 0 & C_{44} & 0 \\ 0 & 0 & 0 & 0 & 0 & C_{44} \end{bmatrix}^{-1} \begin{Bmatrix} \tau_{11} \\ \tau_{22} \\ \tau_{33} \\ \tau_{23} \\ \tau_{13} \\ \tau_{12} \end{Bmatrix} \quad (\text{B.4})$$

The elastic strains in the 123 coordinate system is put into matrix form:

$$\boldsymbol{\epsilon}_{123} = \begin{bmatrix} \epsilon_{11} & \epsilon_{12} & \epsilon_{13} \\ \epsilon_{12} & \epsilon_{22} & \epsilon_{23} \\ \epsilon_{13} & \epsilon_{23} & \epsilon_{33} \end{bmatrix} \quad (\text{B.5})$$

The strain tensor in the 123 coordinate system,  $\boldsymbol{\epsilon}_{123}$ , is then rotated back to the  $d\hat{2}\hat{3}$  coordinate system:

$$[\boldsymbol{\epsilon}_{d\hat{2}\hat{3}}] = [\mathbf{A}][\boldsymbol{\epsilon}_{123}][\mathbf{A}]^T \quad (\text{B.6})$$

The strain tensor in the  $d\hat{2}\hat{3}$  coordinate system has the form:

$$\boldsymbol{\epsilon}_{d\hat{2}\hat{3}} = \begin{bmatrix} \epsilon_d & \epsilon_{12}^d & \epsilon_{13}^d \\ \epsilon_{12}^d & \epsilon_{22}^d & \epsilon_{23}^d \\ \epsilon_{13}^d & \epsilon_{23}^d & \epsilon_{33}^d \end{bmatrix} \quad (\text{B.7})$$

The definition of the directional elastic stiffness for a single crystal,  $E_d^{\text{crys}}$ , is the ratio of the Kirchhoff stress component in the  $d$  direction,  $\tau_d$ , to the strain component in the  $d$  direction,  $\epsilon_d$ :

$$E_d^{\text{crys}} = \frac{\tau_d}{\epsilon_d} \quad (\text{B.8})$$

## BIBLIOGRAPHY

- [1] S. L. Wong and P. R. Dawson. Influence of directional strength-to-stiffness on the elastic-plastic transition of fcc polycrystals under uniaxial tensile loading. *Acta Materialia*, 58(5):1658 – 1678, 2010.
- [2] H. Ritz, P. R. Dawson, and T. Marin. Analyzing the orientation dependence of stresses in polycrystals using vertices of the single crystal yield surface and crystallographic fibers of orientation space. *Journal of the Mechanics and Physics of Solids*, 58(1):54 – 72, 2010.
- [3] P. R. Dawson, D. E. Boyce, S. R. MacEwen, and R. B. Rogge. On the influence of crystal elastic moduli on computed lattice strains in AA-5182 following plastic straining. *Materials Science and Engineering A*, 313(1-2):123–144, 2001.
- [4] I. C. Noyan and J. B. Cohen. *Residual Stress: Measurement by Diffraction and Interpretation*. Springer-Verlag, 1987.
- [5] A. D. Krawitz. *Introduction to Diffraction in Materials Science and Engineering*. Wiley-Interscience, New York, 2001.
- [6] A. Wanner and D. C. Dunand. Synchrotron x-ray study of bulk lattice strains in externally loaded Cu-Mo composites. *Metallurgical and Materials Transactions A*, 31(11):2949–2962, 2000.
- [7] M. P. Miller, J. V. Bernier, J.-S. Park, and A. Kazimirov. Experimental measurement of lattice strain pole figures using synchrotron x rays. *Review of Scientific Instruments*, 76:113903, 2005.

- [8] D. H. Carter and M. A. M. Bourke. Neutron diffraction study of the deformation behavior of beryllium–aluminum composites. *Acta Materialia*, 48(11):2885–2900, 2000.
- [9] Y. D. Wang, R. L. Peng, and R. L. McGreevy. A novel method for constructing the mean field of grain-orientation-dependent residual stress. *Philosophical Magazine Letters*, 81(3):153–163, 2001.
- [10] J. V. Bernier and M. P. Miller. A direct method for the determination of the mean orientation-dependent elastic strains and stresses in polycrystalline materials from strain pole figures. *Journal of Applied Crystallography*, 39:358–368, 2006.
- [11] T. M. Holden, A. P. Clarke, and R. A. Holt. Neutron diffraction measurements of intergranular strains in MONEL-400. *Metallurgical and Materials Transactions A*, 28A:2565 – 2576, 1997.
- [12] T. M. Holden, R. A. Holt, and A. P. Clarke. Intergranular strains in Incoloy-800. *Journal of Neutron Research*, 4:241–264, 1997.
- [13] T. M. Holden, R. A. Holt, and A. P. Clarke. Intergranular strains in Inconel-600 and the impact on interpreting stress fields in bent steam-generator tubing. *Materials Science and Engineering A*, A246:180–198, 1998.
- [14] B. Clausen, T. Lorentzen, M. A. M. Bourke, and M. R. Daymond. Lattice strain evolution during uniaxial tensile loading of stainless steel. *Materials Science and Engineering A*, 259(1):17–24, 1999.
- [15] B. Clausen and M. Bourke. Lattice plane response during tensile loading of an aluminum 2 percent magnesium alloy. *Metallurgical and Materials Transactions A*, 32(13):691–694, 2001.

- [16] J. W. L. Pang, T. M. Holden, and T. E. Mason. In situ generation of intergranular strains in an Al7050 alloy. *Acta Materialia*, 46(5):1503–1518, 1998.
- [17] J. W. L. Pang, T. M. Holden, J. S. Wright, and T. E. Mason. The generation of intergranular strains in 309H stainless steel under uniaxial loading. *Acta Materialia*, 48:1131–1140, 2000.
- [18] M. R. Daymond, C. N. Tomé, and M. A. M. Bourke. Measured and predicted intergranular strains in textured austenitic steel. *Acta Materialia*, 48(2):553–564, 2000.
- [19] J. W. L. Pang, T. M. Holden, and T. E. Mason. The development of intergranular strains in a high-strength steel. *Journal of Strain Analysis*, 33(5):373–383, 1998.
- [20] M. R. Daymond and H. G. Priesmeyer. Elastoplastic deformation of ferritic steel and cementite studied by neutron diffraction and self-consistent modelling. *Acta Materialia*, 50:1613–1626, 2002.
- [21] E. C. Oliver, M. R. Daymond, and P. J. Withers. Interphase and intergranular stress generation in carbon steels. *Acta Materialia*, 52:1937–1951, 2004.
- [22] J. Quinta da Fonseca, E. C. Oliver, P. S. Bate, and P. J. Withers. Evolution of intergranular stresses during in situ straining of IF steel with different grain sizes. *Materials Science and Engineering A*, A437:26–32, 2006.
- [23] J. W. L. Pang, T. M. Holden, P. A. Turner, and T. E. Mason. Intergranular stresses in Zircaloy-2 with rod texture. *Acta Materialia*, 47(2):373–383, 1999.
- [24] D. W. Brown, M. A. M. Bourke, B. Clausen, T. M. Holden, C. N. Tomé, and R. Varma. A neutron diffraction and modeling study of uniaxial deforma-

- tion in polycrystalline beryllium. *Metallurgical and Materials Transactions A*, 34A:1439–1449, July 2003.
- [25] M. R. Daymond and N. W. Bonner. Lattice strain evolution in IMI 834 under applied stress. *Materials Science and Engineering A*, A340:272–280, 2003.
- [26] S. R. Agnew, C. N. Tomé, D. W. Brown, T. M. Holden, and S. C. Vogel. Study of slip mechanisms in a magnesium alloy by neutron diffraction and modeling. *Scripta Materialia*, 48:1003–1008, 2003.
- [27] S. R. Agnew, D. W. Brown, and C. N. Tomé. Validating a polycrystal model for the elastoplastic response of magnesium alloy AZ31 using in situ neutron diffraction. *Acta Materialia*, 54:4841–4852, 2006.
- [28] F. Xu, R. A. Holt, and M. R. Daymond. Modeling lattice strain evolution during uniaxial deformation of textured Zircaloy-2. *Acta Materialia*, 56:3672–3687, 2008.
- [29] B. Clausen, T. Lorentzen, and T. Leffers. Self-consistent modelling of the plastic deformation of f.c.c. polycrystals and its implications for diffraction measurements of internal stresses. *Acta Materialia*, 46(9):3087–3098, 1998.
- [30] F. C. Frank. Orientation mapping. *Metallurgical Transactions A*, 19(3):403–408, 1988.
- [31] A. Morawiec and D. P. Field. Rodrigues parameterization for orientation and misorientation distributions. *Philosophical Magazine A*, 73(4):1113–1130, 1996.
- [32] A. Kumar and P. R. Dawson. Computational modeling of f.c.c. deformation textures over Rodrigues' space. *Acta Materialia*, 48(10):2719–2736, 2000.

- [33] J. F. Nye. *Physical Properties of Crystals: Their Representation by Tensors and Matrices*. Oxford University Press, 1985.
- [34] W. F. Hosford. *The Mechanics of Crystals and Textured Polycrystals*. Oxford Science Publications, 1993.
- [35] E. B. Marin and P. R. Dawson. On modelling the elasto-viscoplastic response of metals using polycrystal plasticity. *Computer Methods in Applied Mechanics and Engineering*, 165(1-4):1–21, 1998.
- [36] E. B. Marin and P. R. Dawson. Elastoplastic finite element analyses of metal deformations using polycrystal constitutive models. *Computer Methods in Applied Mechanics and Engineering*, 165(1-4):23–41, 1998.
- [37] P. R. Dawson, D. E. Boyce, and R. B. Rogge. Issues in modeling heterogeneous deformations in polycrystalline metals using multiscale approaches. *CMES*, 10(2):123–141, 2005.
- [38] U. F. Kocks. The relation between polycrystal deformation and single-crystal deformation. *Metallurgical Transactions*, 1:1121–1143, 1970.
- [39] U. F. Kocks, G. R. Canova, and J. J. Jonas. Yield vectors in f.c.c. crystals. *Acta Metallurgica*, 31(8):1243–1252, 1983.
- [40] E. Schmid and W. Boas. *Plasticity of crystals with special reference to metals*. CRC Press, 1968.
- [41] H. J. Frost and M. F. Ashby. *Deformation-Mechanism Maps: The Plasticity and Creep of Metals and Ceramics*. Pergamon, 1982.
- [42] U. F. Kocks. Polyslip in single crystals. *Acta Metallurgica*, 8(6):345–352, 1960.

- [43] Y. D. Wang, H. Tian, A. D. Stoica, X.-L. Wang, P. K. Liaw, and J. W. Richardson. The development of grain-orientation-dependent residual stresses in a cyclically deformed alloy. *Nature Materials*, 2:101–106, 2003.
- [44] X.-L. Wang, Y. D. Wang, A. D. Stoica, D. J. Horton, H. Tian, P. K. Liaw, H. Choo, J. W. Richardson, and E. Maxey. Inter- and intragranular stresses in cyclically-deformed 316 stainless steel. *Materials Science and Engineering A*, 399:114–119, 2005.
- [45] J.-S. Park, P. Revesz, A. Kazimirov, and M. P. Miller. A methodology for measuring in situ lattice strain of bulk polycrystalline material under cyclic load. *Review of Scientific Instruments*, 78(2):023910, 2007.
- [46] T. Lorentzen, M. R. Daymond, B. Clausen, and C. N. Tomé. Lattice strain evolution during cyclic tensile loading of stainless steel. *Acta Materialia*, 50:1627–1638, 2002.
- [47] A. M. Korsunsky, K. E. James, and M. R. Daymond. Intergranular stresses in polycrystalline fatigue: diffraction measurement and self-consistent modelling. *Engineering Fracture Mechanics*, 71:805–812, 2004.
- [48] E.-W. Huang, B. Clausen, Y. D. Wang, H. Choo, P. K. Liaw, M. L. Benson, L. M. Pike, and D. L. Klarstrom. A neutron-diffraction study of the low-cycle fatigue behavior of HASTELLOY<sup>®</sup> C-22HS<sup>™</sup> alloy. *International Journal of Fatigue*, 29(9-11):1812–1819, 2007.
- [49] E.-W. Huang, R. I. Barabash, Y. D. Wang, B. Clausen, L. Li, P. K. Liaw, G. E. Ice, Y. Ren, H. Choo, L. M. Pike, and D. L. Klarstrom. Plastic behavior of a nickel-based alloy under monotonic-tension and low-cycle-fatigue loading. *International Journal of Plasticity*, 24(8):1440–1456, 2008.

- [50] T.-S. Han and P. R. Dawson. A two-scale deformation model for polycrystalline solids using a strongly-coupled finite element methodology. *Computer Methods in Applied Mechanics and Engineering*, 196(13-16):2029–2043, 2007.
- [51] E. Voce. The relationship between stress and strain for homogeneous deformation. *Journal of the Institute of Metals*, 74:537–562, 1948.
- [52] H. S. Turkmen, M. P. Miller, P. R. Dawson, and J. C. Moosbrugger. A slip-based model for strength evolution during cyclic loading. *Journal of Engineering Materials and Technology*, 126:329–338, 2004.
- [53] M. P. Miller, J.-S. Park, P. R. Dawson, and T.-S. Han. Measuring and modeling distributions of stress state in deforming measuring and modeling distributions of stress state in deforming polycrystals. *Acta Materialia*, 56:3927–3939, 2008.
- [54] D. P. Mika and P. R. Dawson. Effects of grain interaction on deformation in polycrystals. *Materials Science and Engineering: A*, 257(1):62 – 76, 1998.
- [55] H. M. Ledbetter. In M. Levy, H. E. Bass, and R. R. Stern, editors, *Handbook of Elastic Properties of Solids, Liquids, Gases*, volume III, pages 291–298; 313–324. Academic, 2000.
- [56] S. J. Czyzak, N. Bow, and H. Payne. On the tensile stress-strain relation and the baushinger effect for polycrystalline materials from taylor’s model. *Journal of the Mechanics and Physics of Solids*, 9(1):63 – 66, 1961.
- [57] J. W. Hutchinson. Plastic stress-strain relations of F.C.C polycrystalline metals hardening according to Taylor’s rule. *Journal of the Mechanics and Physics of Solids*, 12(1):11 – 24, 1964.

- [58] N. R. Barton, P. R. Dawson, and M. P. Miller. Yield strength asymmetry predictions from polycrystal elastoplasticity. *Transactions of the ASME*, 121:230–239, 1999.
- [59] N. E. Frost, K. J. Marsh, and L. P. Pook. *Metal Fatigue*. Dover, 1999.
- [60] R. I. Stephens, A. Fatemi, R. R. Stephens, and H. O. Fuchs. *Metal Fatigue in Engineering*. Wiley-Interscience, 2000.
- [61] R. Dingreville, C. C. Battaile, L. N. Brewer, E. A. Holm, and B. L. Boyce. The effect of microstructural representation on simulations of microplastic ratcheting. *International Journal of Plasticity*, 26(5):617 – 633, 2010.
- [62] J. V. Bernier and M. P. Miller. A direct method for the determination of the mean orientation-dependent elastic strains and stresses in polycrystalline materials from strain pole figures. *Journal of Applied Crystallography*, 39:358–368, 2006.
- [63] D. B. Williams and C. B. Carter. *Transmission Electron Microscopy*. Springer, 1996.
- [64] A. H. Cottrell and D. Hull. Extrusion and intrusion by cyclic slip in copper. *Proceedings of the Royal Society of London. Series A, Mathematical and Physical Sciences*, 244(1229):211–213, 1957.
- [65] S. J. Basinski, Z. S. Basinski, and A. Howie. Early stages of fatigue in copper single crystals. *Philosophical Magazine*, 19:899–924, 1969.
- [66] D. L. Jones and H. Liebowitz. A microscopic study of crack initiation mechanisms in 7075 aluminum alloy sheets. *Engineering Fracture Mechanics*, 5(2):397–402, 1973.

- [67] F. Ackermann, L.P. Kubin, J. Lepinoux, and H. Mughrabi. The dependence of dislocation microstructure on plastic strain amplitude in cyclically strained copper single crystals. *Acta Metallurgica*, 32(5):715–725, 1984.
- [68] Z. S. Basinski and S. J. Basinski. Fundamental aspects of low amplitude cyclic deformation in face-centred cubic crystals. *Progress in Materials Science*, 36:89–148, 1992.
- [69] W. A. Wood. Formation of fatigue cracks. *Philosophical Magazine*, 3(31):692–699, 1958.
- [70] U. Essmann, U. Gösele, and H. Mughrabi. A model of extrusions and intrusions in fatigued metals i. point-defect production and the growth of extrusions. *Philosophical Magazine A*, 44(2):405–426, 1981.
- [71] A. Hunsche and P. Neumann. Quantitative measurement of persistent slip band profiles and crack initiation. *Acta Metallurgica*, 34(2):207–217, 1986.
- [72] L. Corsetti and D. Duquette. The effect of mean stress and environment on corrosion fatigue behavior of 7075-T6 aluminum. *Metallurgical and Materials Transactions B*, 5:1087–1093, 1974.
- [73] S. E. Stanzl-Tschegg, O. Plasser, E. K. Tschegg, and A. K. Vasudevan. Influence of microstructure and load ratio on fatigue threshold behavior in 7075 aluminum alloy. *International Journal of Fatigue*, 21(Supplement 1):255–262, 1999.
- [74] P. S. Pao, C. R. Feng, and S. J. Gill. Corrosion fatigue crack initiation in aluminum alloys 7075 and 7050. *Corrosion*, 56:1022–1031, 2000.
- [75] K. Jones and D. W. Hoepfner. The interaction between pitting corrosion, grain boundaries, and constituent particles during corrosion fatigue

of 7075-T6 aluminum alloy. *International Journal of Fatigue*, 31(4):686–692, 2009.

- [76] N. E. Dowling. *Mechanical Behavior of Materials*. Prentice Hall, 2006.
- [77] R. V. Martins, L. Margulies, S. Schmidt, H. F. Poulsen, and T. Leffers. Simultaneous measurement of the strain tensor of 10 individual grains embedded in an Al tensile sample. *Materials Science and Engineering A*, 387-389:84–88, 2004.
- [78] J. C. Schuren, M. P. Miller, and A. Kazimirov. Creating a mechanical testing capability for measuring the microscale deformation behavior of structural materials. *Submitted to Experimental Mechanics*, 2010.
- [79] J. C. Schuren, S. L. Wong, M. P. Miller, and P. R. Dawson. Integrating high energy x-rays and finite element for a detailed characterization of deforming AA7075-T6 sample. *In preparation*, 2010.
- [80] W. Voigt. *Lehrbuch der Kristallphysik*. Teubner, 1928.
- [81] A. Reuss. Berechnung der fließgrenze von mischkristallen auf grund der plastizitätsbedingung für einkristalle. *Z. Angew. Math. Mech.*, 9(1):49–58, 1929.
- [82] G. I. Taylor. Plastic strain in metals. *Journal of the Institute of Metals*, 62:307–24, 1938.
- [83] T. H. Lin. Analysis of elastic and plastic strains of a face-centred cubic crystal. *Journal of the Mechanics and Physics of Solids*, 5(2):143 – 149, 1957.
- [84] C. A. Bronkhorst, S. R. Kalidindi, and L. Anand. Polycrystalline plasticity and the evolution of crystallographic texture in fcc metals. *Philosophi-*

*cal Transactions: Physical Sciences and Engineering Philosophical Transactions: Physical Sciences and Engineering*, 341(1662):443–477, 1992.

- [85] B. D. Cullity and S. R. Stock. *Elements of X-Ray Diffraction*. Prentice Hall, 2001.
- [86] L. Lutterotti, S. Matthies, and H.-R. Wenk. MAUD (Material Analysis Using Diffraction): a user friendly Java program for Rietveld Texture Analysis and more. In *Proceeding of the Twelfth International Conference on Textures of Materials (ICOTOM-12)*, volume 1, page 1599, 1999.
- [87] I. Lonardelli, H.-R. Wenk, L. Lutterotti, and M. Goodwin. Texture analysis from synchrotron diffraction images with the Rietveld method: dinosaur tendon and salmon scale. *Journal of Synchrotron Radiation*, 12(3):354–360, 2005.
- [88] J. V. Bernier, M. P. Miller, and D. E. Boyce. A novel optimization-based pole-figure inversion method: comparison with WIMV and maximum entropy methods. *Journal of Applied Crystallography*, 39(5):697–713, 2006.